Effect of Fiber Waviness on Compressive Properties of Quasi-Unidirectional Woven Fabric Composite Laminates

王, 波

https://doi.org/10.15017/1654887

出版情報：九州大学, 2015, 博士（工学）, 課程博士
バージョン：
権利関係：全文ファイル公表済

Effect of Fiber Waviness on Compressive Properties of Quasi-Unidirectional Woven Fabric Composite Laminates

By

Bo WANG

A Dissertation Submitted to
Department of Aeronautics and Astronautics
Graduate School of Engineering
Kyushu University
Fukuoka, Japan

December 2015

Abstract

Composites are widely used in aerospace, automobile, and many other green energy projects. Therefore, it is necessary to understand the compressive failure modes of composites in a broad range of applications.

Quasi-unidirectional (UD) woven fabrics are one type of woven carbon fabrics with unbalanced textile, which are woven with around 98% warp tows and a few weft yarns. The warp tows provide a loading capability after consolidation and the weft yarns make the fabric integrity for a good drapability. However, fiber misalignment in the quasi-UD woven fabrics is a kind of defects, which causes significant reductions in compressive mechanical properties of the CFRPs.

This study presents an investigation of the compressive failure mechanisms of the quasi-UD woven fabric composites due to fiber waviness. Three kinds of the quasi-UD woven fabrics, Standard pitch fabrics (SP), Long pitch fabrics (LP) and Thin pitch fabrics (TP), were selected for this research. Based on a measurement for in-plane fiber waviness and an evaluation for out-of-plane fiber waviness, the three fabrics are divided into two groups, the SP and LP are used for the study of effect of out-of-plane fiber waviness and the SP and TP are done for the study of effect of in-plane fiber waviness, respectively. Afterward, compressive tests were performed and the experimental results

showed the negative effect of out-of-plane and in-plane fiber waviness on the compressive properties. Finally, finite element method (FEM) was implemented to account for failure mechanisms of the quasi-UD woven fabric composite as well. The results show the fiber waviness has a greater effect on compressive strength than that on the compressive modulus, and this research will benefit designing in architecture of the quasi-UD woven fabrics.

Keywords:

Quasi-UD woven fabric; out-of-plane fiber waviness; in-plane fiber waviness; compressive properties; finite element method (FEM).

Contents

Chapter 1

Introduction

1.1 Overview

Carbon fiber reinforced polymer (CFRP) consists of carbon fibers of high strength and modulus embedded in a matrix with distinct interfaces between them [1]. In this form, the CFRPs produce a combination of properties that cannot be achieved with the fibers or matrix acting alone. In general, the fibers are the major load-carrying members, and the surrounding matrix acts as a load transfer medium between them and keeps them in a desired location and orientation, moreover, the matrix protects them from environmental damages such as humidity and corrosion.

CFRPs are commonly used wherever high strength-to-weight ratio and rigidity are required, such as aerospace, automotive and civil engineering, and an increasing number of other consumer and technical applications, for example, the Boeing 787 Dreamliner is about 50% the CFRPs by weight (Fig. 1-1) [2]. However, they are expensive and lack of high productivity manufacturing methods and clear-cut design rules, which are disadvantages at their usages.

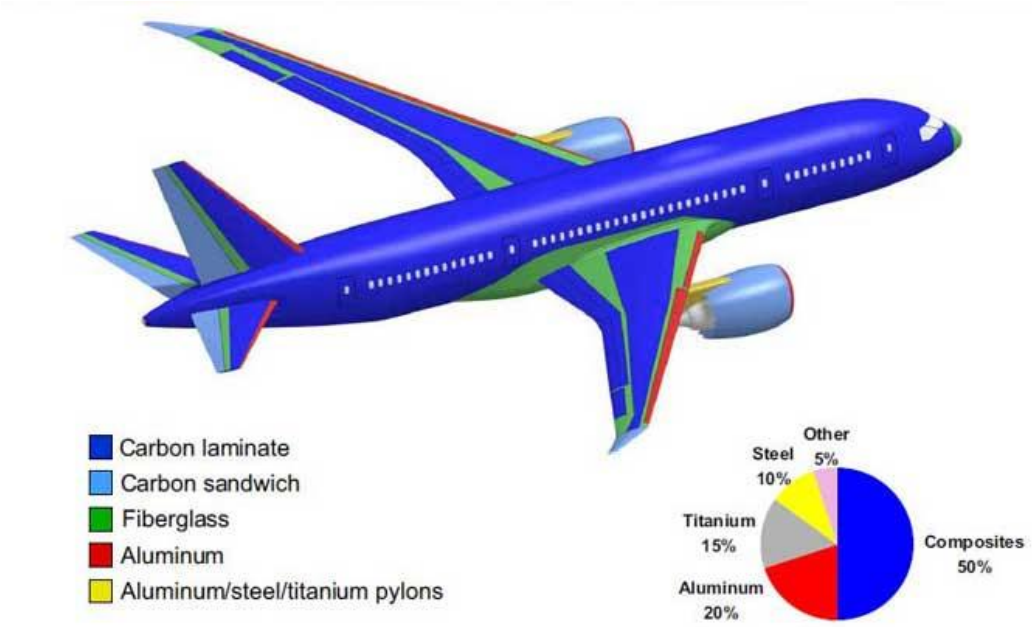

Fig. 1-1 Composite materials in Boeing 787

Quasi-unidirectional (UD) woven fabrics are a special type of woven carbon fabrics that have unbalanced textiles, which are woven with ~98% warp tows and a few weft yarns [3], which is a kind of the dry fiber preform to fabricate the CFRPs. In this fabric, the warp tows of the carbon fibers provide loading capability, after consolidation, and the weft yarns of glass fibers bestow fabric integrity that, in turn, leads to good drapability. However, the UD woven fabrics are prone to fiber misalignment, which has an adverse effect on mechanical properties of the CFRPs, such as tensile properties [4-10], fracture properties [11,12], fatigue properties [13,14] and transverse properties [15,16], especially on the compressive properties.

1.2 Fiber misalignment

In 1965, Rosen [17,18] estimated compressive strength of the CFRPs by theory of elastic stability. Idealized fibers, as elastic beams, are embedded in a matrix and buckle in two instability modes: extension mode and shear mode (Fig. 1-2). The corresponding buckling stresses are for the compressive strengths and given in Eqs. (1-1) and (1-2). It is found that the extension mode is the lower stress for the low fiber volume fractions, while for high volume fractions of fibers the shear mode predominates. In general, the lower stress is associated with the shear mode when fiber volume fraction of the CFRPs is higher than 40%, but this stress is four times as great as experimental results.

$$\sigma_c = \frac{G_m}{1-V_f} \tag{1-1}$$

$$\sigma_c = 2V_f \left[\frac{V_f E_m E_f}{3(1-V_f)}\right]^{1/2} \tag{1-2}$$

where

σ_c= compressive strength

V_f= fiber volume fraction

G_m= matrix shear modulus

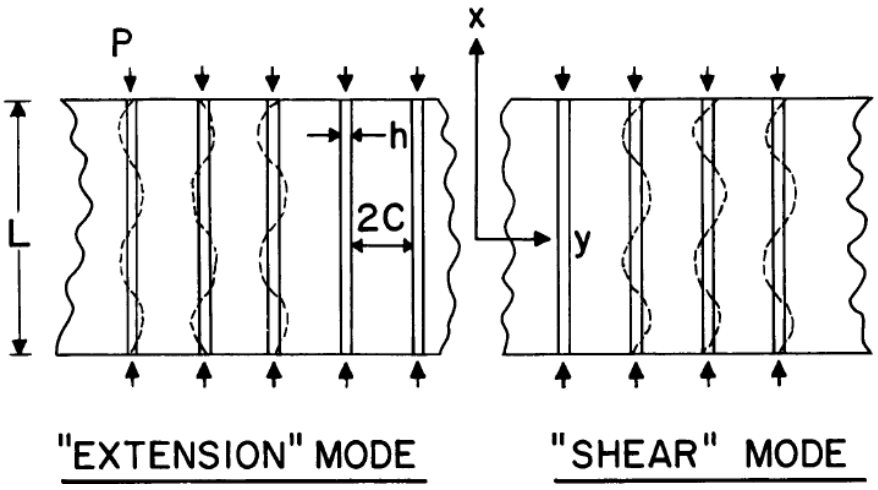

Fig. 1-2 Two instability modes of carbon fibers: extension mode and shear mode

To solve overestimations of the compressive strengths based on Rosen's theory of elastic stability, Argon [19] pointed out that fiber misalignment as a kind of manufacturing defects leads to development of local shear stress in the shear mode, which creates kinking bands when the shear stresses reach the shear yield strength of the matrix. Therefore, the compressive strengths are reduced as Eq. (1-3). Then Budiansky [20] extended Argon's work, and applied an elastic-perfectly plastic shear response on the CFRPs to deduce the compressive strengths as Eq.(1-4), which induces that plastic kinking tend to arrange the fibers into inclined bands. After that, he and Fleck [21-25] adopted a three-parameter Ramberg-Osgood relationship for the shear response in their further analysis, and theoretically and experimentally evidenced the CFRPs have a tendency to fail in compression by plastic kinking.

$$\sigma_c = \frac{\sigma_{12}}{\theta_0} \tag{1-3}$$

$$\sigma_c = \frac{\sigma_{12}}{(\theta_0+\gamma)} \tag{1-4}$$

where

σ_{12}= shear yield strength of the matrix

θ_0= initial local fiber misalignment angle

γ= shear yield strain of the matrix.

Evans and Adler [26] observed the kinking bands in CFRPs and proposed a process of kinking deflection under the shear stress developing from the fiber misalignment, which is shown as Fig. 1-3: (a) a micromodel of the CFRPs with fiber misalignment, (b) local shear stress developed due to the fiber misalignment, (c) carbon fibers fractured with increasing the local shear stress, (d) generation of the kinking bands. It demonstrated the plastic performance is important in the deflection.

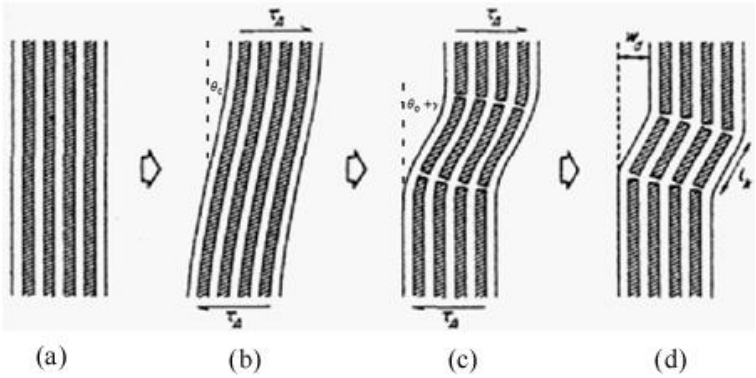

Fig. 1-3 A schematic indicating the formation of a kink band

Wisnom [27] analyzed a misalignment angle between the fibers and loading axis of the CFRPs, and presented some stages which is likely to introduce the fiber misalignment, such as, the specimen not being exactly parallel to the loading axis, eccentricities as a result of imperfections in the way the specimen is tabbed and gripped, specimens aren't cut exactly in line with the fiber direction, occurrence during lay-up of the material, and within reinforcement material itself.

Jelf and Fleck [28] continued their working on the compressive failure of unidirectional fiber composites and identified four mechanisms of failure (Fig. 1-4): fiber failure, elastic microbuckling, matrix failure, and plastic microbuckling. They find that plastic microbuckling dominate the compressive failure mechanism in polymeric matrix composites, which is influenced by the shear yield strength of the matrix and the misalignment of the fibers as well as plastic kinking.

Shuart [29] used multidirectional composite laminates to analyze compressive failure modes with different fiber misalignment angles, θ, and showed that: Interlinear shearing is shown to be the dominant failure mode for $0 < \theta < 15$ deg. In-plane matrix shearing is shown to be the dominant failure mode for $15 < \theta < 50$ deg. Matrix compression is shown to be the dominant failure mode for $50 < \theta < 90$ deg.

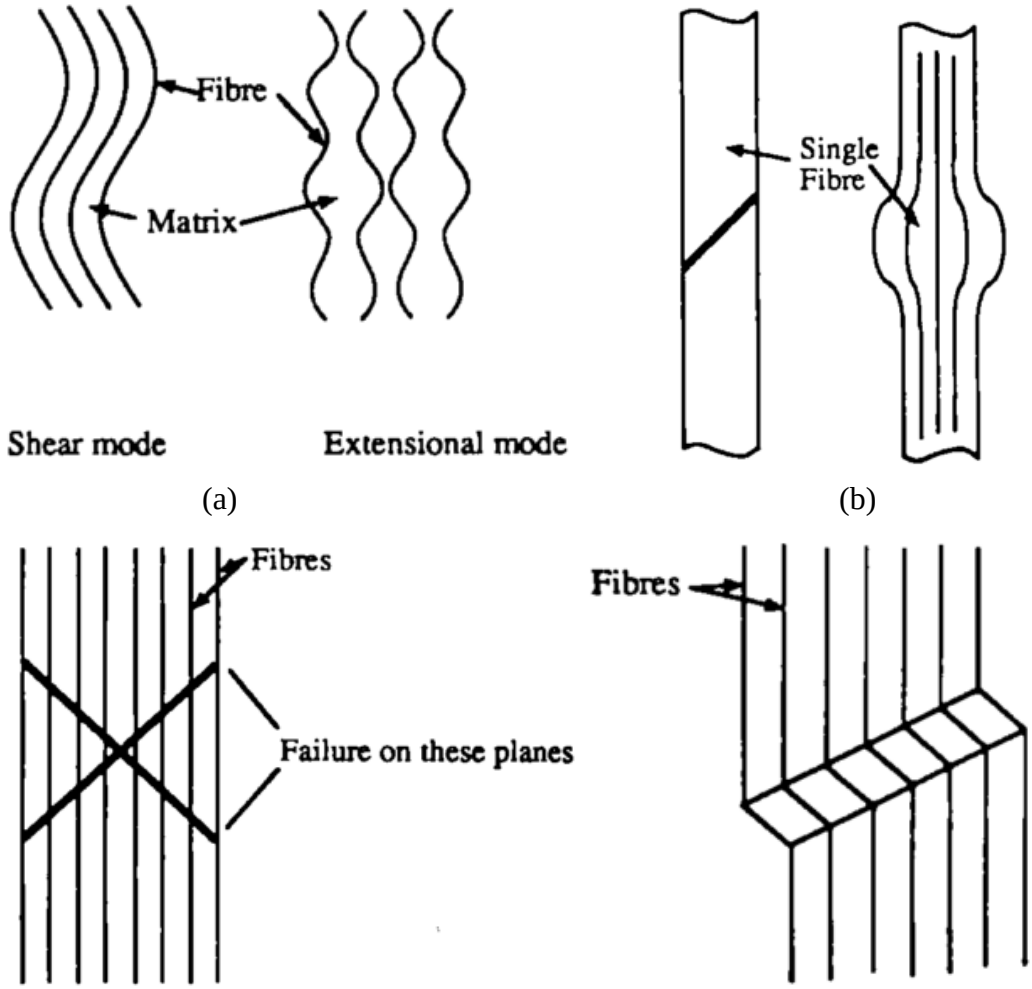

Fig. 1-4 Four mechanisms of failure: (a) elastic microbuckling. Two modes are distinguished, shear and extensional; (b) fiber crushing, for example, by shear yielding of the fiber or splitting of the fiber; (c) matrix failure; (d) plastic microbuckling.

Meanwhile, some numerical models were proposed for this issue. Fleck and Shu [30] developed a finite element code based on general Cosserat couple stress theory for the plastic kinking, and found that the compressive strength is limited between the Rosen' result to the infinite band strength of Fleck et al. [23].

Sun and Jun [31] applied von Mises J_2 plasticity to matrix in their numerical model, and found that both matrix plasticity and fiber misalignments have significant effects on lowering the composite compressive strength. However, the fiber misalignments or matrix plasticity alone cannot alter the elastic microbuckling strength.

Wisnom [32,33] proposed a finite element model for compressive failure due to shear instability in ABAQUS, and rebar capability with nonlinear geometry and orthotropic material properties with nonlinear shear response were adopted. His study demonstrated the limitation of theories of compressive strength which assume a uniform, unconstrained stress state, which can make an overestimation in reduction of compressive strength.

1.3 Fiber waviness

The effect of fiber misalignments is presented above. Fiber waviness, curved fibers associated with the fiber misalignments, is another important manifestation in the CFRPs, which contains wave amplitude and wavelength. Many researchers contribute their work on the effect of the fiber waviness.

Kyriakides and his co-workers [34] conducted confined rod experiments and found that the kinking bands propagate with loading dropping in a dynamic way as shown in Fig. 1-5. Then they used a sinusoidal curved imperfection to represent the fiber waviness, and simulated some parametrical effect of the fiber imperfection using Riks' method in ABAQUS. It found that band orientations and widths are relatively insensitive to the microsection size and to the imperfection amplitude and wavelength.

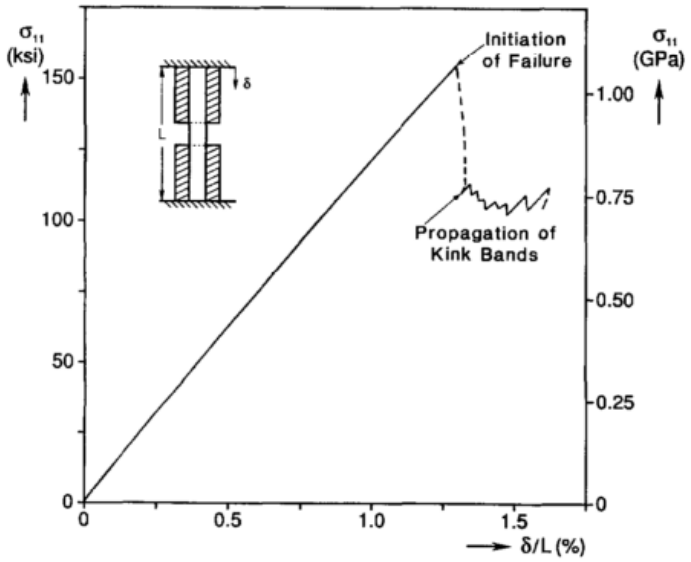

Fig. 1-5 Axial stress-end shortening response recorded in a confined rod experiment

Hsiao and Daniel et al. [35-40] fabricated unidirectional wavy composites with out-of-plane by a tape-winding method and a three-step curing method. After compression experiments on the unidirectional wavy composites, they found the first failure mechanism is shear yielding or shear failure in the matrix precipitated by initial fiber misalignment, then the matrix shear yielding is followed by fiber buckling and fracture to create the kinking bands (Fig. 1-6). In addition, it was reported that in unidirectional composites both major Young's modulus and compressive strength degrade seriously as the fiber waviness increases and interlaminar shear stress is far more significant than other stress components in initial failure mechanism, which is followed by delaminations and layer buckling.

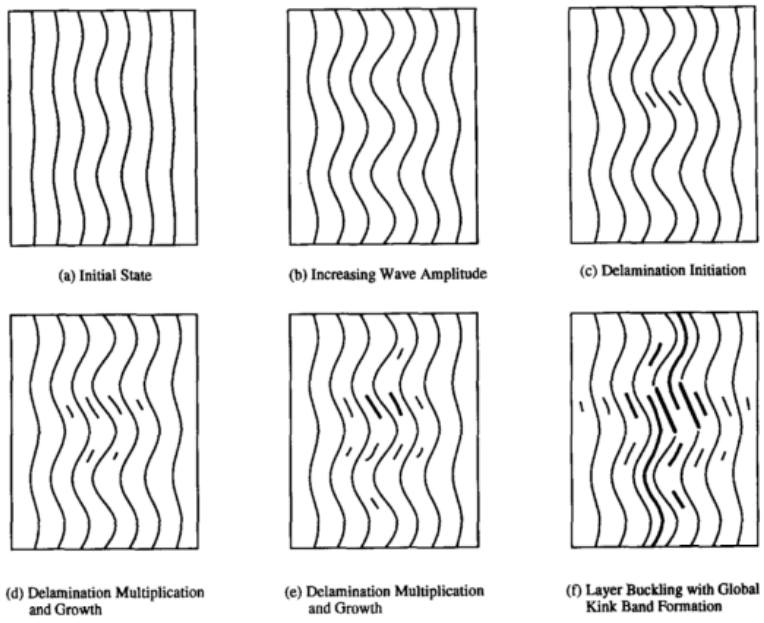

Fig. 1-6. Failure progression in IM6G/3501-6 unidirectional composite with graded waviness under axial compression

Adams and Hyer [41,42] developed a single-step fabrication procedure based on their three-step method of fabrication for producing fiber waviness into the CFRPs with varying wavy 0° layer fractions. They found fiber waviness reduce compressive strengths under a certain percentage of 0° layers containing layer waviness, and a constant strength reduction of was observed when more than 33% of the 0° layers contained waviness.

Garnich and Karami [43-46] proposed geometrically wavy micromechanics model for the fiber waviness in the CFRPs, and their studies demonstrated the importance of local stresses. However, this model over predicted the effects of fiber waviness because of enforcement of periodic constraints. Then they made a wavy material-orientation model and used neighboring isotropic or straight fiber material layers to instead of the periodic constraints, and it showed that the shear and transverse normal stress response associated with fiber straightening is reduced due to the presence of adjacent materials.

1.4 In-plane-fiber waviness in Z-pins

Z-pins are useful through-thickness reinforcements to the CFRPs to against delaminations [47-49]. However, the embedded z-pins cause in-plane fiber waviness of the CFRPs because of the relative large diameter of the z-pins as shown in Fig. 1-7 [50]. Mouriz's studies experimentally demonstrated the compressive modulus and strengths are reduced by the in-plane fiber waviness [51,52]. O'Brien and Krusger [53] used a 2D finite element code (FLASH) based on Fleck and Shu's Cosserat couple stress theory, and determined increasing pin diameters make in-plane fiber waviness increase and decrease the compressive strengths. Steeves and Fleck [54] also used the FLASH and get a good agreement at the kinking bands surrounding resin-rich zones between simulations and experiments. Xie et al. [55] proposed a quarter of cell model with non-uniform spacing fiber and isotropic matrix. They found the influence of non-linear shear properties of matrix on compressive strength is obvious for small diameter of pin and the fast reduction of compressive strength with increasing pin diameter before the pin diameter is up to critical value.

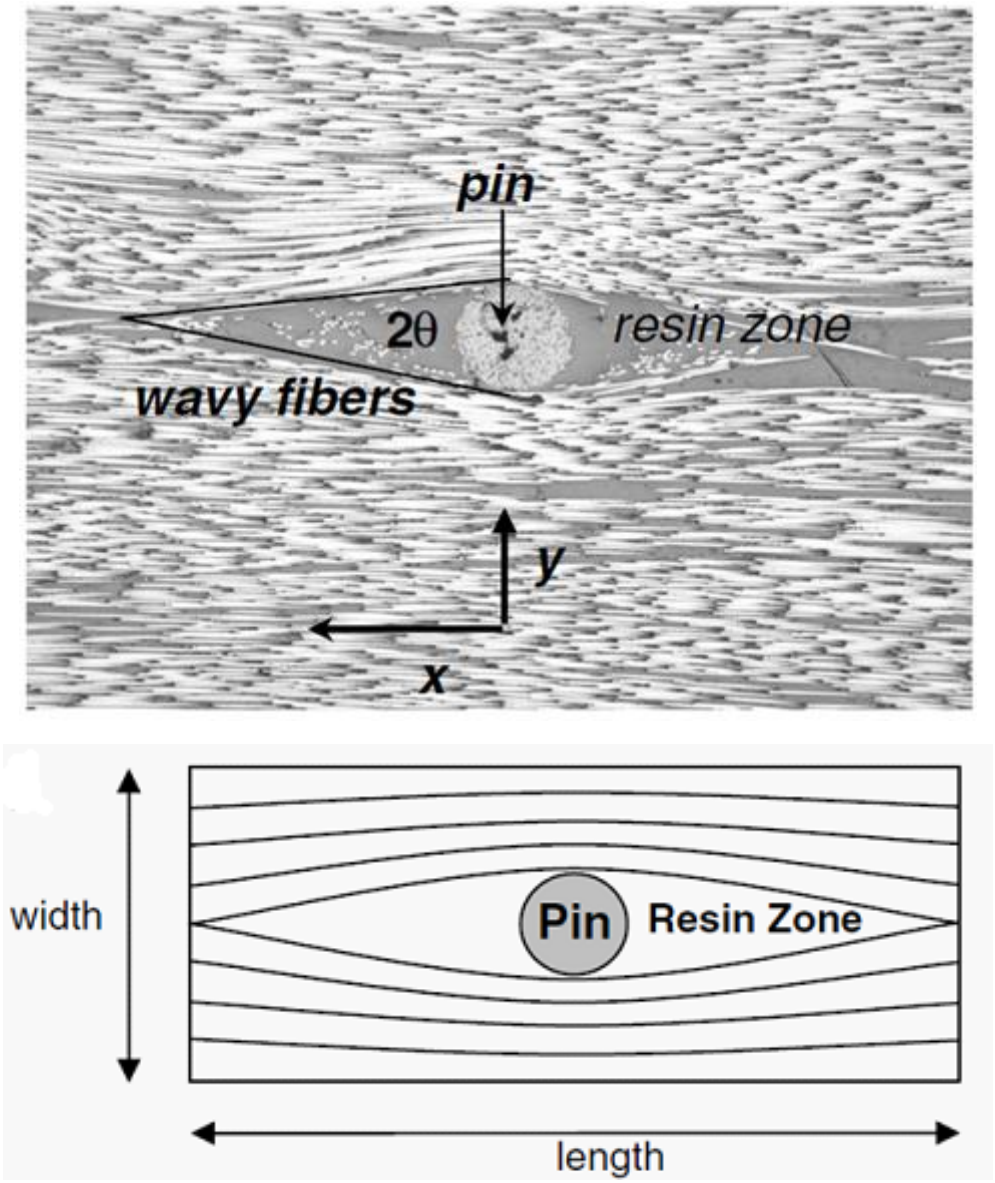

Fig. 1-7 In-plane fiber waviness and resin-rich zones surrounding a pin

1.5 Measurements of fiber misalignment

Yurgartis [56] presented a useful technique for measuring the volume fraction distribution of fiber misalignment angle and assumed (1) that short sections of fibers are approximately straight and (2) that all fibers have the same circular diameter. In this measurement technique, he sectioned the composites at a certain plane-cut angle, and then measured ellipse major axis lengths of cut fibers, and finally calculated the fiber misalignment angle based on a relationship among fiber diameters, the major axis lengths and the plane-cut angle. However, polishing artifacts, manual collection of data and fiber curvature raised errors and needed to be improved in future study.

Zak and his co-workers [57] proposed a two-section method to obtain a three-dimensional fiber-orientation distribution, which consists of three major steps: (i) obtain two cross-sections of the specimen and fit ellipses to the fiber cross-sections observed within the two sections; (ii) identify the ellipses belonging to the same fibers and estimate the section-to-section transformation; and (iii) calculate angles of the transformations for each matched fiber to obtain the overall fiber-orientation distribution. But intensive labor and local desired cross-section region were two limitations of this method.

Clarke et al. [59] used confocal laser scanning microscope (CLSM) to determine 3D fiber waviness from a single polished section even reconstruct the spatial distribution of short fibers, and this confocal technique was limited by maximum useful depths.

Sutcliffe and his co-workers [60,61] presented a multiple field image analysis (MFIA) procedure based on typical intensity distributions along lengths of arrays. The file of interest is first divided up into a number of domains, and some points within the domains are rotated to an angle to calculate the light intensity. By rotating through a series of angles and calculating repeatedly, the angle with minimum light intensity corresponds to the fiber misalignment angle. However, a disadvantage of MFIA-method was computation time consuming in this version. Then they improved and adopted the MFIA-method for measurement of in-plane and out-of-plane waviness misalignment angles even from X-ray images.

Kratmann et al. [62] extended the MFIA-method to Fourier transform misalignment analysis (FTMA) method. They used a 2D fast Fourier transformation (FFT) to transform the spatial domains into frequency domains and obtained a centered logarithmic power spectrum in each domain. Finally, the mean fiber orientation was determined by the orientation of white line in each domain. It is a robust method and much faster than the MFIA-method.

1.6 Scope of work

Based on the literatures reviewed above, we can find that fiber misalignment is an important factor on the CFRPs. The pioneers proposed theories of compressive strength which assume uniform fiber misalignment angle to analyze the reduction in compressive strength. However, the uniform fiber misalignment angle is not likely to occur in the actual CFRPs, which causes an overestimation in the reduction. Moreover, the artificial out-of-plane fiber waviness is much larger than the actual out-of-plane fiber waviness in the CFRPs, which exaggerates the effect of out-of-plane fiber waviness on the compressive properties.

Quasi-UD woven fabrics are a kind of reinforcements in the CFRPs, and the out-of-plane and in-plane fiber waviness in these fabrics are much smaller than the artificial out-of-plane fiber waviness or the in-plane fiber waviness surrounding the Z-pins. Moreover, the textile configurations of quasi-UD woven fabrics produce different fiber waviness, which causes the quasi-UD woven fabric composites failed in different compressive failure modes. Unfortunately, many researchers ignored the effect of fiber waviness in the fabric composites. Therefore, the effect of fiber waviness on compressive properties of quasi-UD woven fabric composites and the size effect of fiber waviness are studied in this research. Three types of quasi-UD woven fabrics were selected to fabricate

the quasi-UD woven fabric composites via VaRTM process. The compression tests were performed to evaluate the effects of out-of-plane and in-plane fiber waviness respectively. Finally, finite element method was used to analyze the failure mechanisms in out-of-plane and in-plane fiber waviness respectively.

Chapter 2

Materials

2.1 Quasi-UD woven fabrics

Quasi-UD woven fabrics have been developed as a substitute for UD tapes in resin infusion processes, which is shown in Fig. 2-1. In general, around 98% warp, typically 6k, 12k or 24k carbon tow and remaining weft yarn that may be 3k carbon, fine glass yarns or thermoplastic binder yarns are woven to these quasi-UD woven fabrics. The warp tow lie straight, and it dominates a contribution to strength or stiffness of woven fabrics composites. The weft yarn is used to keep structural integrity for holding the fabric in position during processing, thus its contribution to strength or stiffness is normally ignored. Therefore, classical laminate analysis is normally used to analyze stresses in the quasi-UD woven fabrics composites from the design point of view.

In making a comparison between the quasi-UD woven fabrics and UD tapes the following comments can be made:

A. Warp tows are as straight as UD tapes;

B. Improved drapability over UD tapes;

C. Minimal reduction of fiber strength;

D. Improved fiber alignment.

Quasi-UD woven fabrics have several disadvantages:

A. Adding weaving process into manufacturing stages;

B. Lower fiber volume fractions than UD tapes.

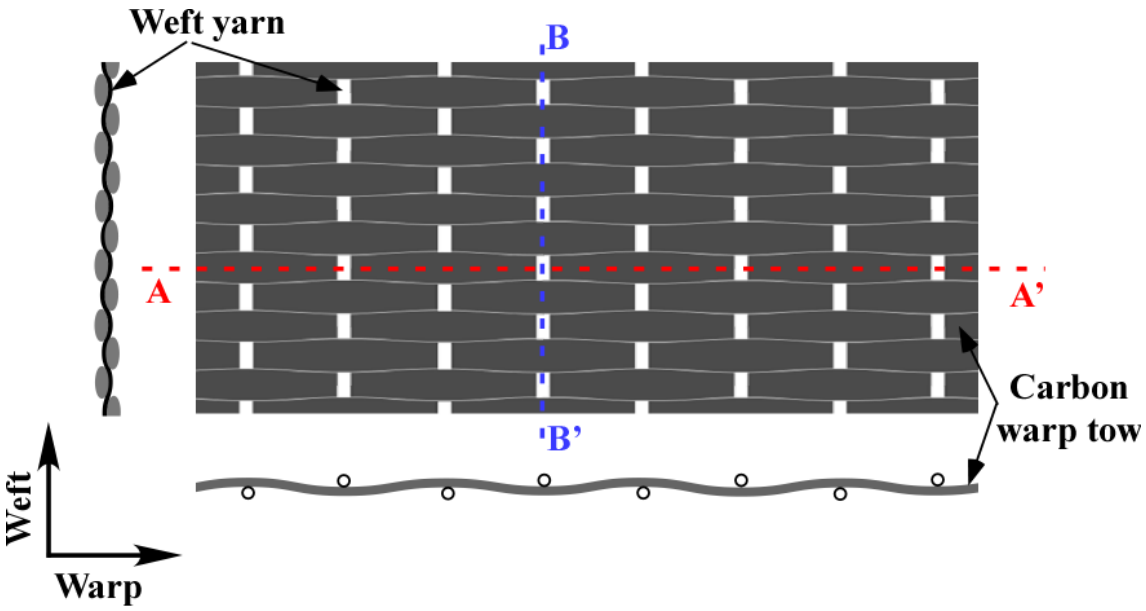

Fig. 2-1 A schematic of quasi-UD woven fabrics

There are three types of the quasi-UD woven fabrics in our laboratory, which are made of carbon fibers and glass fibers that lie along the warp and weft directions, respectively [63,64]. The trademark of the carbon fibers is MR50S-12K from Mitsubishi Rayon Co., Ltd., the density of the carbon fibers is 1.81 g/cm^3. The tensile modulus of the carbon fibers is 295 GPa with a tensile strength of 5500 MPa [65]. In the weft direction, the weft yarns are formed by twisting the glass fibers, whose trademark is ECD450 1/2

4.4S (Nitto Boseki Co., Ltd.) with an outside diameter of 0.08 mm and the length per kilogram is 44.6 km/kg. The diameter of single glass fiber is 5 μm [66]. The carbon fibers are woven at different pitch intervals or densities by these yarns. The resulting quasi-UD woven fabrics are referred to as standard pitch fabric (SP), long pitch fabric (LP) and thin pitch fabric (TP), respectively, as shown in Fig. 2-2.

Table 2-1 shows the textile configurations of the three quasi-UD woven fabrics. As the table shows, the SP and TP fabrics have the same pitch intervals but different pitch density. In contrast, the SP and LP fabrics have the different pitch intervals but same pitch density. Therefore, inspections on quasi-UD woven fabrics were conducted.

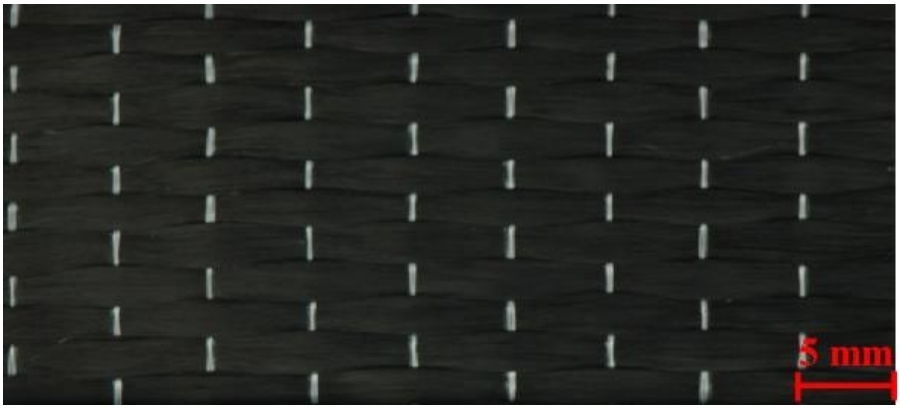

(a)

(b)

(c)

Fig. 2-2 three types of the quasi-UD woven fabrics: (a) standard pitch fabric, (b) long pitch fabric and (c) thin pitch fabric

Table 2-1 Textile configurations of the three quasi-UD woven fabrics

Fabrics	Standard pitch fabric SP	Long pitch fabric LP	Thin pitch fabric TP
Warp tow	MR50S-12K Carbon Fibers		
Weft yarn	ECD450 1/2 4.4S Glass Fibers (280dTex)		
Pitch interval L_{pi}	5 mm	8.3 mm	5 mm
Pitch density ρ_{pd}	5.4 picks/cm	5.4 picks/cm	3.3 picks/cm
Areal weights w_f	316 g/m^2	319 g/m^2	199 g/m^2

2.2 Inspection of in-plane fiber waviness

From the observation of geometry on the quasi-UD woven fabrics, we can find that the warp tows are far from being straight due to the weft yarns, which produces some periodic patterns and makes in-plane fiber waviness in the quasi-UD woven fabrics in fact (Fig. 2-3). Moreover, characteristics of the in-plane fiber waviness are depended by the pitch density in the weft direction.

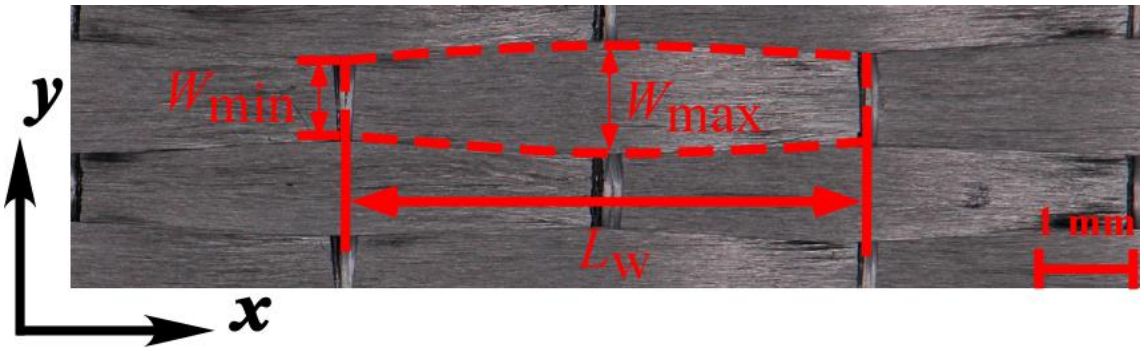

Fig. 2-3 In-plane fiber waviness in the quasi-UD woven carbon fabrics.

We use three parameters to describe the in-plane fiber waviness, namely, the wavelength (L_w), in-plane wave amplitude (A_{in}), and tow width (W); A_{in} and W are calculated as follows from the mean maximal and minimal width, W_{max} and W_{min}, respectively:

$$A_{in} = \frac{W_{max} - W_{min}}{4} \qquad (2\text{-}1)$$

$$W = \frac{W_{max} + W_{min}}{2} \tag{2-2}$$

If we assume the in-plane fiber waviness to a sinusoidal function, the maximum fiber misalignment angle of the in-plane fiber waviness, θ_{0in}, is calculated as Eq. (2-3).

$$\theta_{0in} = \frac{2\pi A_{in}}{L_w} \tag{2-3}$$

An in-plane fiber waviness ratio (R_{in}) are given in Eq. (2-4)

$$R_{in} = \frac{A_{in}}{L_w} = \frac{\theta_{0in}}{2\pi} \tag{2-4}$$

The data of in-plane fiber waviness on the three quasi-UD woven fabrics is shown in Table 2-2. The SP fabric and TP fabric have the same wavelength but the LP fabric has longer wavelength than the SP and TP fabric, and it is because the SP fabric and TP fabric have the same pitch intervals in the warp direction but the LP fabric's pitch intervals is longer than theirs, thereby we can get a relationship between the wavelength (L_w) and pitch interval (L_{pi}) as Eq. (2-5)

$$L_w \approx 2L_{pi} \tag{2-5}$$

Moreover, The SP fabric and LP fabric have the same tow width but they are less than the TP fabric's, which is caused by differing pitch densities in the weft direction. Thus the tow width is depended on the pitch densities. In addition, the in-plane wave amplitude of the LP fabric is greater than that of the SP fabric at the same pitch densities but the wave amplitude of the TP fabric is very small, which shows the in-plane wave amplitude

increases with increasing pitch density and wavelength. However, although the wave amplitude of the LP fabric is greater than that of the SP fabric, the in-plane fiber waviness ratio of the LP fabric is similar to the SP fabric due to the LP fabric's longer wavelength than SP fabric's.

Table 2-2 In-plane fiber waviness on the three quasi-UD woven fabrics
(Coefficient of variation shown in parentheses)

Fabrics	Standard pitch fabric SP	Long pitch fabric LP	Thin pitch fabric TP
Wavelength L_w	10.16 mm (1.4%)	16.94 mm (0.7%)	10.14 mm (1.6%)
Maximal width W_{max}	2.06 mm (8.8%)	2.18 mm (7.3%)	3.01 mm (7.1%)
Minimal width W_{min}	1.59 mm (11.8%)	1.48 mm (12.1%)	2.95 mm (7.0%)
Tow width W	1.83 mm	1.83 mm	2.98 mm
In-plane wave amplitude A_{in}	0.12 mm	0.18 mm	0.015 mm
In-plane waviness ratio R_{in}	0.0117	0.0104	0.0015

Chapter 3

Vacuum assisted resin transfer molding (VaRTM)

3.1 VaRTM process

Vacuum assisted resin transfer molding (VaRTM) process is a type of low cost manufactures of the CFRPs, which makes a low viscosity resin matrix injects into dry fiber preform placed in a tool and covered by a flexible vacuum bagging material via a vacuum system.

This process offers the benefits of relatively lower cost than autoclave and simple low cost tooling because it is able to cure very large and complex composite parts at room temperature with an optional post cure. The usage of the vacuum makes the composite parts have higher fiber volume fraction than hand lay-up, in addition, this close system reduced environmental concerns.

Fig. 3-1 shows a basic setup for the VaRTM process, the dry fiber preform is prepared on the tool to mold, covered by two peeling films which eliminate the need for sanding or grinding the excess resin after curing. Then an inlet is set in the left, which connects to a resin tank. In the right, an outlet connecting to a vacuum pump is set to make the resin flows from the resin tank to the dry preform under a pressure differential. Distribution medium is placed on the upper peeling film to let the resin flow through the

dry fiber preform successful. All materials are covered by a bagging film and sealant tape. The bagging film is able to make a uniform pressure apply to the part surface, and the sealant tape produces an airtight bond between the bag and the tool and to repair leaks. After leaking inspection and infusion, the dry fiber preform and the resin are heated by the tool for curing. The time of the curing and post curing process are depended on the types of the resin, and the composite part is completed after the post curing. Equipment and process materials are shown in the Tables 3-1 and 3-2. More details of the VaRTM process are listed in section 3.2.

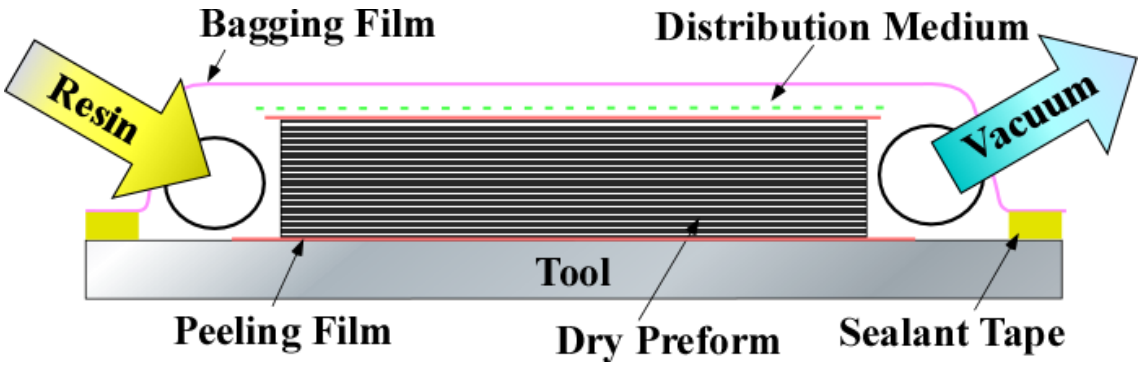

Fig. 3-1 A basic setup of the VaRTM process

Table 3-1 Equipment for the VaRTM process

Tool	500mm×400mm×4mm， Aluminum	-
Heating plate	Aluminum	Tekko Room
Heater	1M-2-1500， 1500W	Sakaguchi Electric Heater
Temperature controller	E5AR-TQ43B-FLK	OMRON
Pressure sensor	E8F2-AN0B	OMRON
Two-way solenoid valve	BN-7M21-8A	Nippon Seiki
Vacuum pump	Direct-coupled oil rotary vacuum pump G-20D， G50D	ULVAG
Data logger	Remote scanner Jr.DC3100	NEC Sanei
Stirrer	Three-One Motor BL-1200	HEIDON
Resin tank & trap	Main body：Aluminum Cover：Acrylic	Tekko Room
Temperature controller for resin	E5CK	OMRON
Resin heater A	Cimarec 2	Thermolyne
Resin heater B	Hot Plate PC-160	CORNING
Clamp for injection tube	Steel	Tekko Room
Inlet and outlet port	Aluminum	Tekko Room
Dressmaking scissors	# 7280 beaver scissors	Kai
Clothes iron	NI-A55	Panasonic
Tube cutter	TC-16	Chiyoda Tsusho

Table 3-2 VaRTM process materials

Punching metal	PA-24	Takachi Electric Industry
Peeling film	Release Ease 234 TFP1 brown	Airtech
Sealant tape	AT-200Y	Airtech
Bagging film	KM1300	Airtech
Disposable beaker	500 ml, 1000 ml	-
Bleeder valve	unknown	-
Release agent	Safelease #30	Airtech
Distribution medium	Green Flow 75	Airtech
Hose A	Superflex F-1510	Aoi
Hose B	Connecting tube TEN-8-10TM	Trusco
Tube connector	I, Y & T type with different diameter	-

3.2 Procedure

A procedure of VaRTM process to fabricate CFRPs is described in this section, and a brief schedule is shown in Fig. 3-2. This procedure consists of cutting fabrics out, fabric lay-up, hot compaction, epoxy resin mixing, infusion, cure and post cure. The vacuum pressure and temperature in each step are shown in Fig. 3-3.

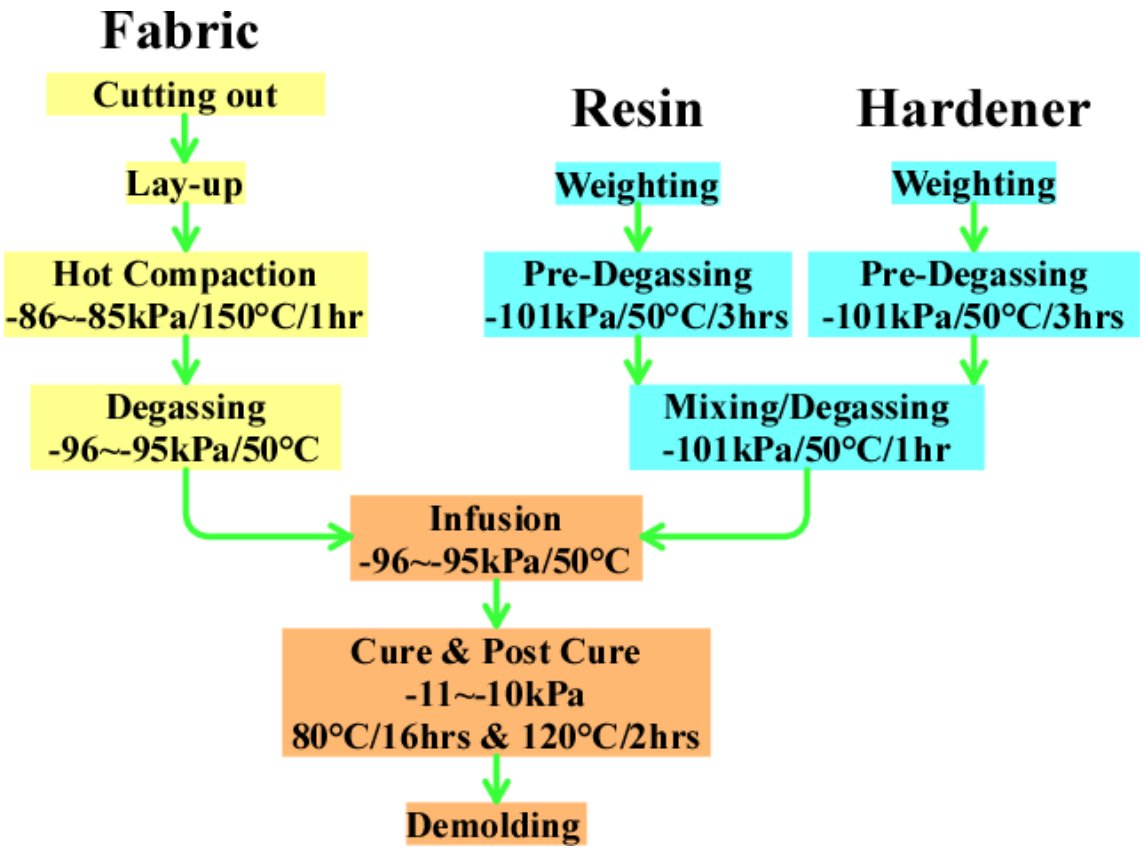

Fig. 3-2 A brief schedule of VaRTM process

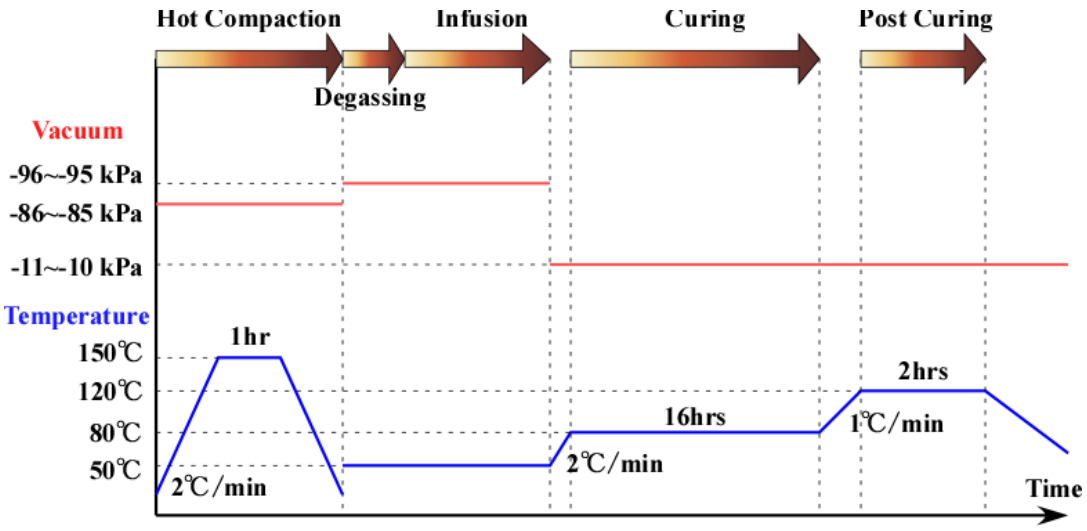

Fig. 3-3 A history of the vacuum pressure and temperature in VaRTM process

1. Cutting fabrics out

The fabrics are cut out at desired size by the dressmaking scissors. It should be noticed that cutting paths of 0° or 90° ply should follow the middle line of two weft yarns or the warp tows, which keeps a good integrity of the quasi-UD woven fabrics. However, the cutting paths of ±45° ply should be pasted with a masking tape first, and then cut the ±45° ply follow the middle line of the masking tape, which make a good incision on the ±45° ply.

2. Fabric lay-up

Two pieces of the peeling film, a big one and a small one, are prepared for this step, and the big peeling film is laid on the tool. Use alcohol to clean the tool and the peeling film before touching the fabrics. One ply of the fabrics is placed at desired degree on the

big peeling film, and then is covered by the small peeling film. The clothes iron is used to heat and press the fabrics at about 150 °C on the small peeling film. After heating and pressing, remove the clothes iron and the small peeling film. Add another ply on the ply as a stacking sequence and repeat the heating and pressing process one ply by one ply. This step is to prevent a slip among plies during hot compaction.

3. Hot compaction

Hot compaction is conducted to solidify the fabrics, which is able to prevent a displacement of ply when resin injection. The punching metal is cut off and polished by #80-2000 sandpapers, which keeps the fabric flat without any wrinkle under atmosphere pressure. The tool and the punching metal should be coated twice by the release agent. Then place the fabrics and the process materials as Fig. 3-4 and a vacuum pressure is controlled at -86~-85 kPa (ON~OFF) by the two-way solenoid valve and the pressure sensor. After leaking inspection, the tool and the fabrics are heated by the heating plate at 150 °C in one hour.

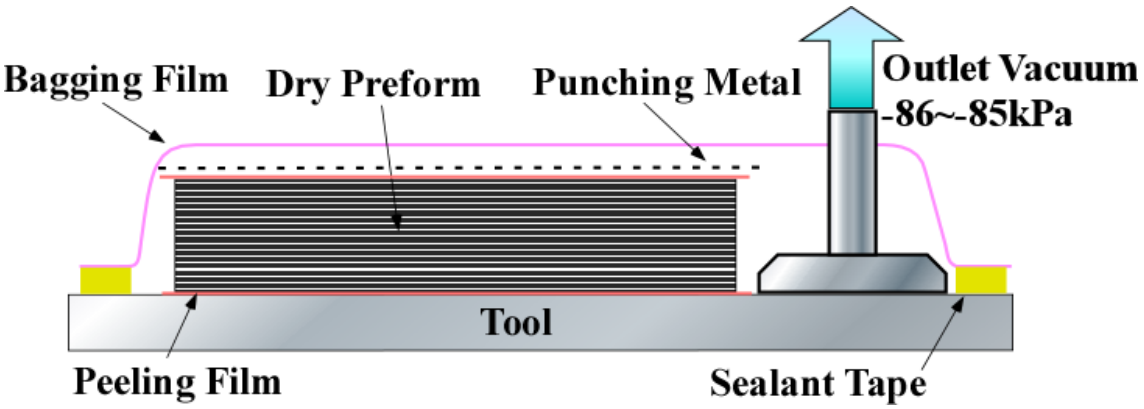

Fig. 3-4 A setup of hot compaction

4. Epoxy resin

The epoxy resin is a matrix to consolidate with the fabrics, and the trademark is XNR/H6809 from Nagase ChemteX [67]. The hardener and resin are separately degassed at 50 °C under -101 kPa vacuum pressure for 3 hours. Then they are mixed at a ratio of 0.95 (hardener: resin= 95:100) with the stirrer at a rotate speed of 100 rpm, and are degassed together at a suitable temperature for one hour. The suitable temperature is depended on the relationships of viscosity with temperature and time, which are shown in Figs. 3-5 and 3-6. Moreover, physical properties of the epoxy resin are listed in Table 3-3.

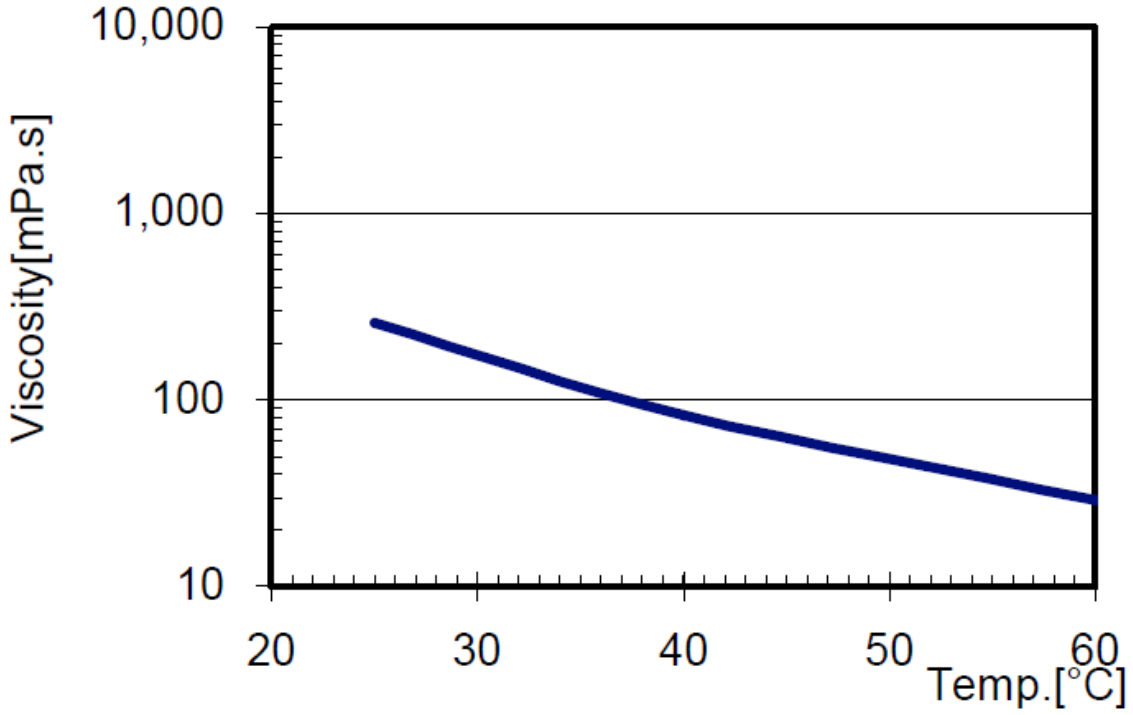

Fig. 3-5 XNR/H6809 Viscosity / temperature Profile

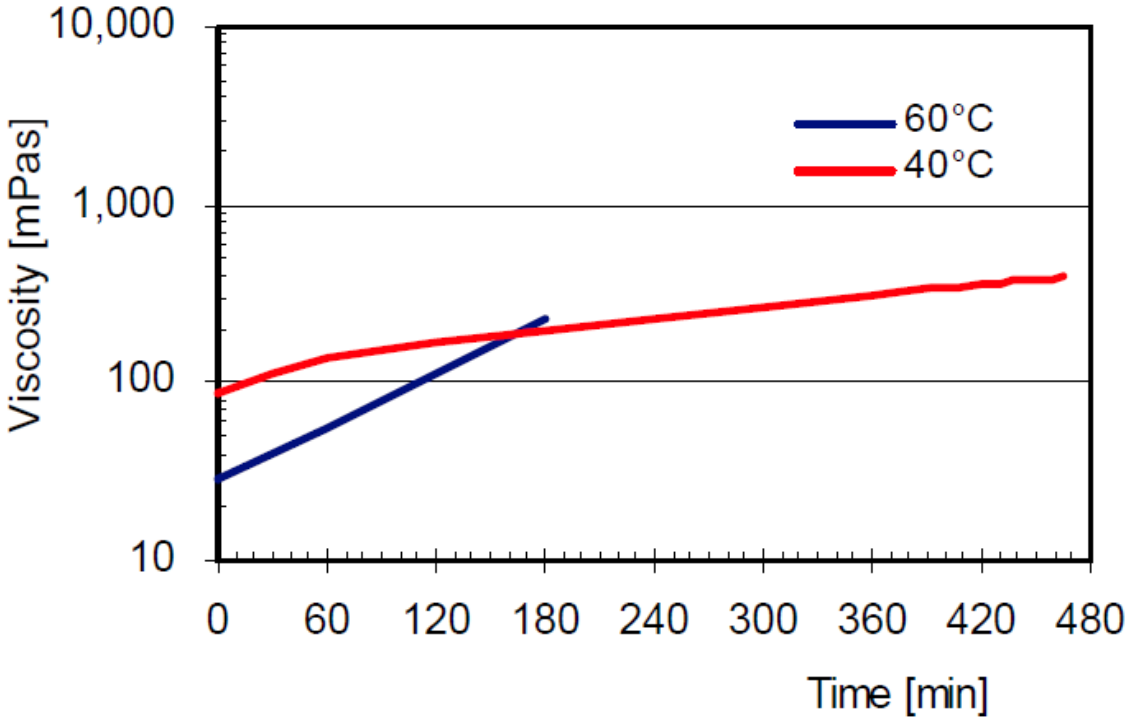

Fig. 3-6 XNR/H6809 Isothermal mixture viscosity

Table 3-3 Physical properties of the epoxy resin

Item	Value	Test Method
Density	1.22 g/cm^3	
Mixture viscosity (25°C)	260 mPa•s	
Tensile strength	86 MPa	ISO 527-1
Tensile Modulus	3.3 GPa	ISO 527-1
Compressive strength	115 MPa	ISO 604
Compressive Modulus	3.1 GPa	ISO 604
Flexural strength	135 MPa	ISO 178
Flexural Modulus	3.2 GPa	ISO 178

5. Infusion

Infusion is the most important step in the VaRTM process, which the quality of the quasi-UD woven fabric composite depends on. A more complicated layout than the hot compaction step is set up as Fig. 3-7. The big peeling film is placed onto the center of the tool, and the heating plate is turned on at 50 °C to keep the sealant tape at a good performance. The dry preform after the hot compaction is put on the big peeling film and covered by the small peeling film, the punching metal and the distribution medium in sequence. The distribution medium makes the resin flow successful. Resin inlet tubes are positioned above the center of the dry preform to enable the resin to fully wet out the dry preform prior to the resin gel. Vacuum outlet tubes connected to a vacuum system are positioned at the two sides of the dry preform. The dry preform is covered with the vacuum bagging film and sealant tape. The bagging film is positioned so as to

prevent bridging. The resin line is inserted into a resin tank of the mixed liquid epoxy resin. The clamp for injection tube is used to control the resin line. The epoxy resin is forced through the dry preform by the pressure differential between the inlet and the outlets when the line is opened. The outlet lines are connected to the resin trap, which is able to prevent the epoxy resin to be vacuumed into the vacuum pump. Moreover, the pressure of resin trap is detected by the pressure sensor, and the two-way solenoid valve open and close the vacuum line based on the value of the pressure sensor. The total setup of the infusion step is shown in as Fig. 3-8. Before the infusion, a leak test is performed as the line is closed, and the vacuum pressure (-96~-95 kPa) is applied to the dry preform. After the dry preform is fully wetted out, the infusion step is completed.

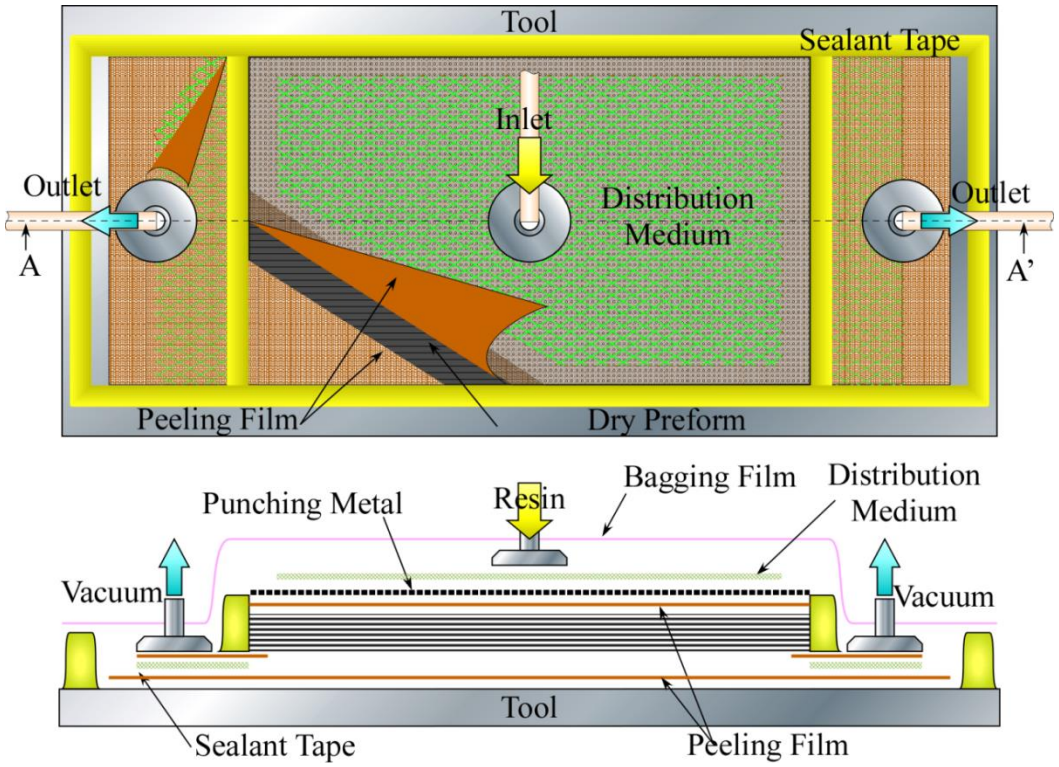

Fig. 3-7 A layout of infusion

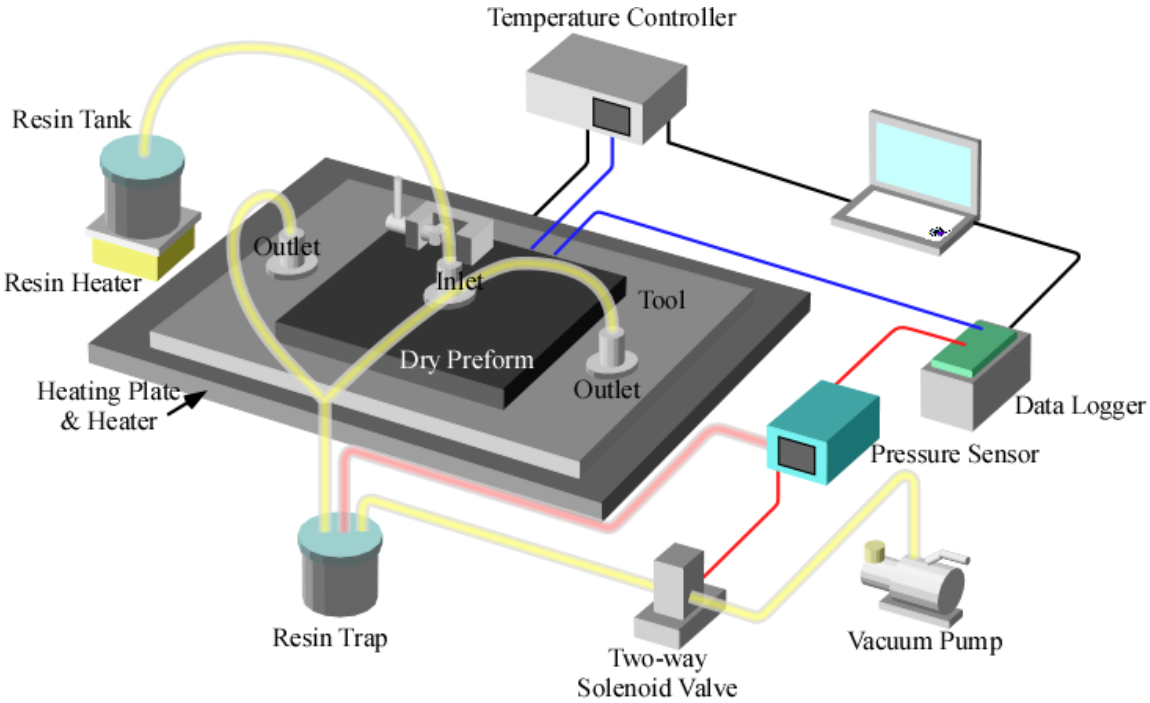

Fig. 3-8 A setup of infusion

6. Curing, post curing and demolding

The consolidation step of the dry preform and liquid epoxy resin are readied after the infusion step. The resin line is closed, and the vacuum pressure is decreased to -11~-10 kPa. The dry preform is allowed to initially cure at an elevated temperature on the heating plate. The curing time is 16 hours at 80 °C and post curing is 2 hours at 120 °C, which is controlled by the temperature controller and heating process from a computer. After the curing and post curing, the quasi-UD woven fabric composite cools down naturally. The composite is then removed from the tool, the process materials removed, and finally trimmed.

Three quasi-UD woven fabric composites, named laminate SP, LP and TP respectively, were fabricated via the VaRTM process, which are shown in Table 3-4.

Table 3-4 VaRTM process of three quasi-UD woven fabric composites

Laminate			SP	LP	TP
Fabric			Standard pitch fabric	Long pitch fabric	Thin pitch fabric
Lay		[ply]	16		24
Stacking sequence			$[45/0/-45/90]_{2S}$		$[45/0/-45/90]_{3S}$
Size		[mm]	165 × 140		
Areal weights		w_f [g/m^2]	316	319	199
Fiber density		ρ_f [g/cm^3]	1.81		
Fiber volume fraction		V_f [%]	61.0	57.7	48.9
Thickness	Average	t [mm]	4.59	4.89	5.40
	S.D.	[mm]	0.030	0.125	0.093
	C.V.	[%]	0.64	2.56	1.71
Hot Compaction	Time	[min]	60		
	Temperature	[°C]	150		
	Pressure	[kPa]	-86~-85		
Epoxy resin	Individual degassing	Time [min]	180		
		Temperature [°C]	50		
		Pressure [kPa]	-101		
	Mixed degassing	Time [min]	60		
		Temperature [°C]	50		
		Pressure [kPa]	-101		
		Rotate speed [rpm]	100		
Infusion	Degassing	Time [min]	60		
		Temperature [°C]	50		
		Pressure [kPa]	-96~-95		
	Saturating	Time [min]	150		

		Temperature [°C]	50
		Pressure [kPa]	-96~-95
Curing	Time	[hour]	16
	Temperature	[°C]	80
	Pressure	[kPa]	-10~-11
Post curing	Time	[min]	120
	Temperature	[°C]	120
	Pressure	[kPa]	-10~-11

3.3 Ultrasonic testing

The ultrasonic testing is performed after the VaRTM process to detect the quality of the quasi-UD woven fabric composite, which is a type of non-destructive testing techniques based on the propagation of ultrasonic waves in the material tested. G-SCAN 6AX500 from GNES corp. is used for the ultrasonic testing in a tank of water, and is shown in Fig. 3-9. It is also called immersion testing [68]. The transducer is placed in the water at an optimum depth, above the test material, projects a very short pulse of ultrasound into the material. The transducer at 5MHz is installed for the quasi-UD woven fabric composite. The front, flaw and back surface of the material along thickness direction reflect the pulse. After ultrasonic operate receive and analyze the reflected pulses, and the front wall peak flaw wall peak and the back wall peak are displayed on a screen. Due to some energy is lost when the waves propagate in the water and hit the material, the amplitude of the peaks decrease obviously. Therefore, distance amplitude correction (DAC) is used to evaluate the reflected signals and adjust the amplitude.

Fig. 3-9 G-SCAN 6AX500

The scanning results consist of A-scope, B-scope and C-scope [69]. The A-scope is the original radar display at one point, which shows the amplified reflected signal received from the transducer into the Y-axis of the display. The B-scope provides a distribution of reflected signal strength of the tested material in a transverse section, with the axes typically representing range and the thickness axis azimuth respectively. The C-scope displays a 2-D "top down" distribution of reflected signal strength, and overlays a graphical representation of the range to tested material.

The scanning results of the laminate SP, LP and TP are shown in Figs. 3-10 to 3-12, respectively. The blue color means that the reflected signal strength is weak, which indicates the scanned area is health. In contrast, the red color shows a delamination or void is in the scanned area. In the case of the laminate SP (Fig. 3-10), there are a green line at -45° in the bottom right corner of the C-scope result, which caused by a small discontinued fabric at the 45° ply. Therefore, the area for making specimens should avoid that part. Some flaws shown as red color are at the bottom of the laminate LP in Fig. 3-11, the possible reason is that the resin didn't fully wet off the area. Moreover, some yellow blockages exist in a line of 90°, which corresponds to the weft yarns of quasi-UD woven fabrics. The existence of the yellow blockages means the weft yarns may cause a discontinuity between the carbon fibers and glass fibers or epoxy resin. The laminate TP have the same problem as well as the laminate SP, there is a yellow triangle area in the left bottom corner in Fig. 3-12. Therefore, that area will be cut off in the process of manufacturing specimens.

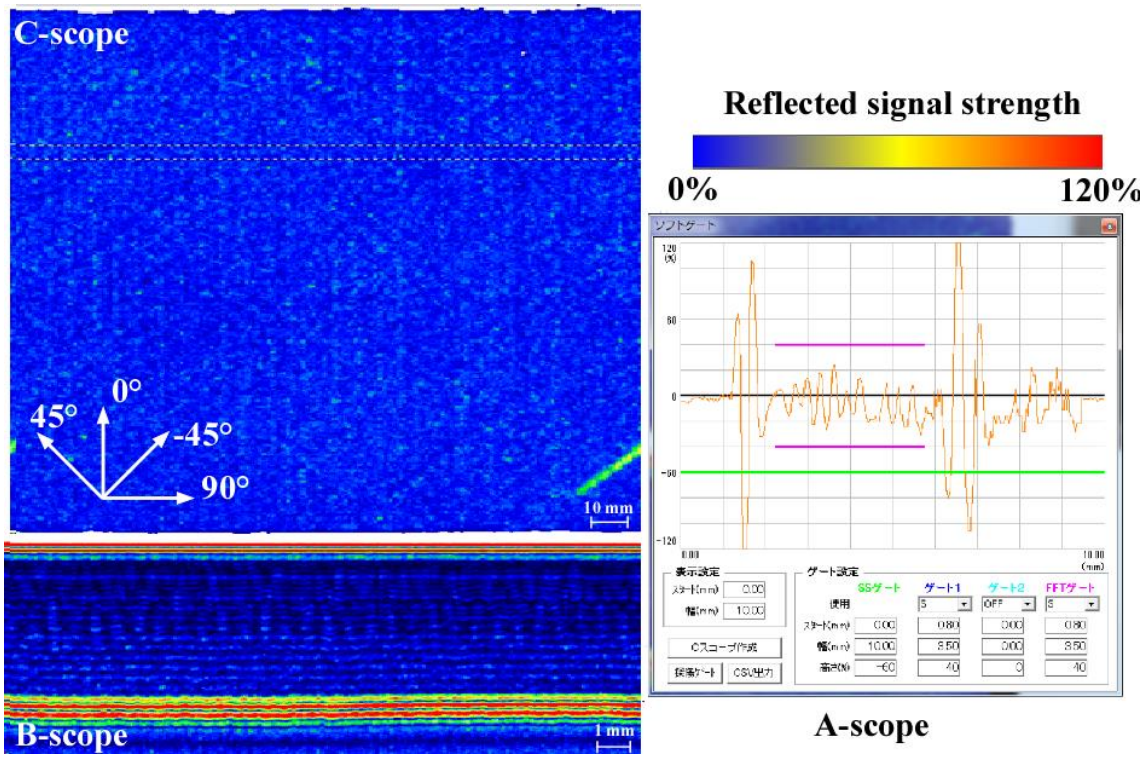

Fig. 3-10 Scanning results of the laminate SP

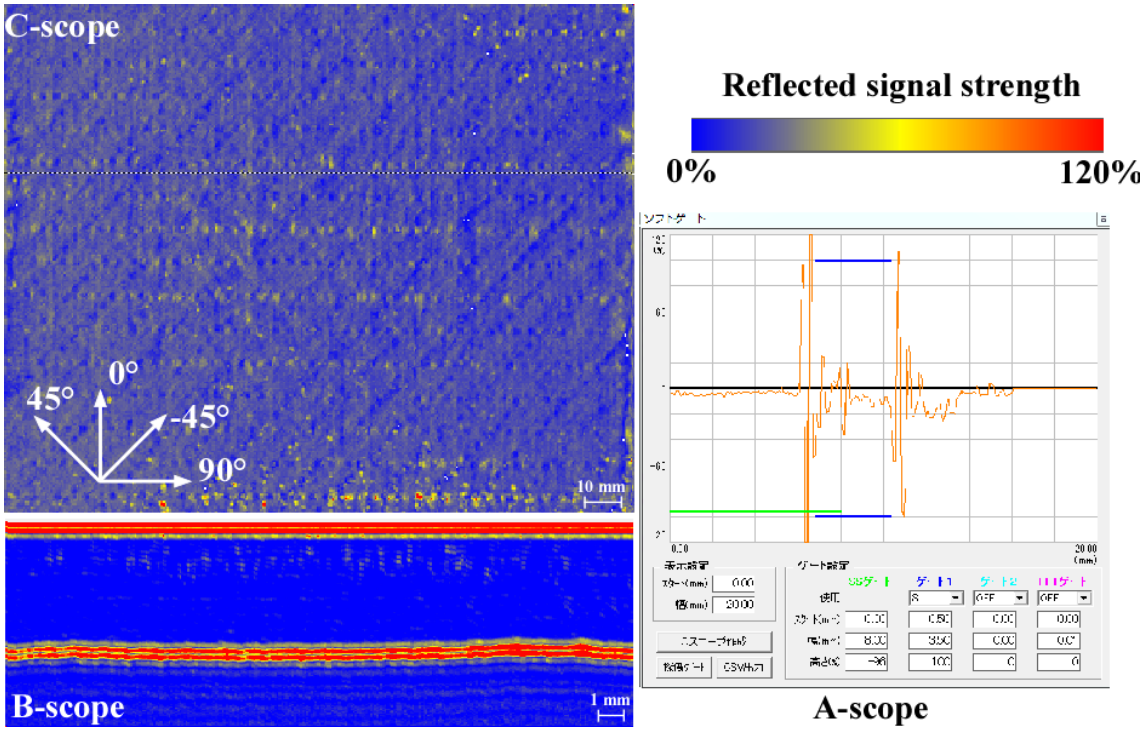

Fig. 3-11 Scanning results of the laminate LP

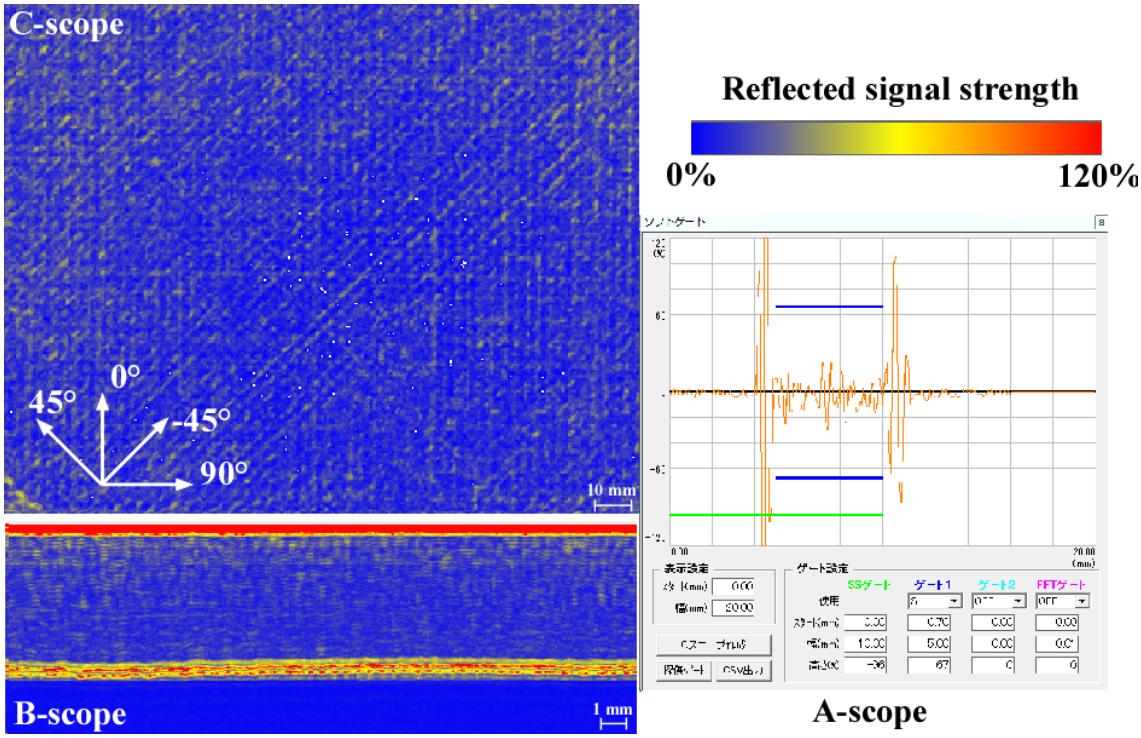

Fig. 3-12 Scanning results of the laminate TP

Chapter 4

Evaluation of out-of-plane fiber waviness

4.1 Out-of-plane fiber waviness

Out-of-plane fiber waviness is a negative effect on the compressive modulus and strength. Fig. 4-1 shows an example of the out-of-plane fiber waviness in a laminate fabricated by the woven fabrics [70]. The curved bright plies correspond to the 0° plies of carbon fibers, in contrast, the other colors are the region with other degreed plies such as 90° and 45° plies. It is obvious that curved 0° plies of carbon fibers reduce the compressive properties of the woven fabrics composites. However, in quasi-UD woven fabrics, the out-of-plane fiber waviness is much lower than that in the woven fabrics. Therefore, a three-step method based on an FFT is performed to obtain the characteristics of the out-of-plane fiber waviness in the laminate SP, LP and TP.

Fig. 4-1 Out-of-plane fiber waviness in a woven fabric laminate

4.2 Inspection method of out-of-plane fiber waviness

A brief introduction of this three-step method is given below, and more details can be found in a previous study [63,64].

a. Photographing a transverse cross section of the laminate in the length direction

A setup for photographing is shown in Fig. 4-2. The camera is Nikon D70, which is fixed on a workbench. A transverse cross section of the laminate should be polished first to make the 0° plies bright enough, and then is placed on the workbench as well to photograph. Moreover, a ruler is attached to the transverse cross section as a length scale. After that, several photographs of a transverse cross section of the laminate are taken in the lengthwise direction and combine into a montage in the software Microsoft ICE, as shown in Fig. 4-3(a). The stacking sequence of the laminate is $[45/0/-45/90]_{2S}$, as mentioned above, and the bright plies labeled "P1," "P2," "P3," and "P4" in the figure correspond to the 0° plie.

Fig. 4-2 A setup for photographing

b. Thinning process for 0° plies

After the montage of the transverse cross section is obtained, the bright plies corresponding to the 0° plies are treated as lines in desired region via the thinning process in the software CANVAS. Some operations like threshold, dedust and brush are conducted to remove noise and whiten the 0° plies. The white 0° plies are inverted to black by an invert operation. Then a skeletonizing operation is able to treat the 0° plies to thin lines, as shown in Fig. 4-3(b). In order to output pixel coordinates of points in each line, the treated montage is saved as a BPM file, and then exports a TXT Raw file. The pixel coordinates of points in TXT Raw file is translated to location information in a new

coordinate system whose *x*-axis is thickness direction and *y*-axis is length direction respectively, by a Fortran program UNERI.

c. Data processing based on the FFT

The location information of points in each line is input to EXCEL, and a possible slope of the laminate to the camera is corrected by fitting and averaging the angle of each line. Afterward, a Fortran program based on the FFT is utilized to analyze the corrected location information, which translates location information along the length direction to a amplitude distribution along spatial frequencies. Fig. 4-3(c) shows a typical relationship of the out-of-plane amplitudes A_{out} and the spatial frequencies f of each 0° ply. Each spatial frequency correspond to a amplitude, and the spatial frequency with the maximum amplitude associates with a characteristic wavelength L_c of the fiber waviness in each 0° ply, and the L_c is calculated using Eq. 4. In general, the characteristic wavelength of the fiber waviness L_c is equal to the wavelength L_w of the quasi-UD woven fabrics, as shown in Eq. (4-1). The reason is the weft yarns exist at a constant pitch interval and cause the warp tows of carbon fibers up and down, then this periodical fluctuation of the warp tows produce the out-of-plane fiber waviness of 0° ply and is detected by the FFT analysis.

$$L_c = \frac{1}{f} \tag{4-1}$$

$$L_c = L_w \tag{4-2}$$

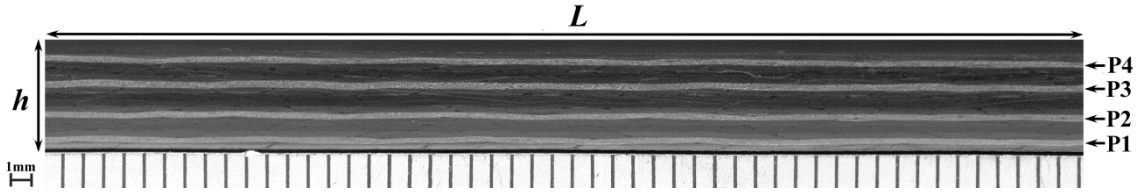

(a)

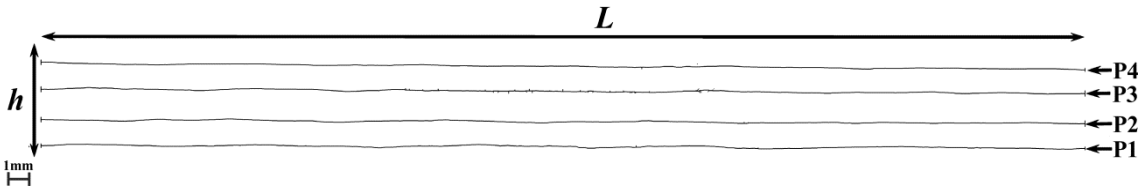

(b)

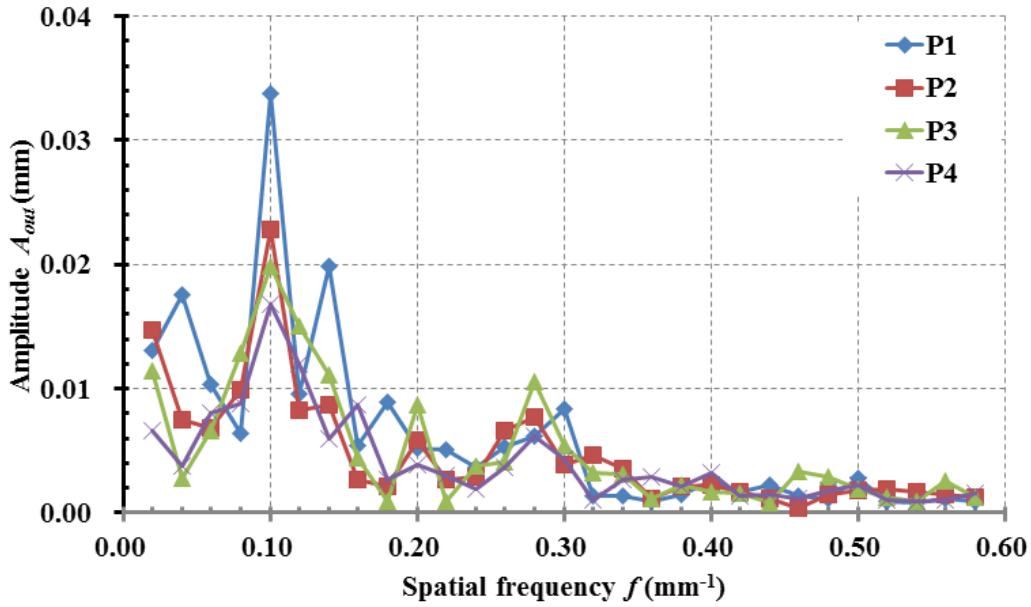

(c)

Fig. 4-3 Three-step method for characterizing fiber waviness: (a) photographing transverse cross section, (b) thinning process for 0° layers, and (c) data processing.

4.3 Evaluation results of out-of-plane fiber waviness

The inspections of out-of-plane fiber waviness were conducted on two sections of fiver specimens of the laminate SP, LP and TP respectively, and the relationships between the out-of-plane wave amplitudes, A_{out}, and spatial frequencies, f, in each laminate are shown in Fig. 4-4 to 4-6, respectively.

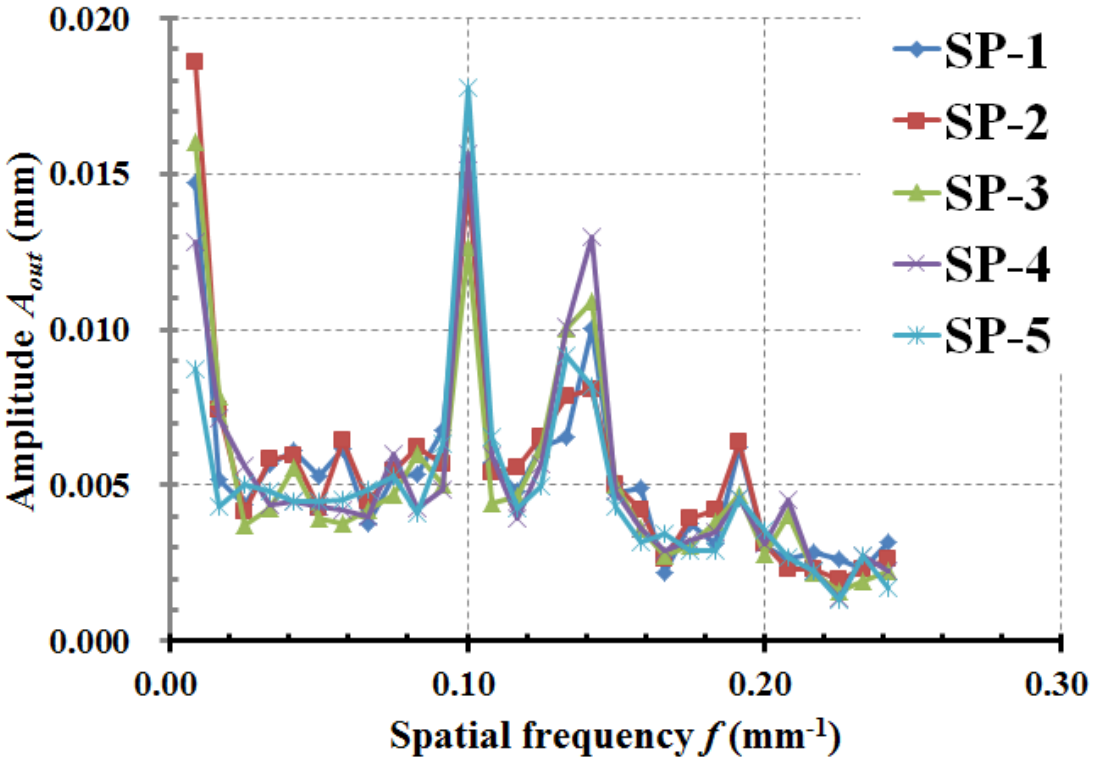

Fig. 4-4 Relationship between amplitudes and spatial frequencies in laminates SP.

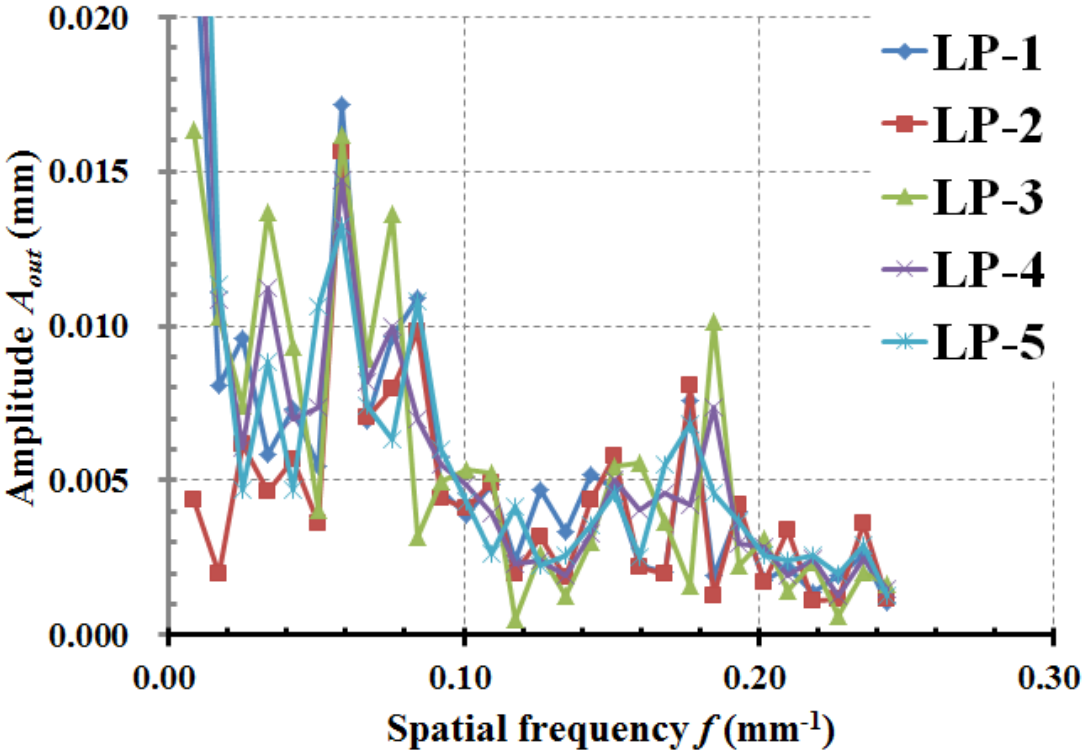

Fig. 4-5 Relationship between amplitudes and spatial frequencies in laminates LP.

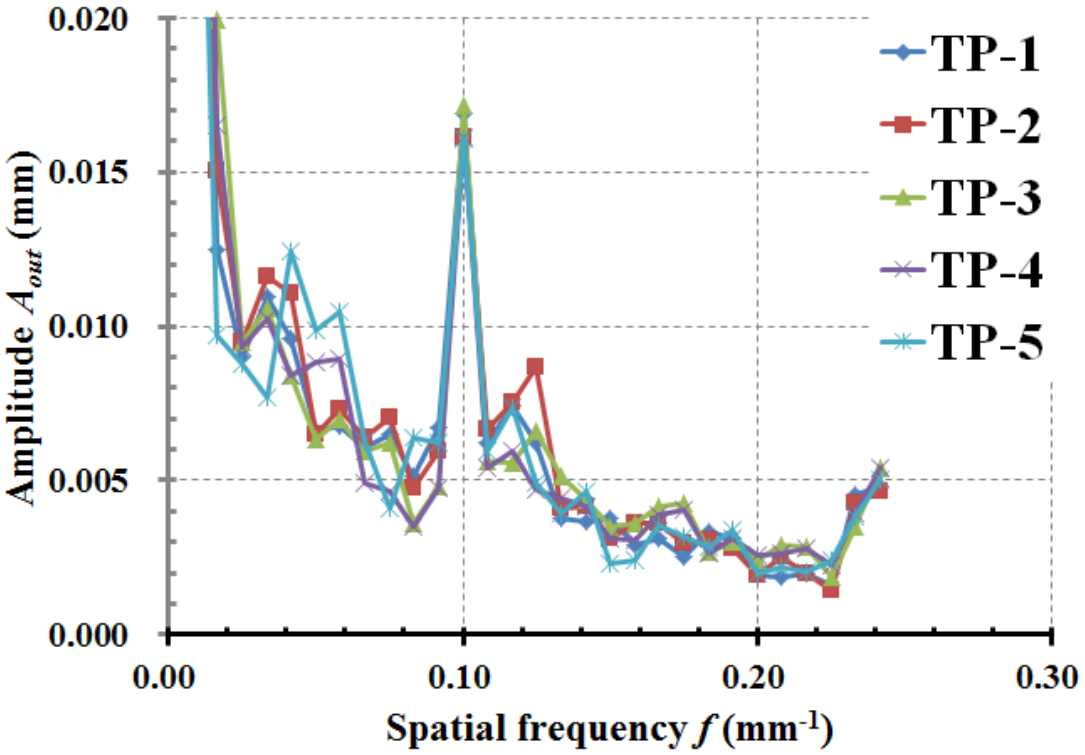

Fig. 4-6 Relationship between amplitudes and spatial frequencies in laminates TP.

In the specimens of laminate SP, the relationships between the out-of-plane wave amplitudes and spatial frequencies are shown in Fig. 4-4. We can find several peaks of the out-of-plane wave amplitudes at the different spatial frequencies are in this figure, which means the out-of-plane fiber waviness is able to be divided into some different fiber waviness. Moreover, the spatial frequencies with the maximum wave amplitude dominate the configuration of the out-of-plane fiber waviness. Therefore, we use spatial frequency at the maximum wave amplitude as characteristic waviness to represent the out-of-plane fiber waviness [63]. For example, the spatial frequencies with the maximum wave amplitude are 0.10 mm^{-1}, which corresponds to a characteristic wavelength of 10 mm. we measured that the wavelength in the SP fabric is 10.16 mm, which agrees with the characteristic wavelength well. Therefore, we can believe that the characteristic waviness is from the pitch interval of the fabrics and the three-step method based on an FFT is able to abstract the out-of-plane fiber waviness from the laminates. The out-of-plane wave amplitudes at the characteristic wavelength are from 0.0127 mm to 0.0178 mm, which means the wave amplitudes may be varied in the different location of the laminate and local configuration of fiber tows. However, the out-of-plane fiber waviness is only measured on the cross-sections of the specimens, to obtain the characteristic wave amplitude of the laminate SP, we averaged wave

amplitude of the five specimens and it is 0.0152 mm. If we simplify the out-of-plane fiber waviness to a sinusoidal function, the maximum fiber misalignment angle of the out-of-plane fiber waviness, θ_{0out}, is calculated as Eq. (4-3) and it is 0.55° in laminate SP.

$$\theta_{0out} = \frac{2\pi A_{out}}{L_w} \tag{4-3}$$

In the laminate LP, the characteristic wavelength is 16.7 mm at the spatial frequency 0.06 mm^{-1} as shown in Fig. 4-5, the corresponding out-of-plane wave amplitude is from 0.0132 mm to 0.0171 mm and average wave amplitude of the five specimens is 0.0158 mm. The corresponding maximum fiber misalignment angle is 0.34°. In the laminate TP (Fig. 4-6), the out-of-plane fiber waviness is from 0.0161 mm to 0.0171 mm. Average wave amplitude of the five specimens is 0.0166 mm at the characteristic wavelength 10 mm, which corresponds to the maximum fiber misalignment angle of 0.60°.

Fig. 4-7 shows the relationships between the average out-of-plane wave amplitudes and spatial frequencies in laminate SP, LP and TP, respectively. The laminate SP and TP have the same characteristic wavelength of 10 mm due to the same pitch interval of the SP and TP fabrics. The characteristic wavelength of the laminate LP is longer than the laminate SP and TP because of the longer pitch interval of the LP fabric than the SP and TP fabrics. The out-of-plane wave amplitude in these three laminates are close to 0.015

mm because the weft yarns in the SP, LP and TP fabrics are all ECD450 1/2 4.4S weft yarns of glass fiber. It should be noticed that there are many influences on the inspection results, for instance, human deviation may be from the nonplanar transverse cross sections of inspected specimens or poor quality of merged montages; the inspected position affects the out-of-plane wave amplitude; both the characteristic wavelength and the amplitude depend on the architectures of the quasi-UD woven fabrics, fiber volume fraction associated with the thickness and the stacking sequence of the laminates.

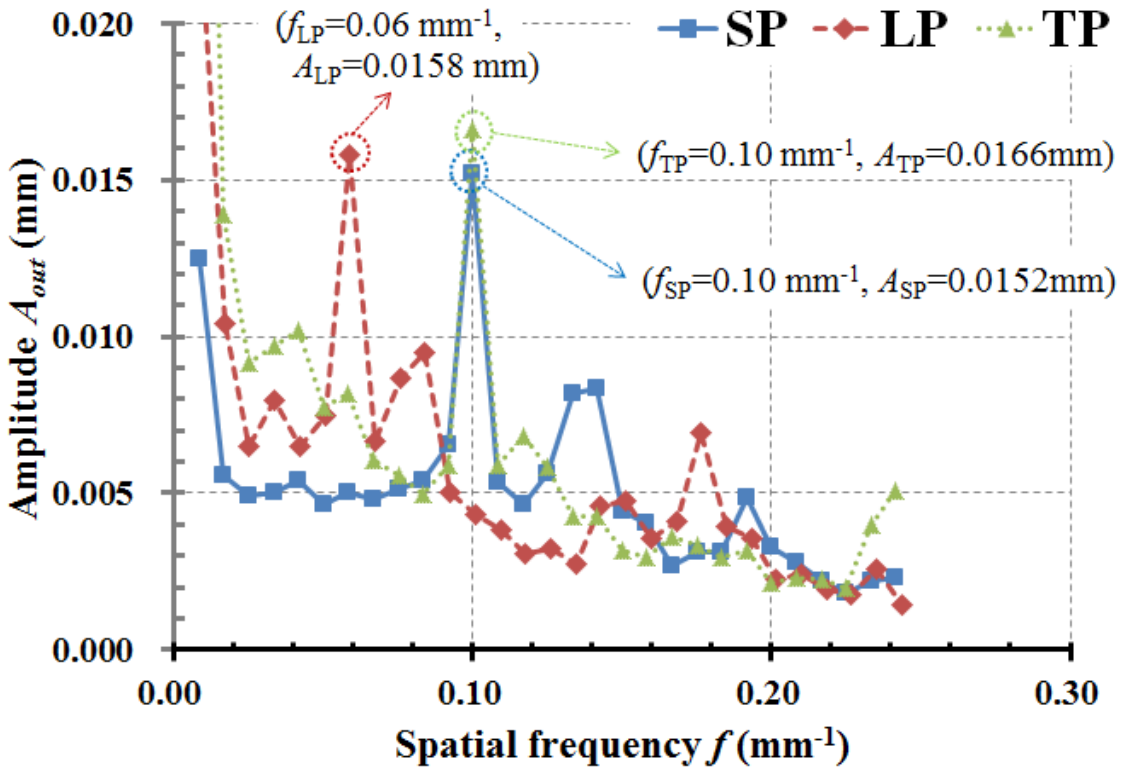

Fig. 4-7 Relationships between average amplitudes and spatial frequencies in laminates SP, LP and TP.

A ratio R_{out} is used to evaluate the relationships between the out-of-plane wave amplitude and wavelength of the quasi-UD woven fabrics, as shown in Eq. (4-4).

$$R_{out} = \frac{A_{out}}{L_w} \tag{4}$$

We can find the relationship of the ratio and the maximum fiber misalignment angle as follows:

$$R_{out} = \frac{\theta_{0out}}{2\pi} \tag{5}$$

Therefore, the maximum fiber misalignment angle is able to be represented by the ratio.

Although the laminates SP, LP and TP have similar out-of-plane wave amplitudes, the R_{out} of the laminate LP is lower than that of the laminates SP and TP due to the wavelength of the laminate LP is longer than laminates SP and TP. Table 4-1 shows the data of in-plane and out-of-plane fiber waviness of the laminate SP, LP and TP. We can find that the major difference between the laminate SP and LP is the out-of-plane fiber waviness comparing with the in-plane fiber waviness. Therefore, the laminate SP and LP are grouped to study the effect of out-of-plane fiber waviness on the compressive strength. In contrast, the in-plane waviness ratio dominates the difference between the laminate SP and TP, thus the research on the effect of in-plane fiber waviness is conducted on the laminate SP and TP.

Table 4-1 Data of in-plane and out-of-plane fiber waviness of the laminate SP, LP and TP (Coefficient of variation shown in parentheses)

Laminate	SP	LP	TP
Fabric	Standard pitch fabric	Long pitch fabric	Thin pitch fabric
Wavelength L_w	10.16 mm (1.4%)	16.94 mm (0.7%)	10.14 mm (1.6%)
In-plane wave amplitude A_{in}	0.12 mm	0.18 mm	0.015 mm
Out-of-plane wave amplitude A_{out}	0.0152 mm	0.0158 mm	0.0166 mm
In-plane waviness ratio R_{in}	0.0117	0.0104	0.0015
Out-of-plane waviness ratio R_{out}	0.0015	0.0009	0.0016

Chapter 5

Compression tests

5.1 Standard test methods for compressive properties

There are standard test methods for compressive properties, namely, ASTM D3410, ASTM D695 and ASTM D6641 respectively.

ASTM D3410 [71] is a commonly shear-loaded test method, which uses the Celanese test fixture or the IITRI test fixture. The Celanese test fixture was first presented by Park of the Celanese Corporation in 1971 as shown in Fig. 5-1 [72]. The specimen is inserted between the two halves of each cone-shaped wedge grip, and assembled in close-fitting sleeve. However, it is very different to use because of its cone-in-cone arrangement of the wedge grips, which is a potential source of bending [73,74]. Moreover, the width and thickness of the specimen are limited by the cone-shaped wedge grip; the maximum width is 6.5 mm and the total thickness at the tabbed ends of the specimen with high modulus is 4.0 mm. Therefore, the IITRI test fixture was developed to improve the Celanese test fixture, which is shown in Fig. 5-2 [75]. Flat wedge grips replace the cone-shaped wedge grips and the close-fitting sleeve is replaced by alignment rods. Variable width and thickness specimens are valid in this fixture; the allowing width is from 6 mm to 25 mm and the total thickness depends on the gage length and the expected

compressive strength. The data obtained from the IITRI test fixture is much better than that from the Celanese test fixture. However, massive and costly to fabricate is major disadvantages of the IITRI test fixture. For example, the IITRI test fixture is more than 40 kg.

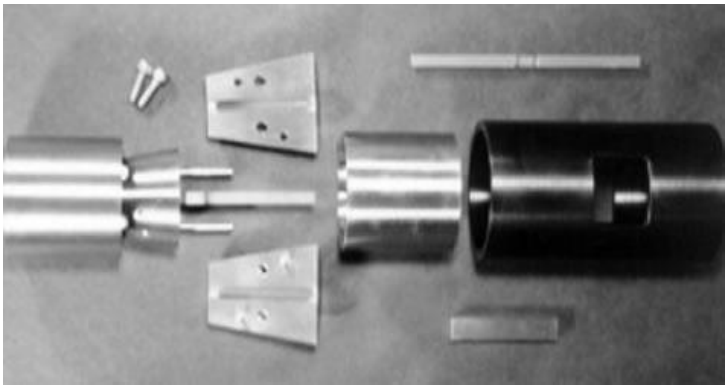

Fig. 5-1 Celanese test fixture

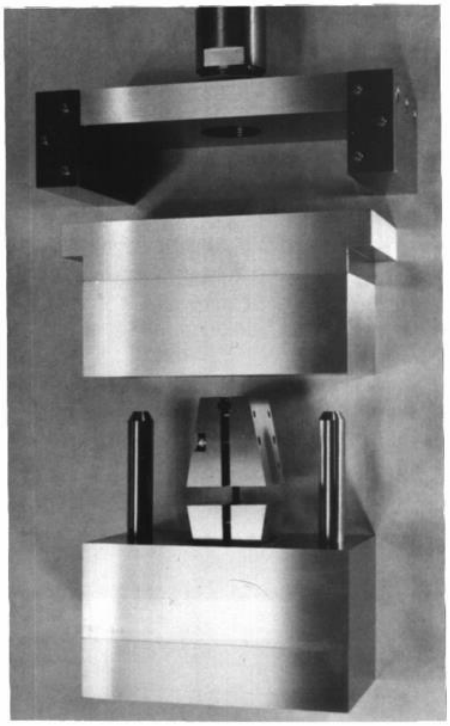

Fig. 5-2 IITRI test fixture

ASTM D695 [76] is a standard of an end-load compression test method. The test fixture for ASTM D695 is shown in Fig. 5-3 [77]. Two I-shaped support jigs and four bolts are used to support the specimen during testing. Two flat pieces are made of hardened steel and installed between the ends of the specimen and loading platen of the testing machine to protect the loading platen. This test method is used widely with reasonable success [78,79]. However, there are some problems in its usage: the specimen is cut to dog-boned shape to avoid stress concentrations at the ends of the specimen, which needs additional process to treat the specimen; due to no space to accommodate a strain gage, at least two specimens are needed, and one is to detect the compressive modulus and the other is for the compressive strength, which is time consuming and inefficient. Although adding tabs is able to solve the problems partly, specimen buckling should be concerned in specimens' size designing.

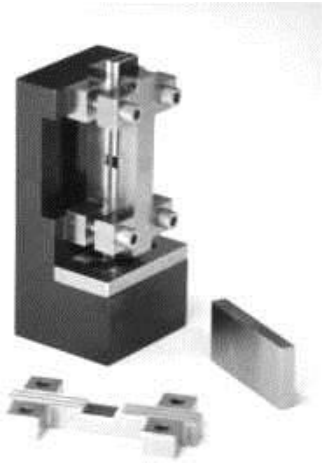

Fig 5-3 Test fixture for ASTM D695

ASTM D6641 [80] determines the compressive properties of CFRPs using a combined loading (combined end- and shear-loading) compression (CLC) test fixture. The CLC test fixture is shown in Fig. 5-4 [81]. The specimen is installed into the test fixture and clamped by the screws. The shear stress is provided by gripping surfaces coated with 100 grit tungsten carbide particles, and the ratio of end- and shear-loading is controlled by adjusting torque. In general, the torque depends on the type of material and the thickness of the specimen. For example, the ends of the specimen may crush if the torque is too low. Otherwise, if the torque is excessive, the high clamping force may lead to premature failures due to stress concentrations at the ends of the gage section. Thus, several trials for the adjusting torque may be needed to prevent end crushing. Some research has been shown that the acceptable range of torque is very broad [82,83]. Untabbed specimens are suitable in this test fixture, which make the specimens be prepared easily. However, the gripping surfaces with tungsten carbide particles may have to be recoated, moreover, the surfaces of the test fixture contacting to the loading platen of the testing machine may be plastic after long term use, which increases the cost of maintenance and repair.

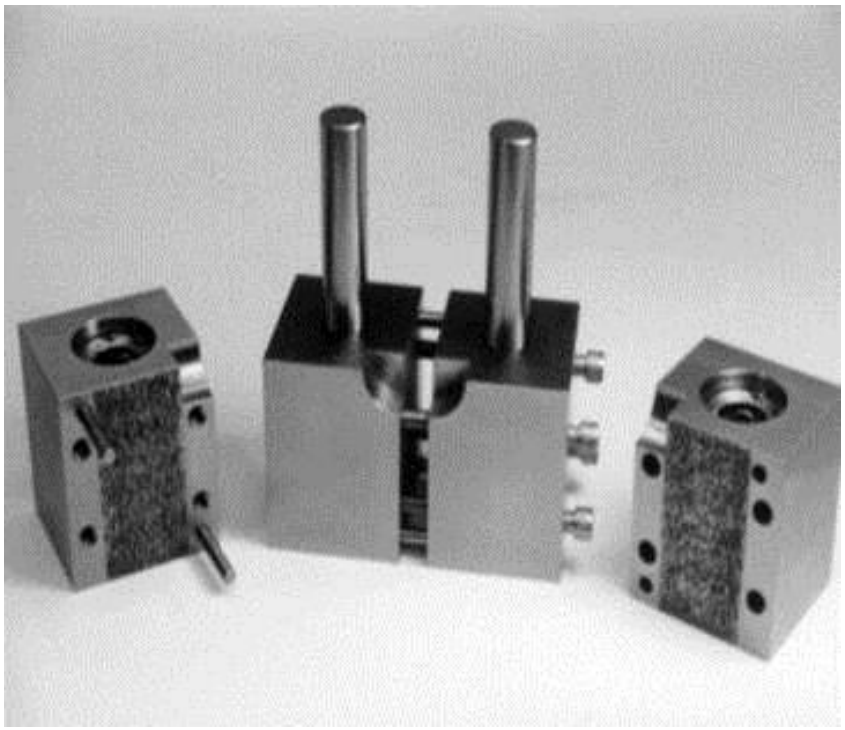

Fig. 5-4 CLC test fixture

5.2 A modified CLC test fixture for compressive properties

In our laboratory, a modified CLC test fixture is built base on the work of Shimokawa et al. [84], which is shown in Fig. 5-5. In this fixture, each end of the specimen is held in place by 50-mm-long binding grips. Steel blocks are then used to keep the specimen on the centerline of the fixture and a pair of supporting guides for the test fixture prevents an out-of-plane directional movement of the specimen [85]. Using double-sided tape, paper face of sand paper (80 grit) is then affixed to the block and abrasive material glued face of the sand paper contacts with the specimen (Fig. 5-6); thus the specimen undergoes shear loading owing to the clamping force exerted by eight screws of the fixture. This test method is able to prevent premature failure of the specimen at the grips as well as ASTM D6641 and the cost of the sand paper is lower than recoating tungsten carbide particles on the gripping surfaces of the CLC fixture. Moreover, two hardened steel flat pieces contacting to the ends of the specimen are also easy to be replaced if plastic deformation occurs on the flat pieces. Therefore, the modified CLC test fixture is able to be repaired more easily than the standard CLC test fixture.

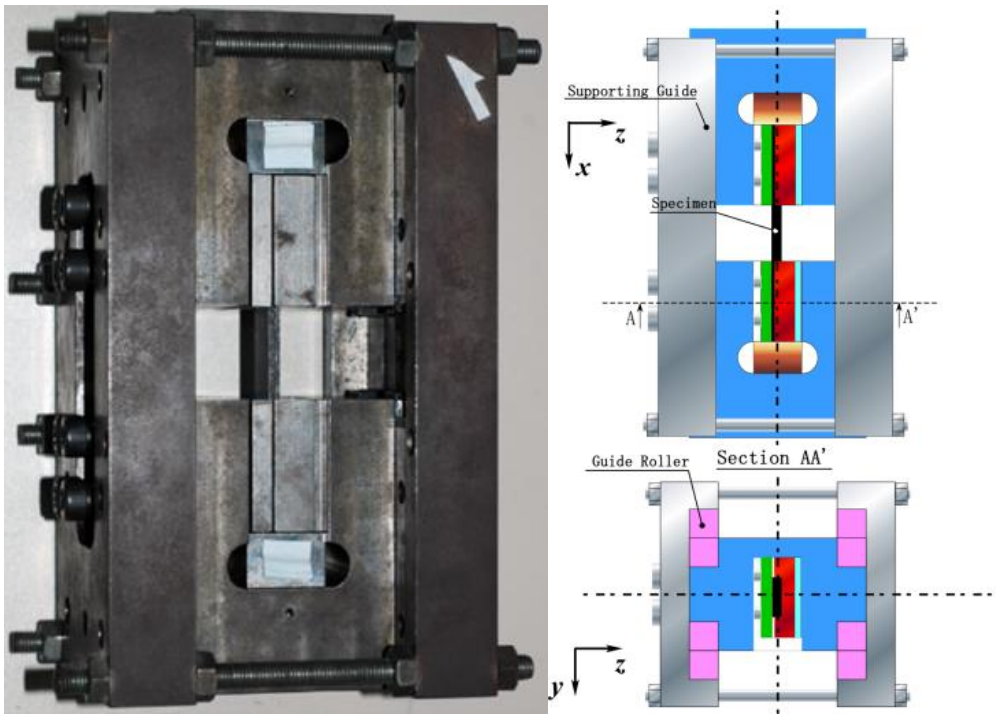

(a) (b)

Fig. 5-5. Compressive testing fixture: (a) schematic representation of fixture and specimen, and (b) photograph of fixture and specimen.

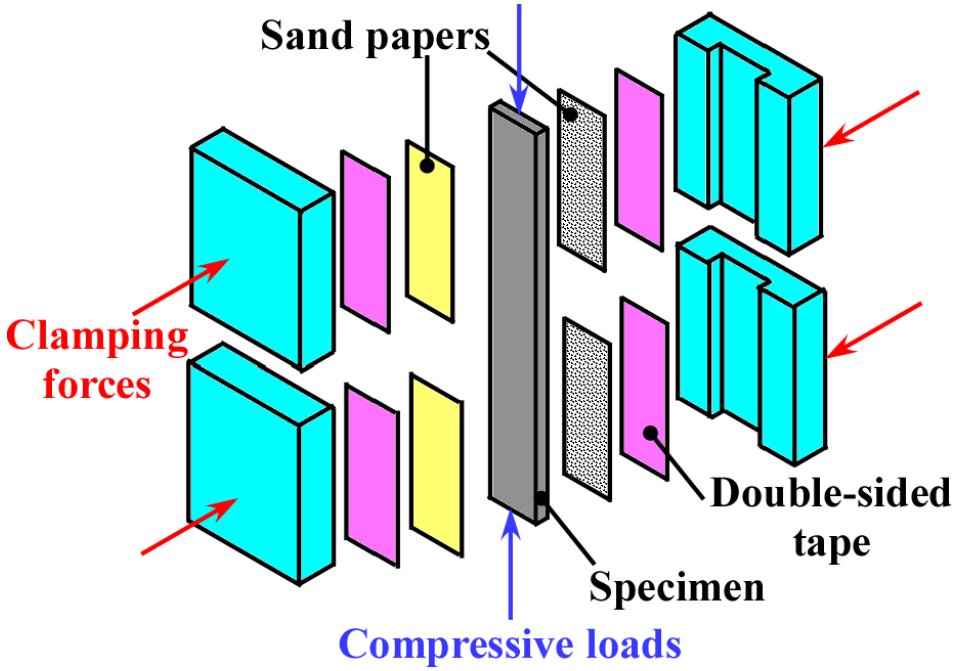

Fig. 5-6 Schematic showing forces on the specimen

5.3 Specimens for the modified CLC test fixture

As mentioned before, the quasi-isotropic lay-up: $[45/0/-45/90]_{ns}$ is used in this study, and similar overall thicknesses of the composite laminates are attained when n = 2 and n = 3 for the laminate SP, LP and TP, respectively.

Five 125 mm (length) × 15 mm (width) specimens of each type of laminate were subjected to compression tests. Each specimen is untabbed as shown in Fig. 5-7, which decreases the time consuming and material cost on the specimens. The combined loading on the specimen avoid the stress concentration on the ends of specimen. The resulting out-of-plane deflection is determined by uniaxial strain gages located back-to-back at the center of the each specimen. Considering the thickness of each specimen is about 5 mm, a central gage length 25 mm long is selected for a long gage area to accommodate strain gages, moreover, the thickness is greater than minimum required specimen thickness at 25 mm-gage length to prevent a global bucking of the specimen according to ASTM D 6641.

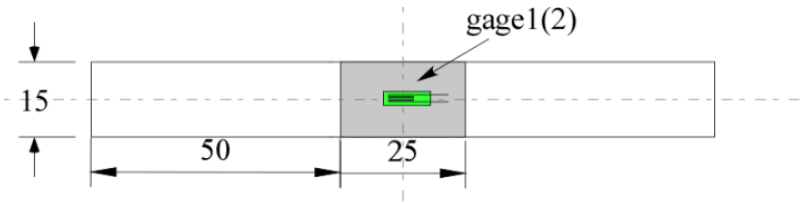

Fig. 5-7 Schematic showing specimen's dimensions

5.4 Procedure

This procedure bases on ASTM 6641, and modified for the modified CLC test fixture.

1. Measure the width and thickness at three places in the gage section of the specimen and calculate the specimen area at the three places. Record the area as the average of these three areas in units of mm^2.

2. Apply strain gages to both faces of the specimen as shown in Fig. 5-7 and keep them valid before tests.

3. Clean the accumulation of debris on the test fixture and screw before the testing and examine the gripping and loading surfaces are not damaged. Oils can spread onto the pair of supporting guides to ensure that it is operating smoothly. 80 grit sand papers are pasted on the surfaces of the specimen and the blocks with double-sided tape.

4. Put the test fixture down first. Select some steel blocks to keep the specimen on the centerline of the fixture and install the concave blocks in to the test fixture. Loosen the screws in both halves of the test fixture sufficiently to accommodate the specimen thickness to be tested.

5. Place the test specimen on the centerline of the fixture and clamp the specimen with the flat blocks. Slightly tighten the eight screws in the test fixture with fingers.

6. Place the test fixture on its side. Loosen the four screws in the lower half of the fixture to ensure that the end of the specimen is flush with the bottom surface of the fixture and then tighten these four screws.

7. Hold the upper blocks and loosen the four screws in the upper half of the fixture. Tighten the four screws after the end of the specimen is flush with the upper surface of the fixture.

8. Torque all eight of screws using a torque wrench. A diagonal tightening pattern at each end is used to let the fixture surfaces are uniformly clamped against the surfaces of the test specimen.

9. Place the assembled fixture between well-aligned, fixed flat platens in the testing machine (INSTRON 8501, ±100 kN). Attach the lead wires of the strain gages to the data acquisition apparatus.

10. Perform specimen alignment at the specimen stress of 1000 and 3000 microstrain and determine the compressive modulus of the specimen at this strain level. If bending of the specimen is occurring, the strains of the back to back strain gages will not be equal. In general, the percent bending must be kept to less than 10 % for compressive strength. Moreover, the average of these two values is the desired strain since the amount of

bending does not affect the average strain. The percent bending, P_b, is determined as follows:

$$P_b = \frac{\varepsilon_{bag} - \varepsilon_{tool}}{\varepsilon_{bag} + \varepsilon_{tool}} \cdot 100 \quad (4)$$

where

ε_{bag} and ε_{tool} are the strain on bag and tool side of the specimen, respectively.

11. Load the specimen in compression to failure at a nominal rate of 0.5 mm/min in 1 to 5 min, and record force, displacement and strain data.

12. Clean the test fixture and machine after the testing.

5.5 Experimental results

The results of the compression tests are shown in Table 5-1, and testing records of each specimen are shown from Fig. 5-8 to Fig. 5-22. As the table shows, P_b at failure is <10% in all cases, indicating that buckling did not occur in our experiments. The fiber volume fraction, V_f, of the specimens form laminate SP, LP and TP is 61.0%, 57.7% and 48.9%, respectively. Therefore, the averaged compressive modulus and strength of the SP specimens is greatest among the three laminates due to the highest the fiber volume fraction. However, the averaged failure strain of the SP specimens is lowest in the three laminates. Moreover, standard deviation on the compressive strength of the SP specimens is 6.8%, which is a little greater than the other laminates. There are many variations influencing the standard deviations among the SP specimens: the different out-of-plane fiber waviness in the different location; the void ratio; the parallelism at both ends of the specimens and the percent bending of the specimens during the compression tests. These variations may lead to the standard deviations of the SP specimens. Finally the experimental results of the laminates are analyzed to study the effect of out-of-plane and in-plane fiber waviness in Chapters 6 and 7 respectively.

Table 5-1. Experimentally determined properties of the SP, LP and TP specimens

	Young's modulus E_c [GPa]	Compressive strength F_c [MPa]	Fiber volume fraction V_f [%]	Failure strain F_s [με]	Percent bending at failure P_b [%]
SP-1	53.4	437.7	61.0	8645	0
SP-2	54.2	438.2	61.0	8492	0
SP-3	51.4	496.2	60.9	9748	4
SP-4	53.6	469.8	60.9	9335	4
SP-5	54.0	519.6	61.0	10470	1
SP-Average	53.3	472.3	61.0	9338.1	
S.D.	1.0	32.2	0.0	727.1	
C.V.	1.9%	6.8%	0.1%	7.8%	
LP-1	48.2	476.2	55.4	10714	-4
LP-2	50.4	451.7	58.9	9591	3
LP-3	50.3	489.6	58.8	10582	2
LP-4	52.0	469.3	56.6	9921	0
LP-5	54.6	458.3	58.9	9078	0
LP-Average	51.1	469.0	57.7	9977.1	
S.D.	2.1	13.4	1.5	611.5	
C.V.	4.1%	2.8%	2.5%	6.1%	
TP-1	41.4	427.0	48.1	11130	0
TP-2	40.9	410.8	48.4	10886	0
TP-3	42.2	391.2	48.9	9888	0
TP-4	43.5	417.8	49.5	10251	1
TP-5	43.0	420.5	49.7	10542	1
TP-Average	42.2	413.5	48.9	10539.4	
S.D.	1.0	12.3	0.6	442.0	
C.V.	2.3%	3.0%	1.3%	4.2%	

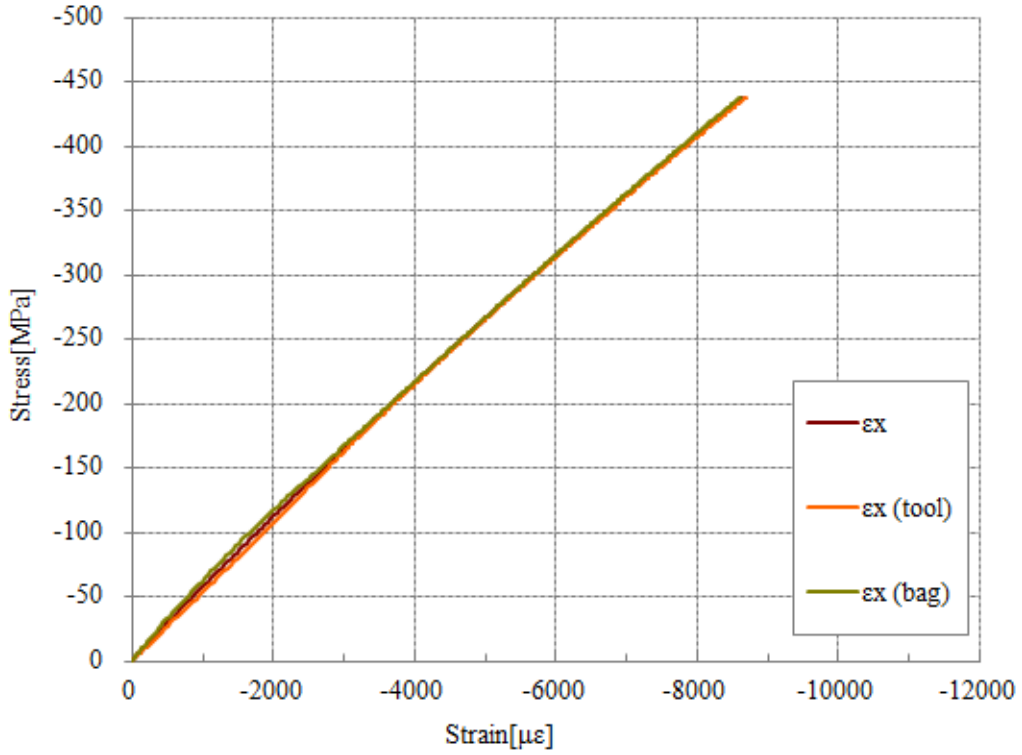

(a)

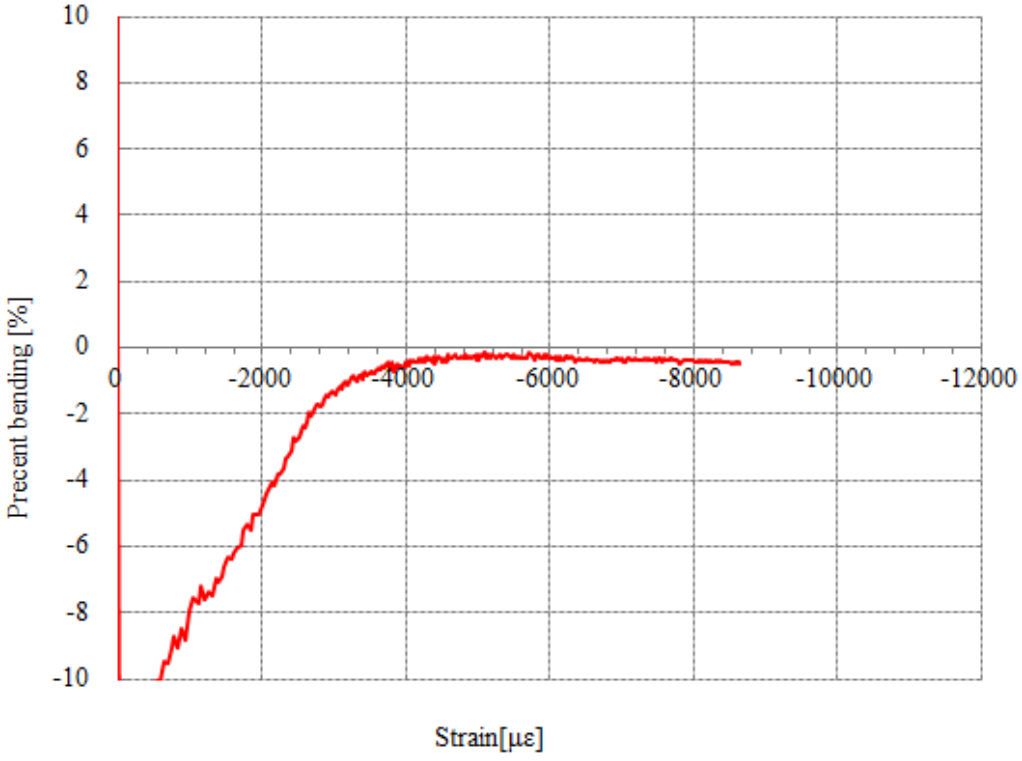

(b)

Fig. 5-8 Testing records of the specimen SP-1: (a) relationship of stress and strain and (b) percent bending

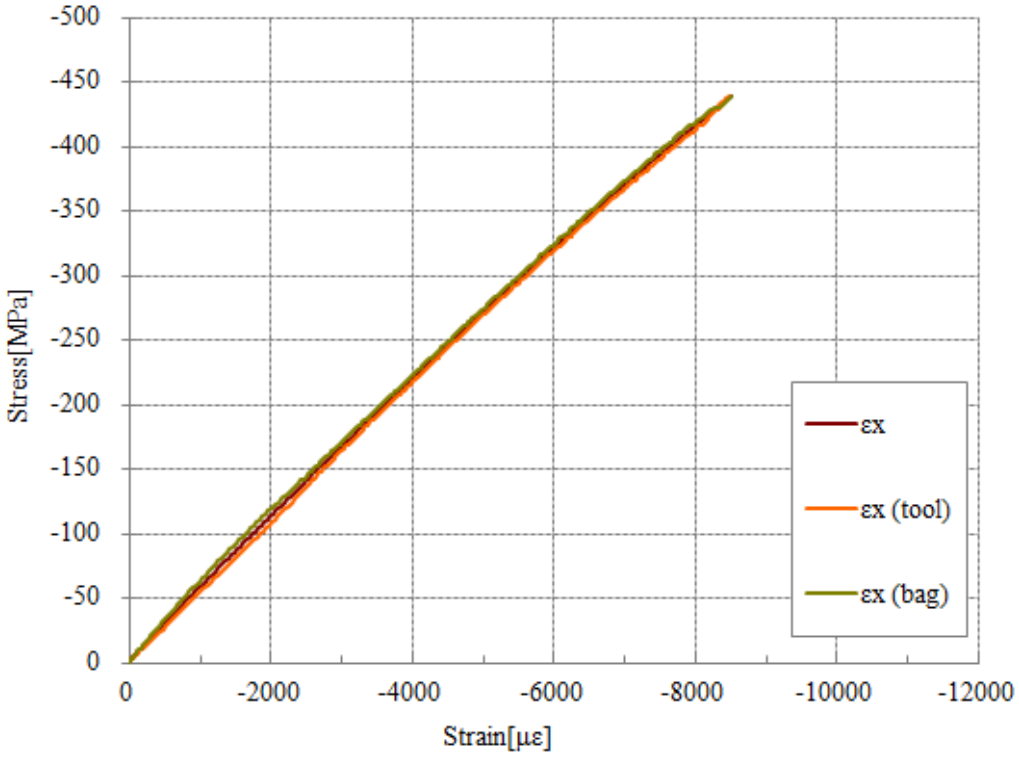

(a)

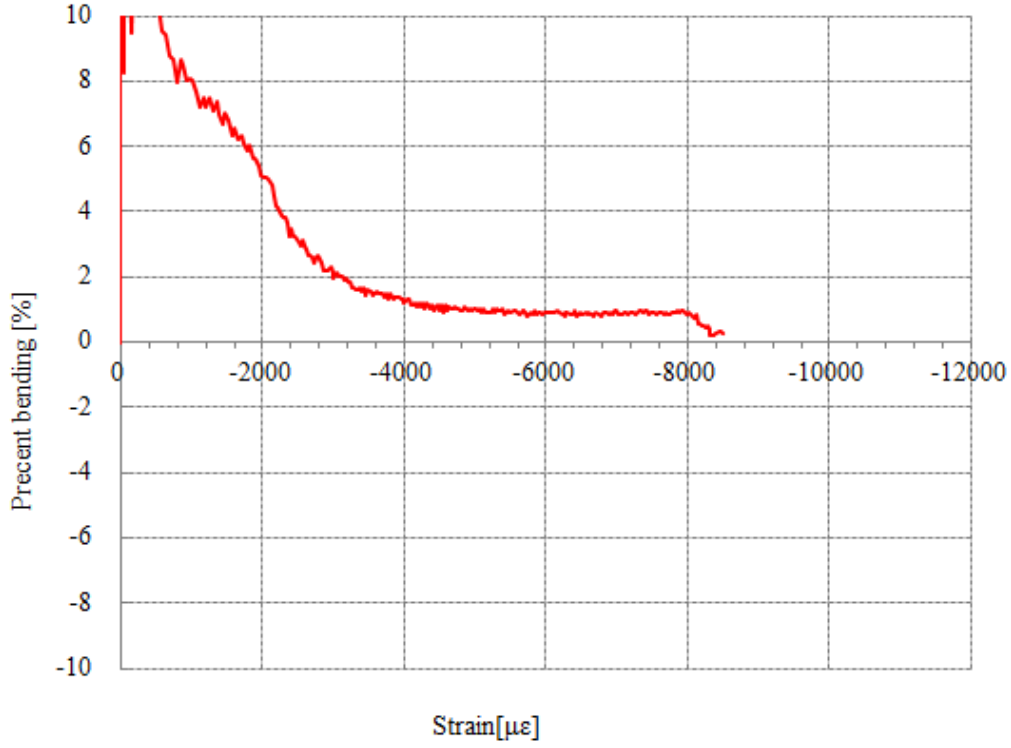

(b)

Fig. 5-9 Testing records of the specimen SP-2: (a) relationship of stress and strain and (b) percent bending

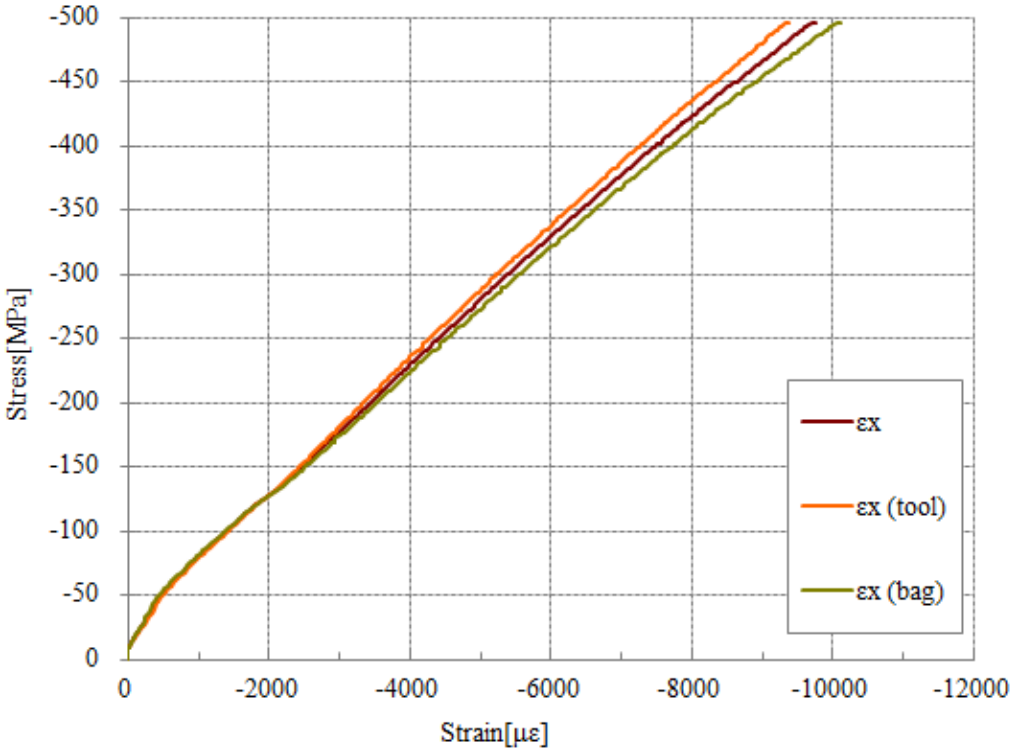

(a)

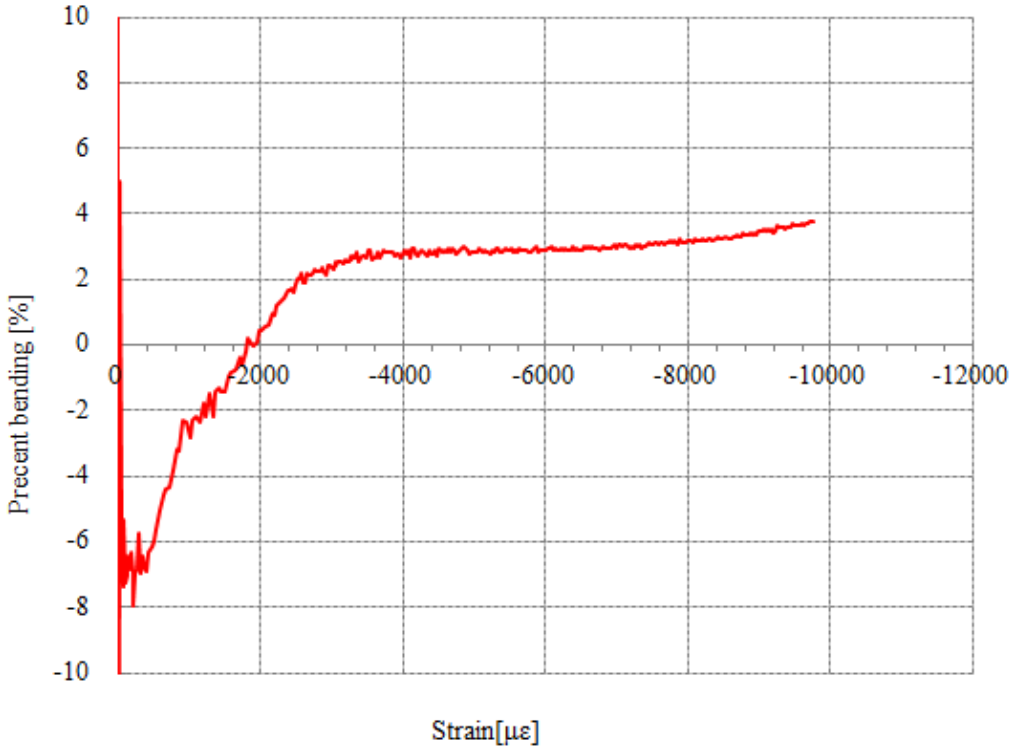

(b)

Fig. 5-10 Testing records of the specimen SP-3: (a) relationship of stress and strain and (b) percent bending

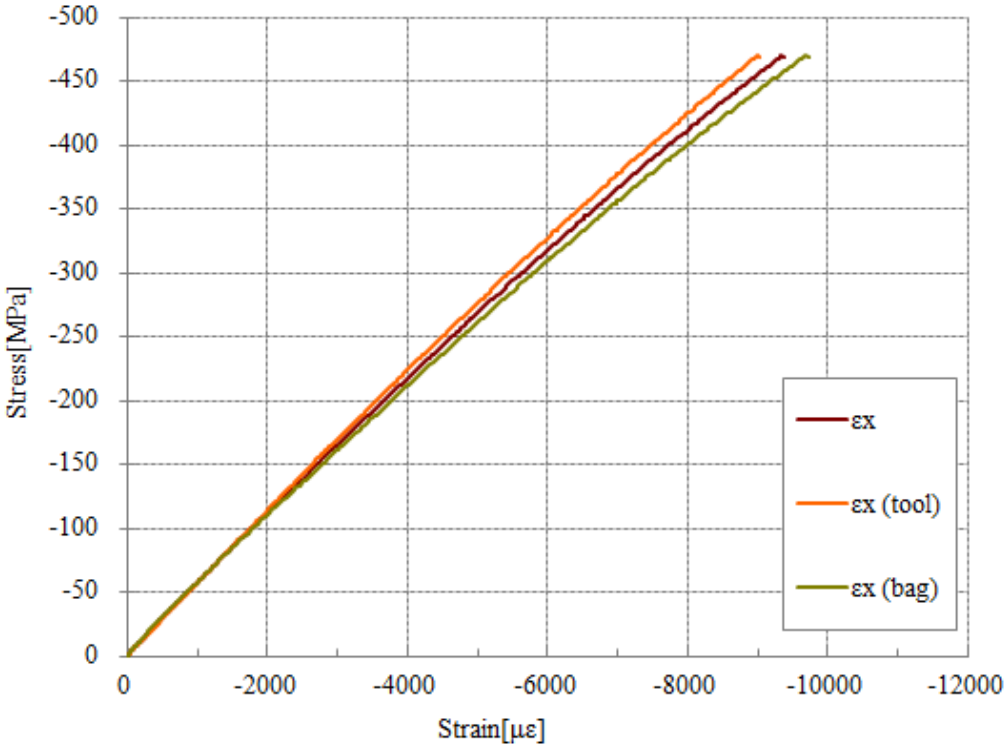

(a)

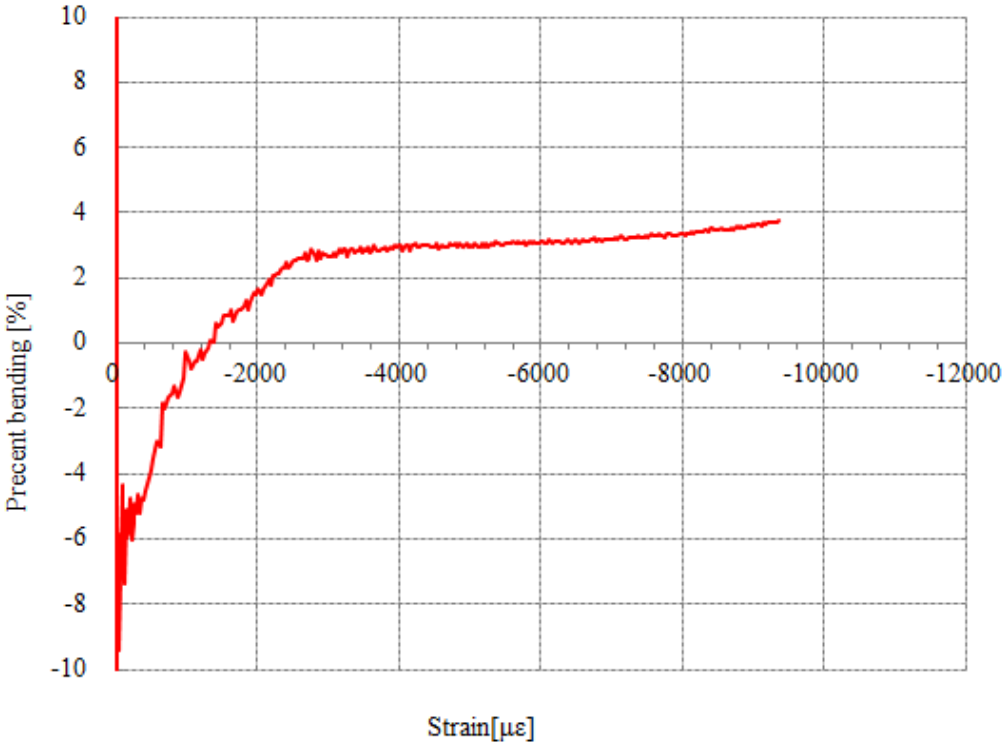

(b)

Fig. 5-11 Testing records of the specimen SP-4: (a) relationship of stress and strain and (b) percent bending

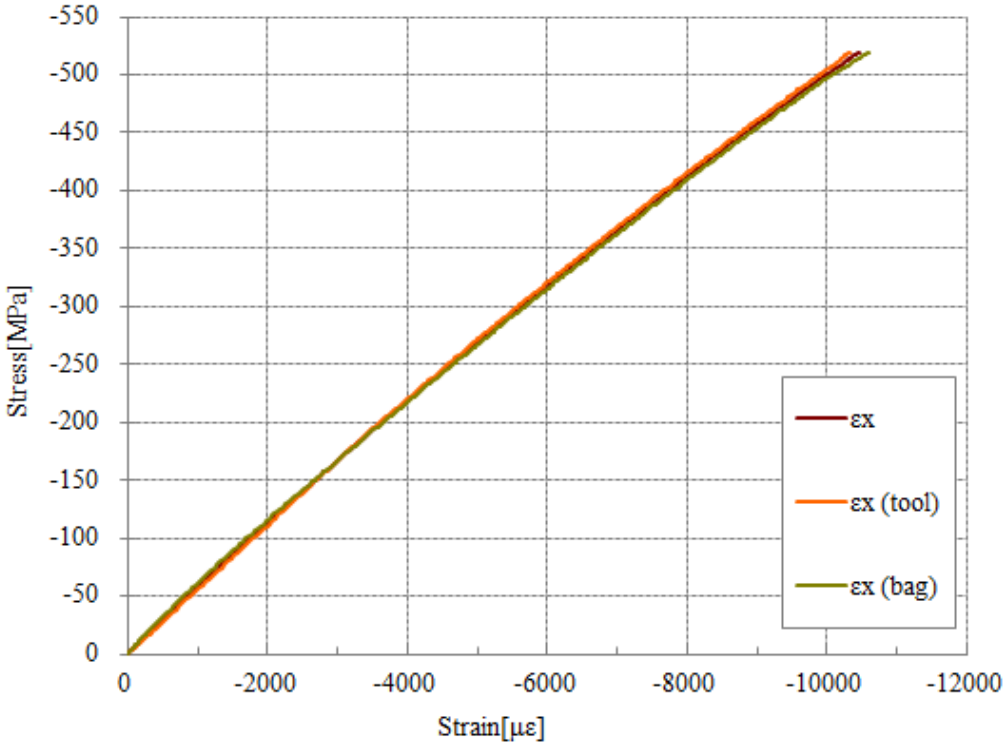

(a)

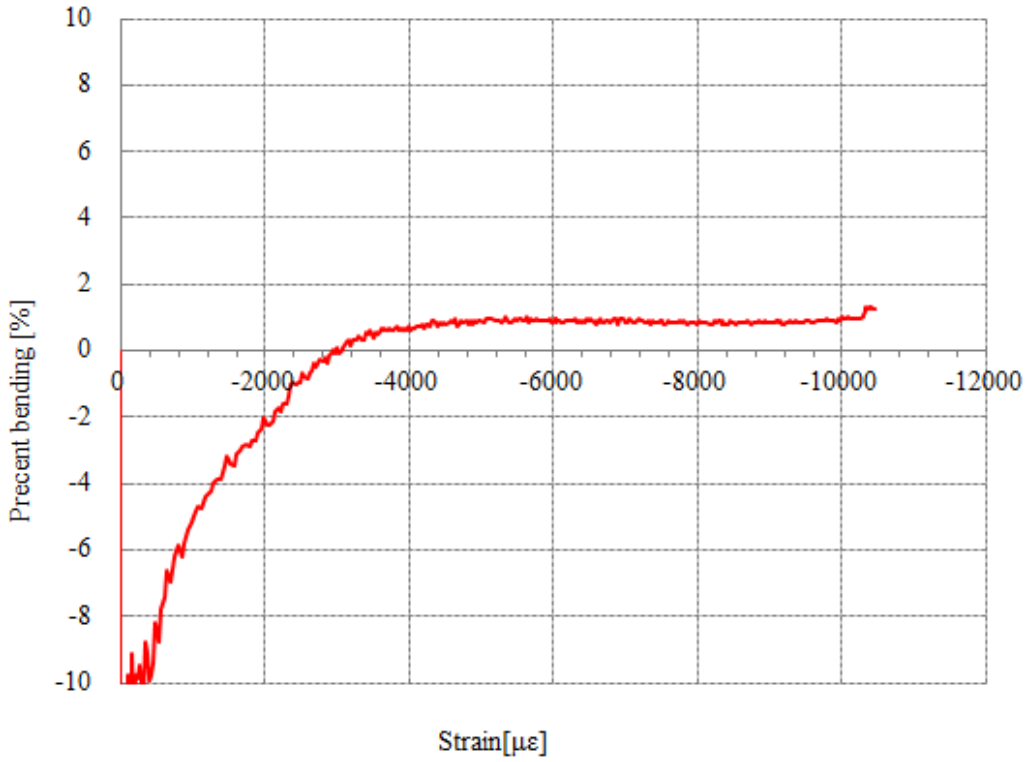

(b)

Fig. 5-12 Testing records of the specimen SP-5: (a) relationship of stress and strain and (b) percent bending

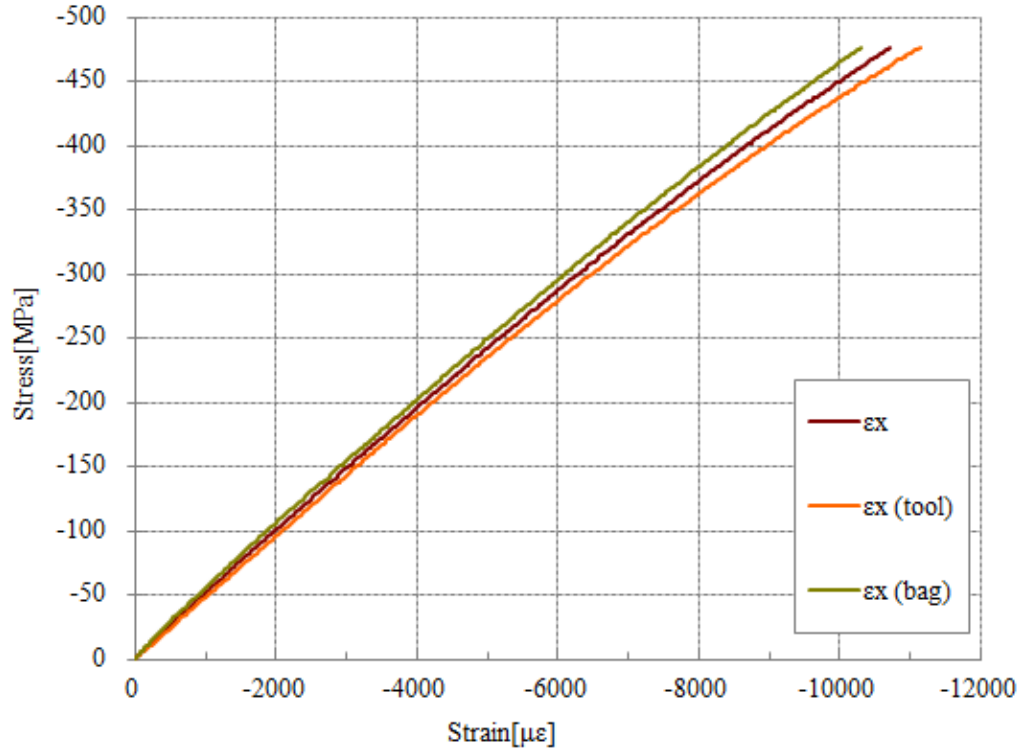

(a)

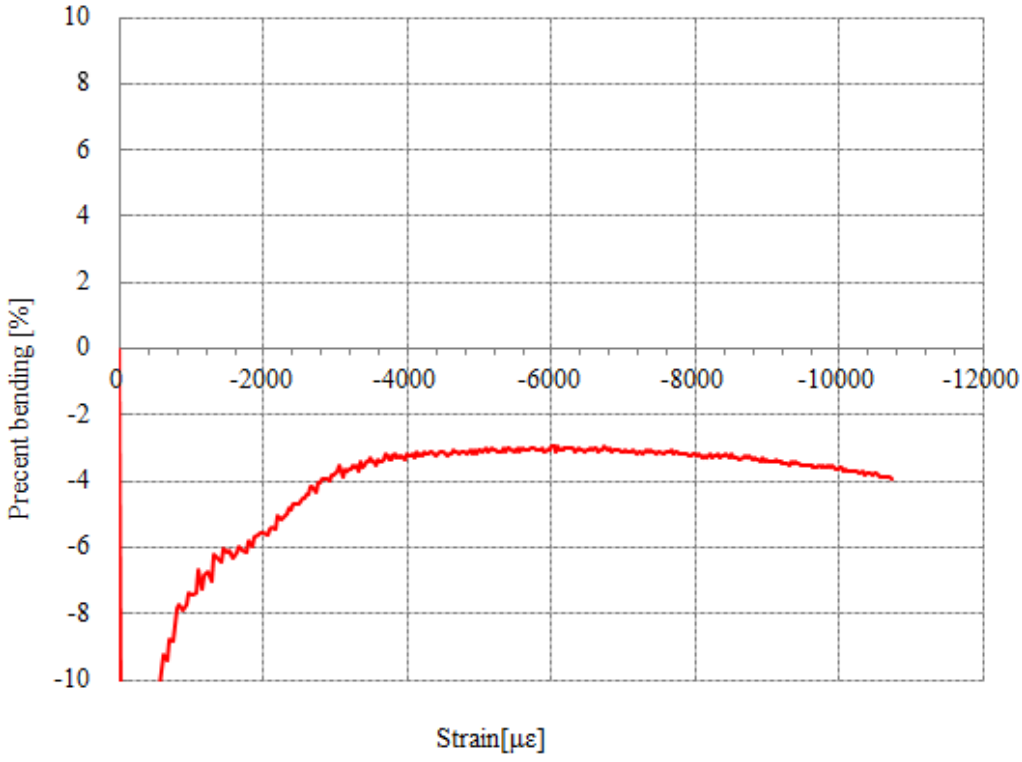

(b)

Fig. 5-13 Testing records of the specimen LP-1: (a) relationship of stress and strain and (b) percent bending

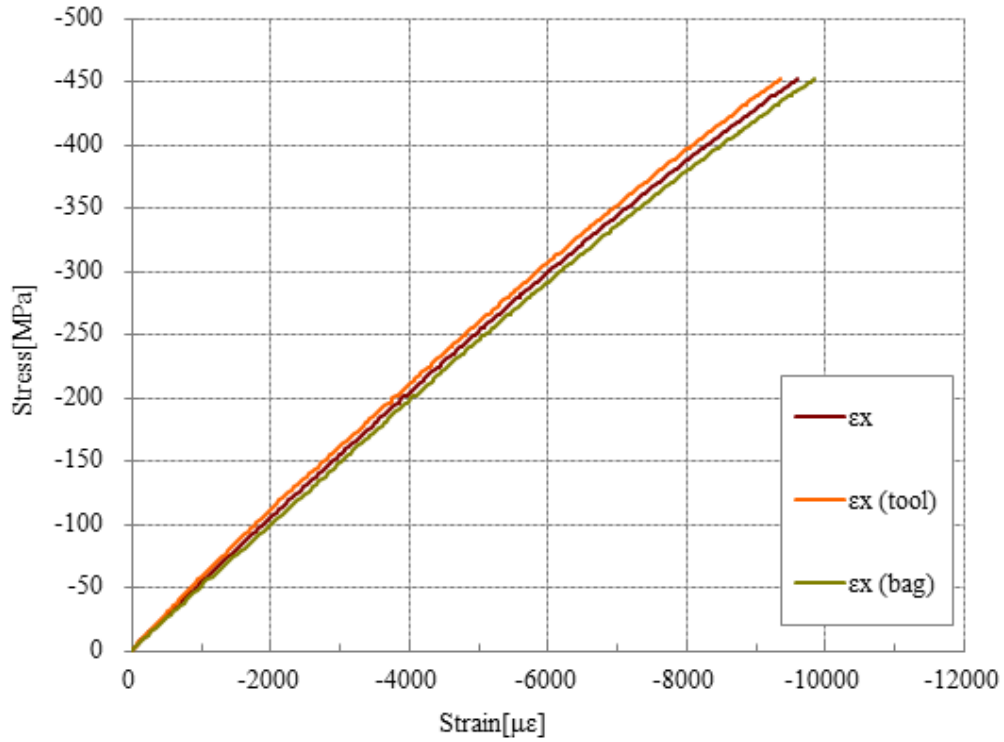

(a)

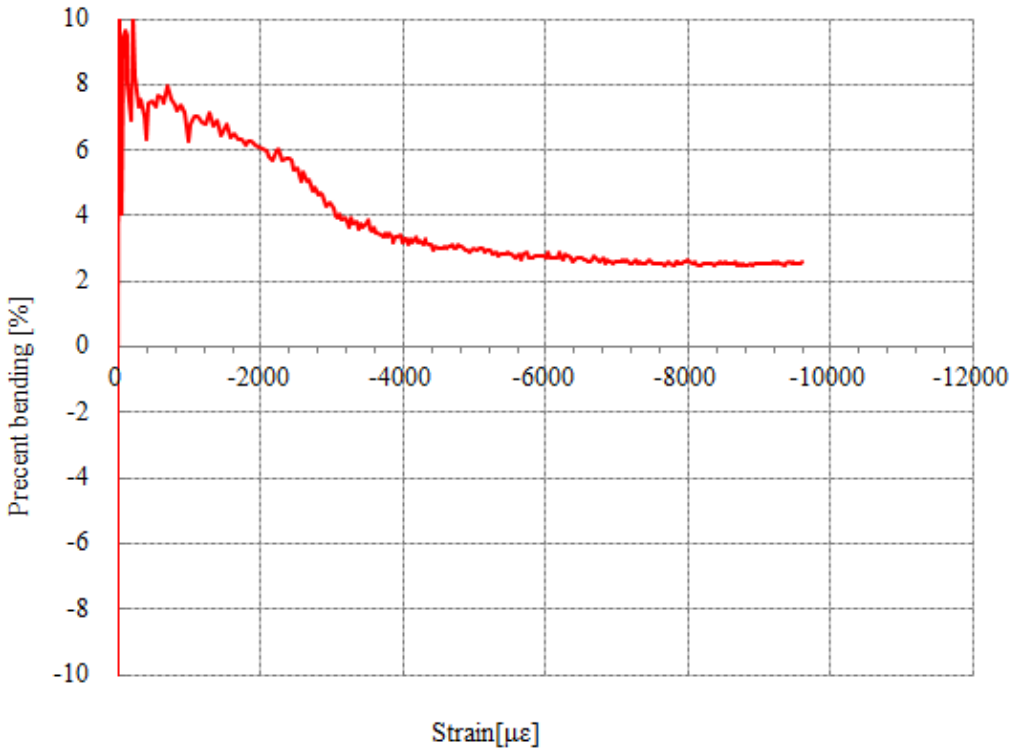

(b)

Fig. 5-14 Testing records of the specimen LP-2: (a) relationship of stress and strain and (b) percent bending

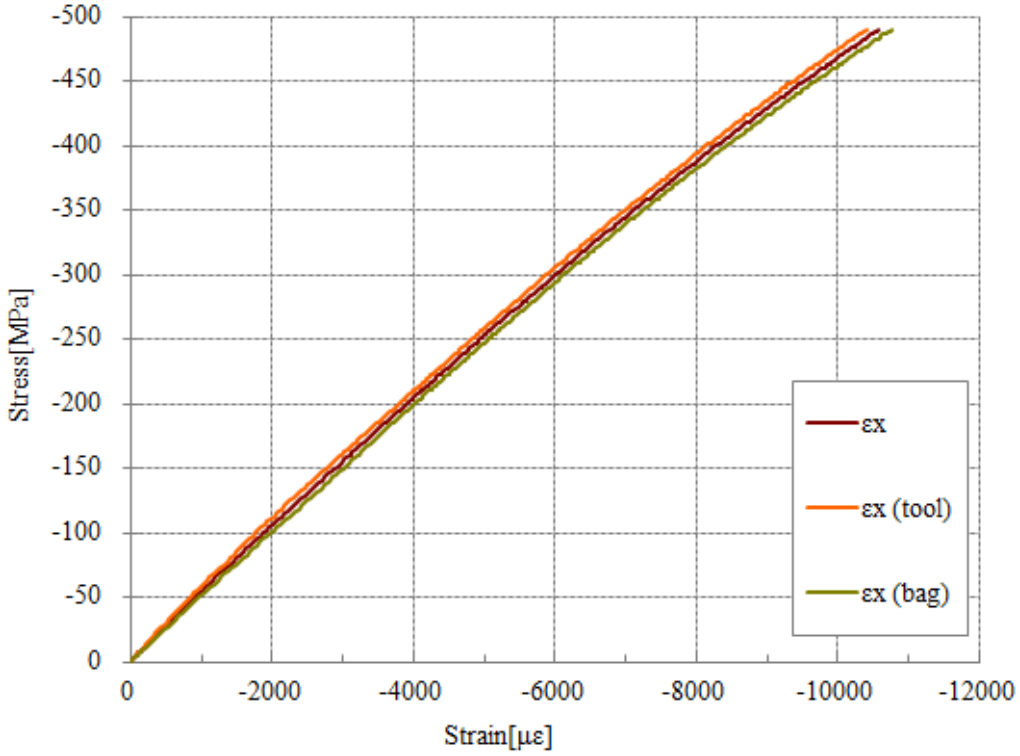

(a)

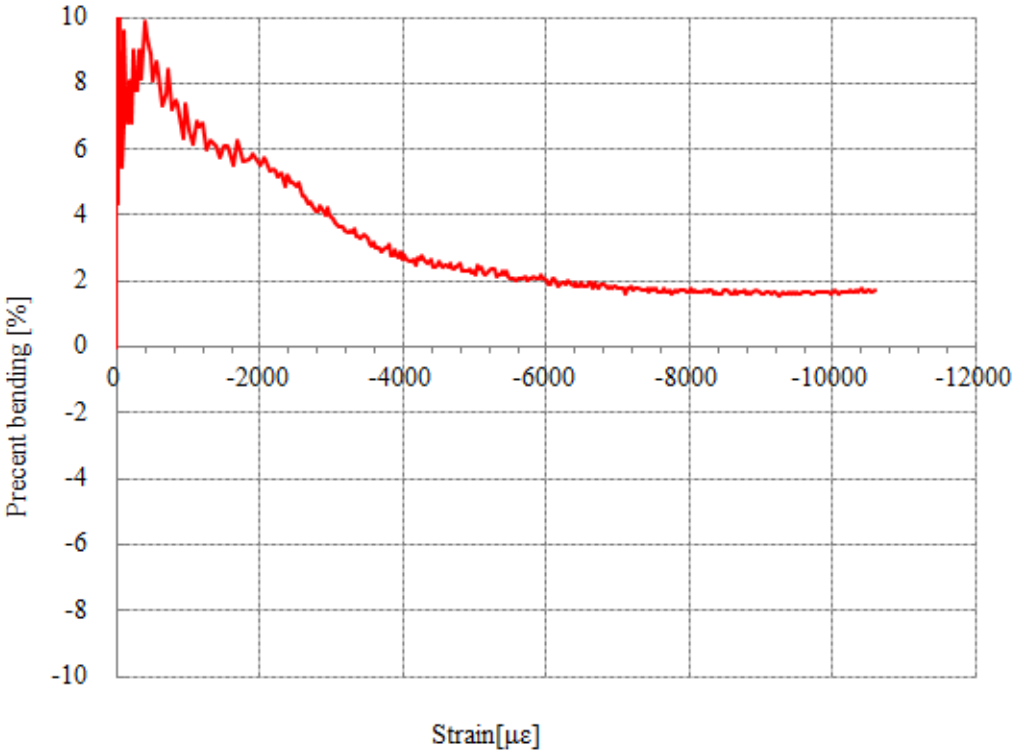

(b)

Fig. 5-15 Testing records of the specimen LP-3: (a) relationship of stress and strain and (b) percent bending

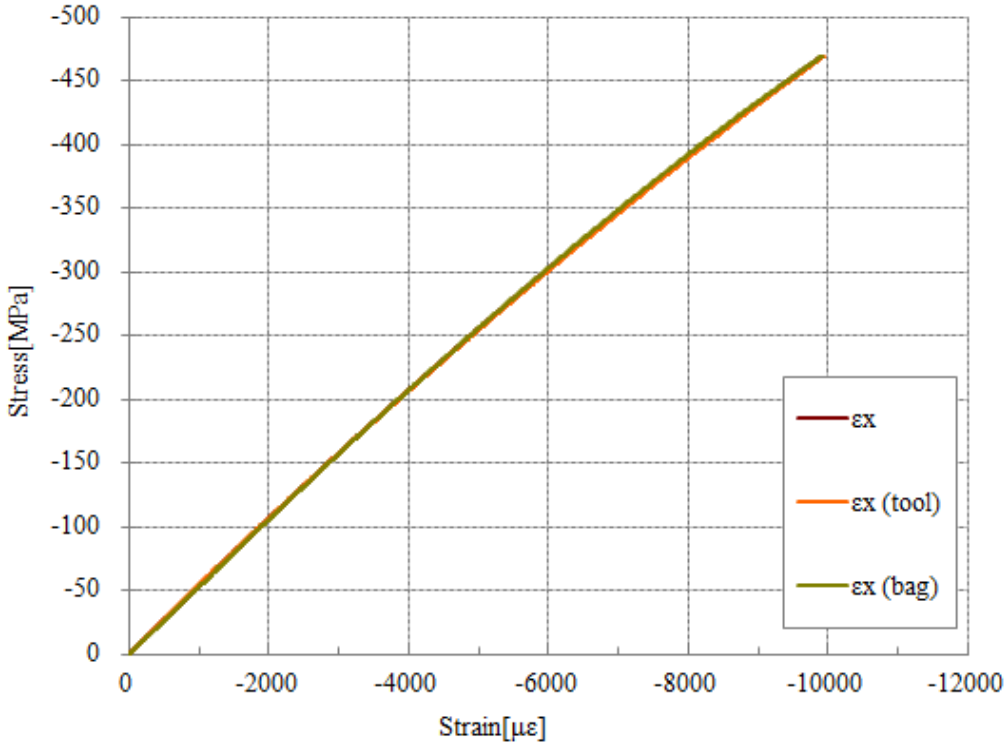

(a)

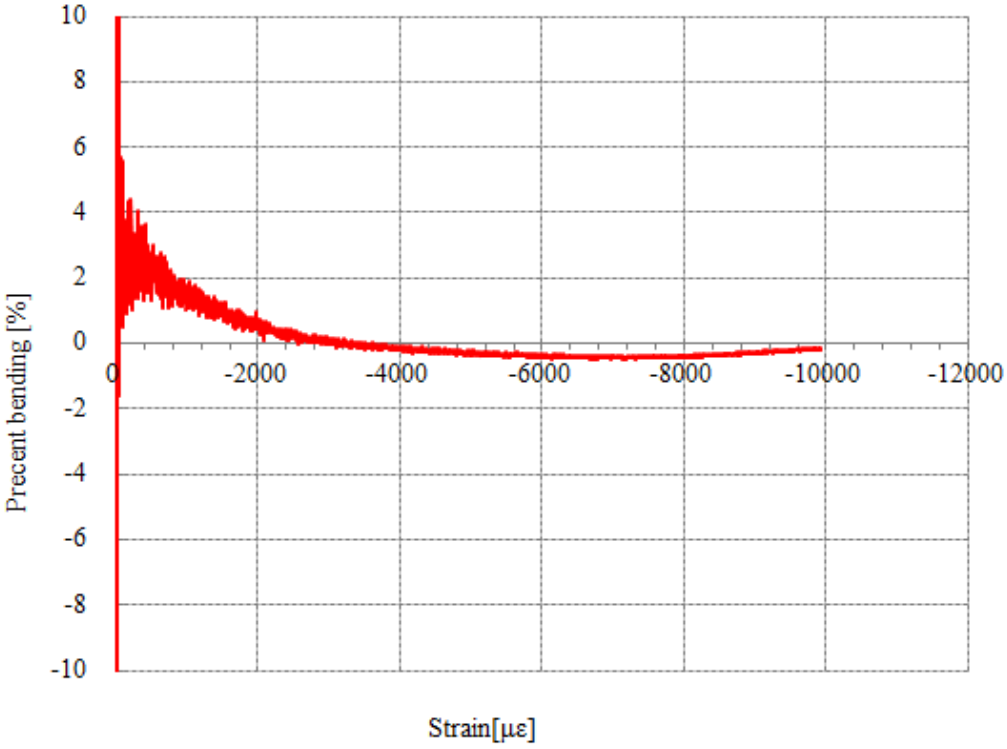

(b)

Fig. 5-16 Testing records of the specimen LP-4: (a) relationship of stress and strain and (b) percent bending

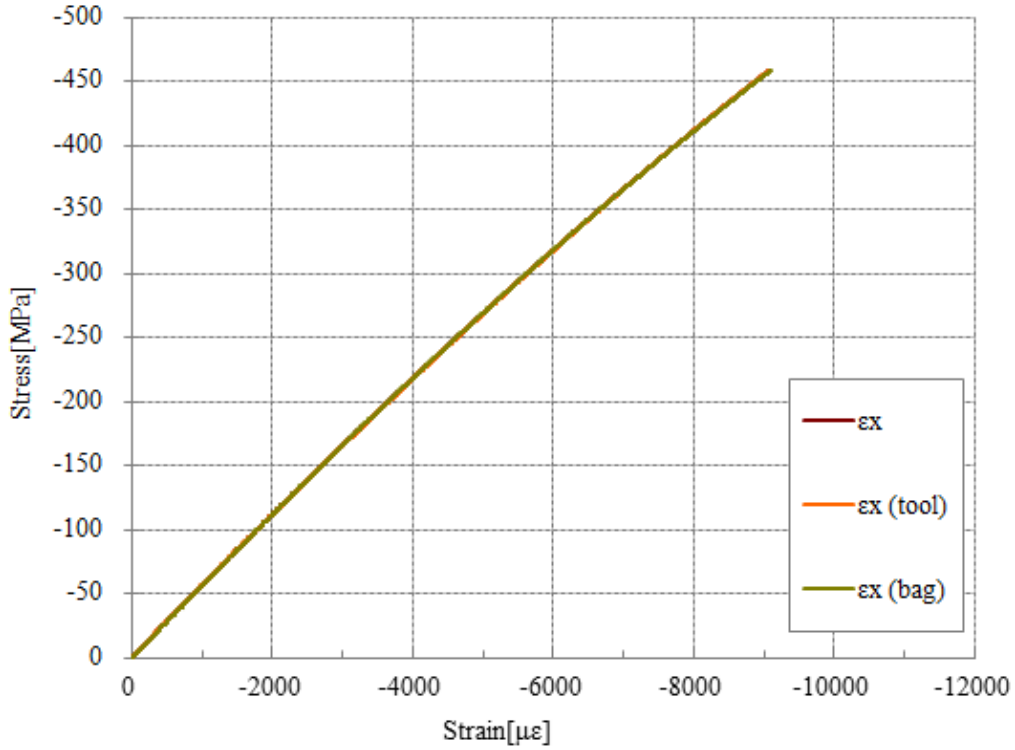

(a)

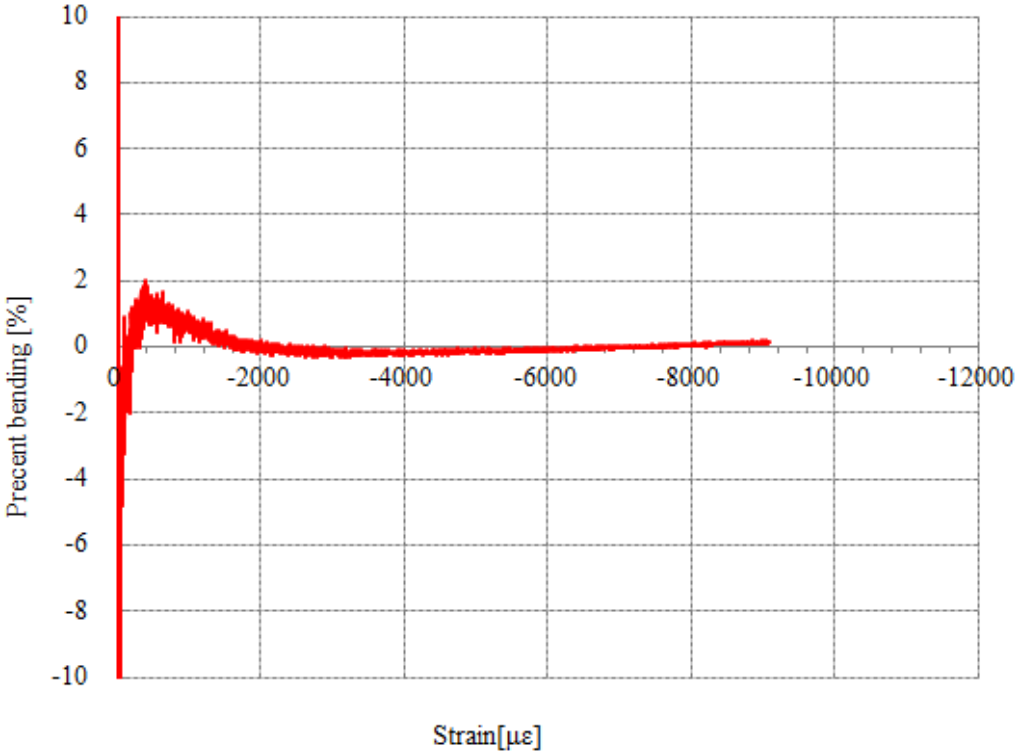

(b)

Fig. 5-17 Testing records of the specimen LP-5: (a) relationship of stress and strain and (b) percent bending

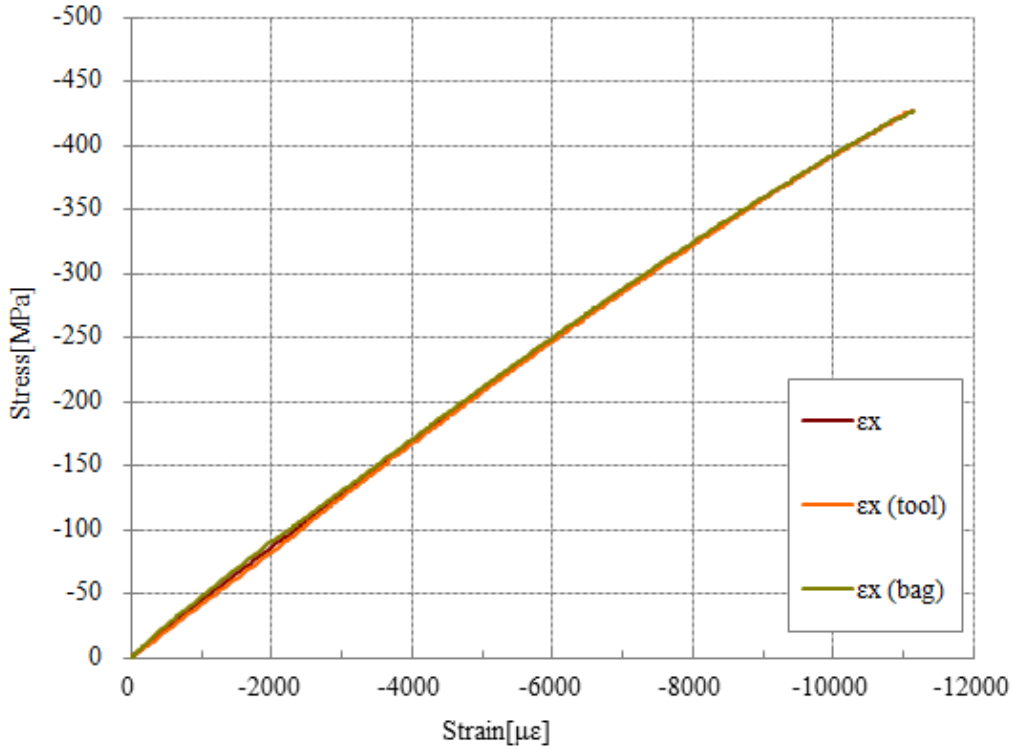

(a)

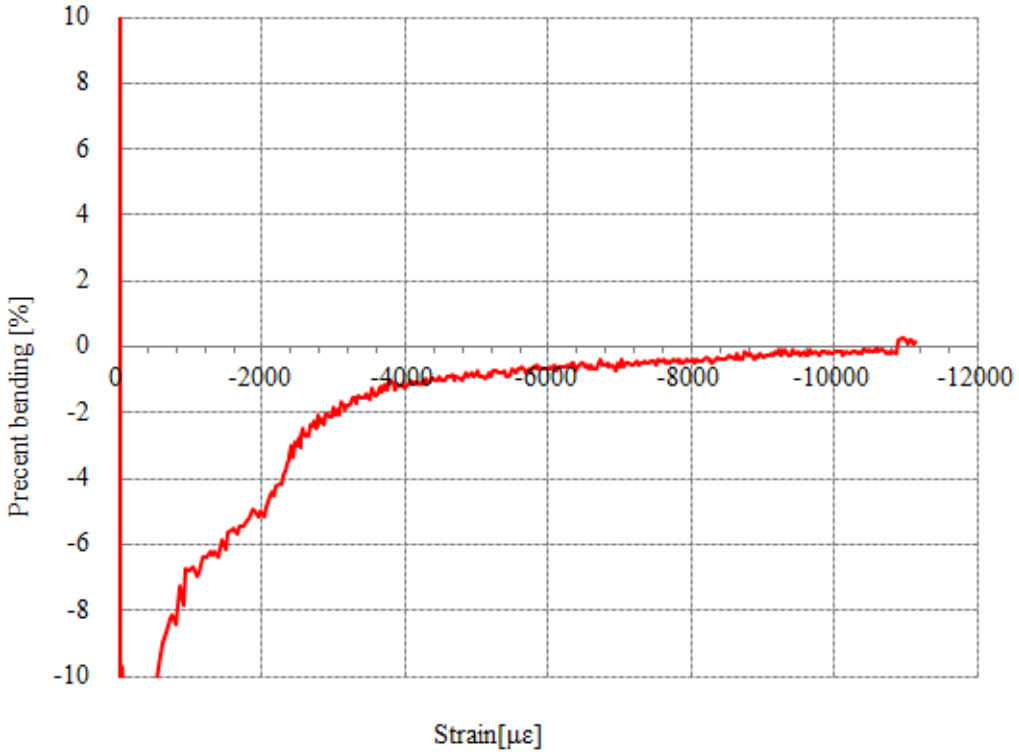

(b)

Fig. 5-18 Testing records of the specimen TP-1: (a) relationship of stress and strain and (b) percent bending

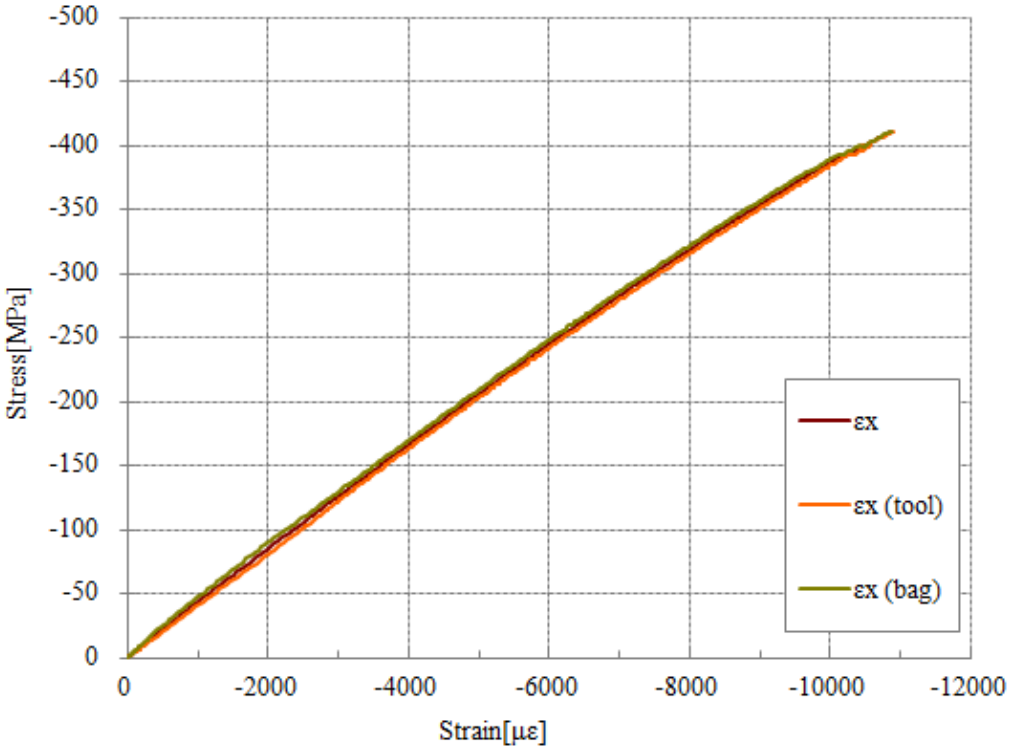

(a)

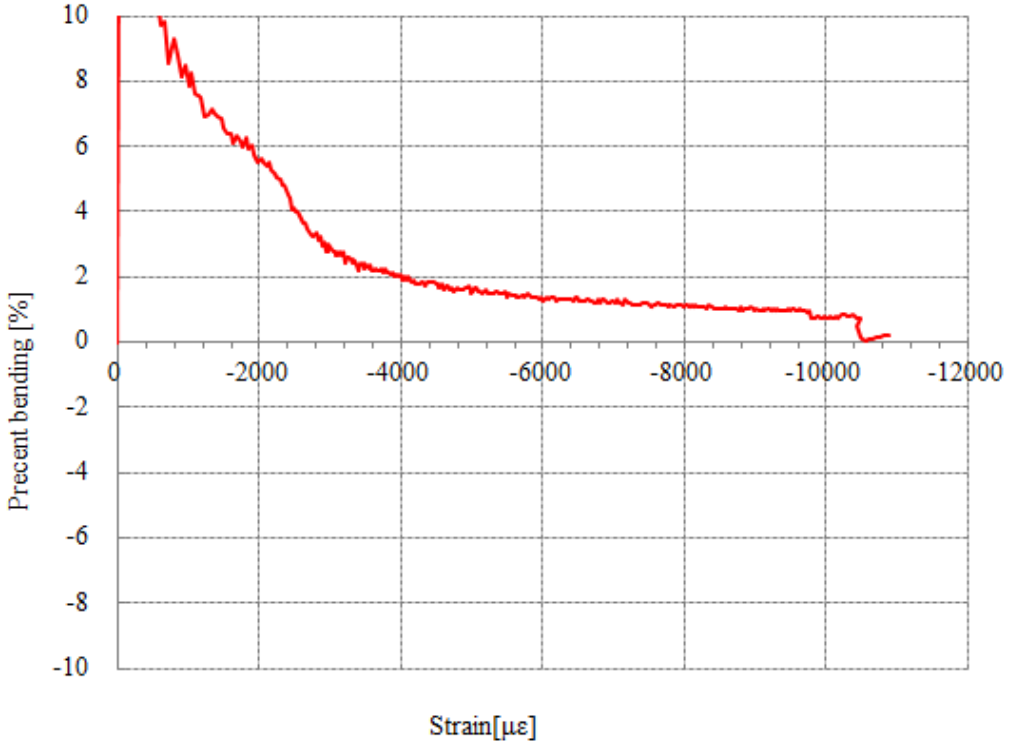

(b)

Fig. 5-19 Testing records of the specimen TP-2: (a) relationship of stress and strain and (b) percent bending

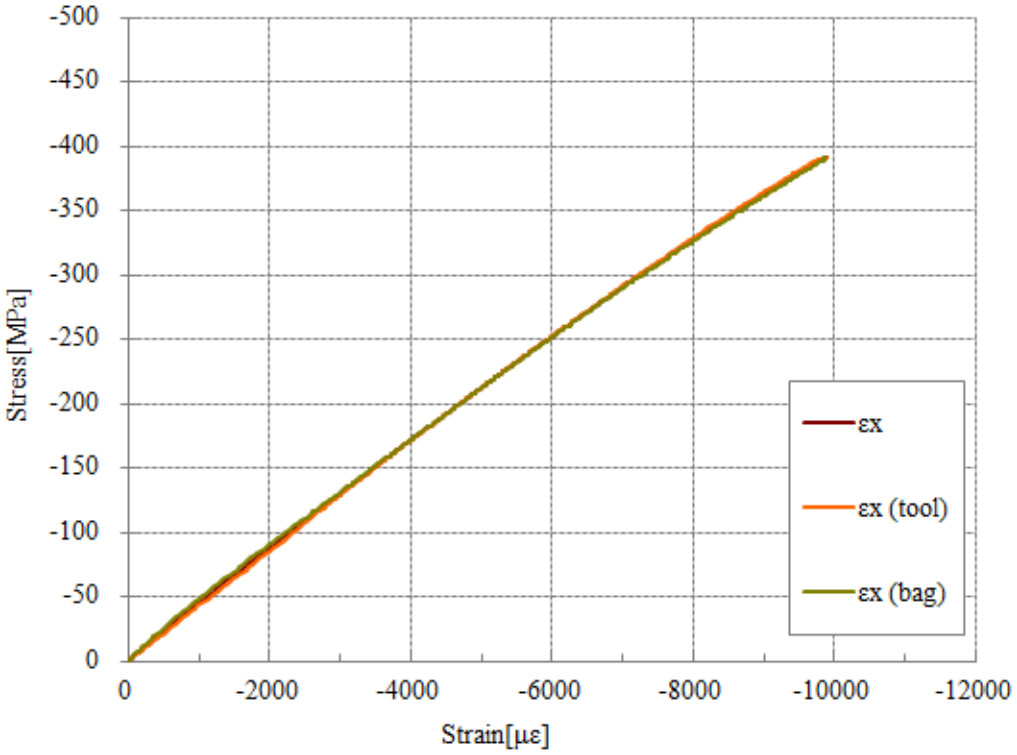

(a)

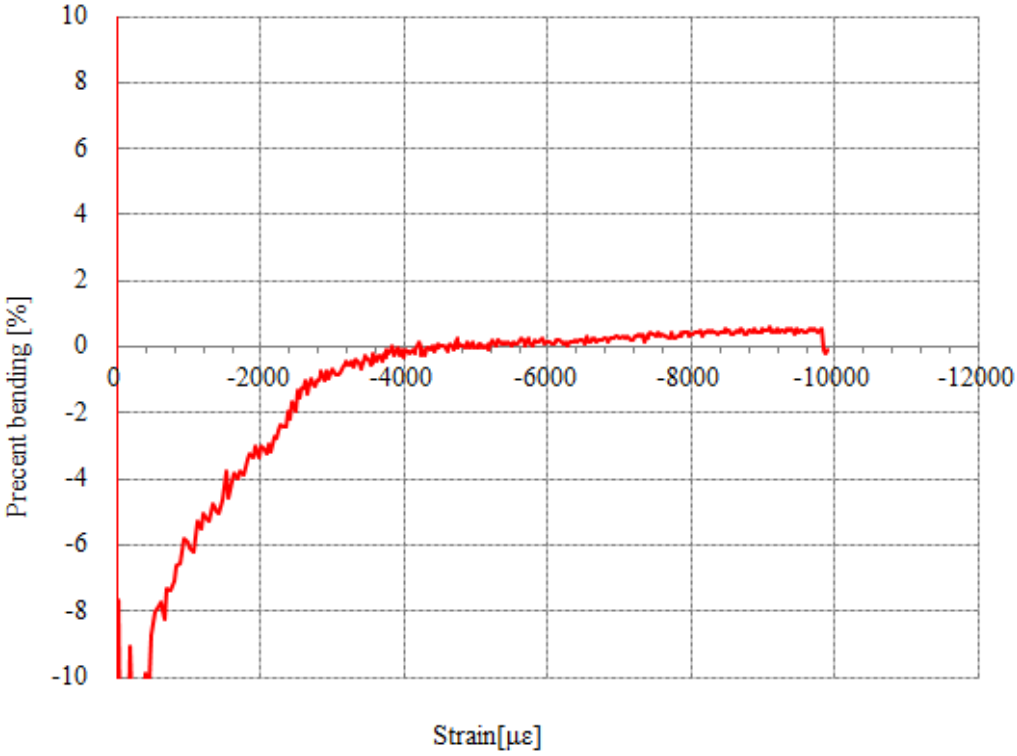

(b)

Fig. 5-20 Testing records of the specimen TP-3: (a) relationship of stress and strain and (b) percent bending

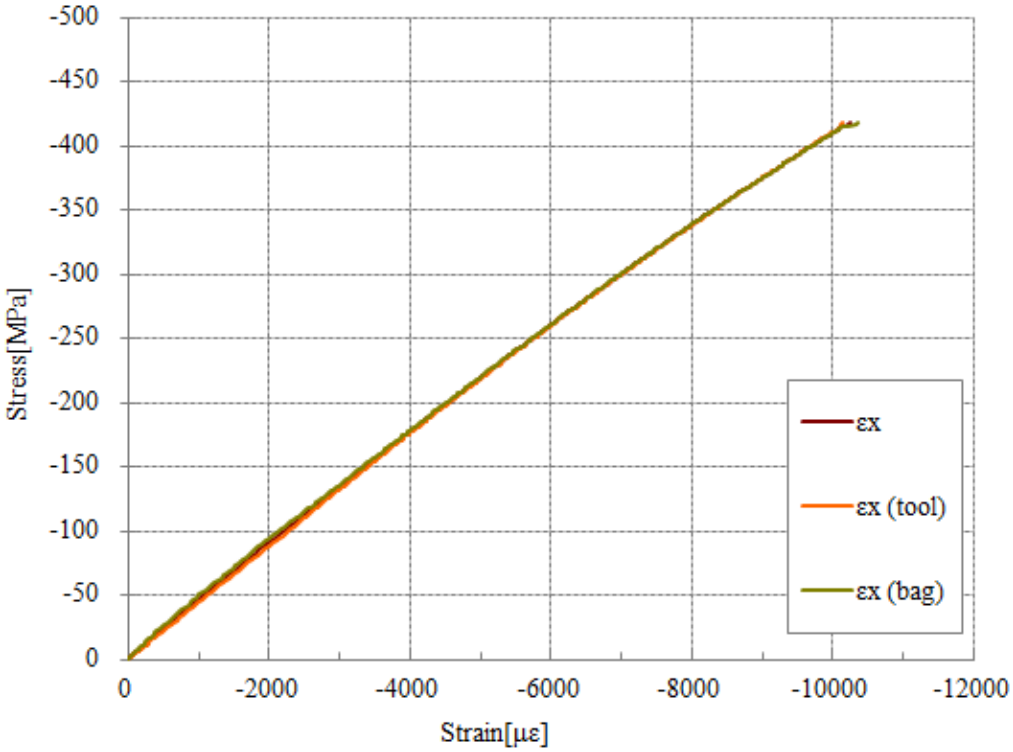

(a)

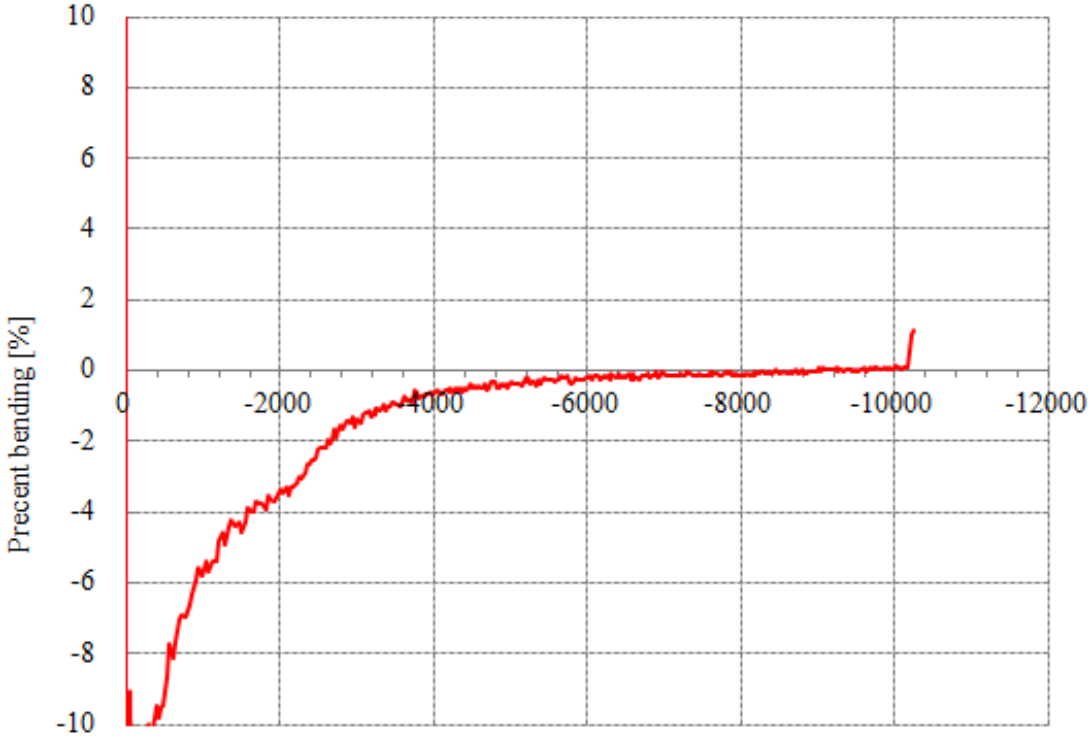

(b)

Fig. 5-21 Testing records of the specimen TP-4: (a) relationship of stress and strain and (b) percent bending

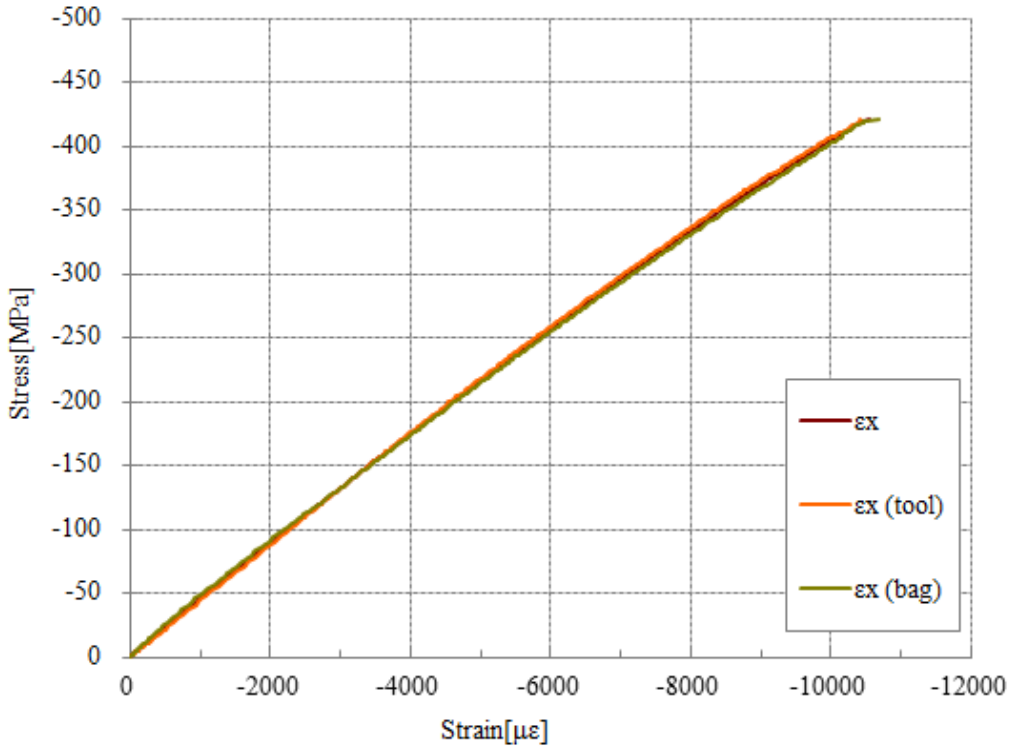

(a)

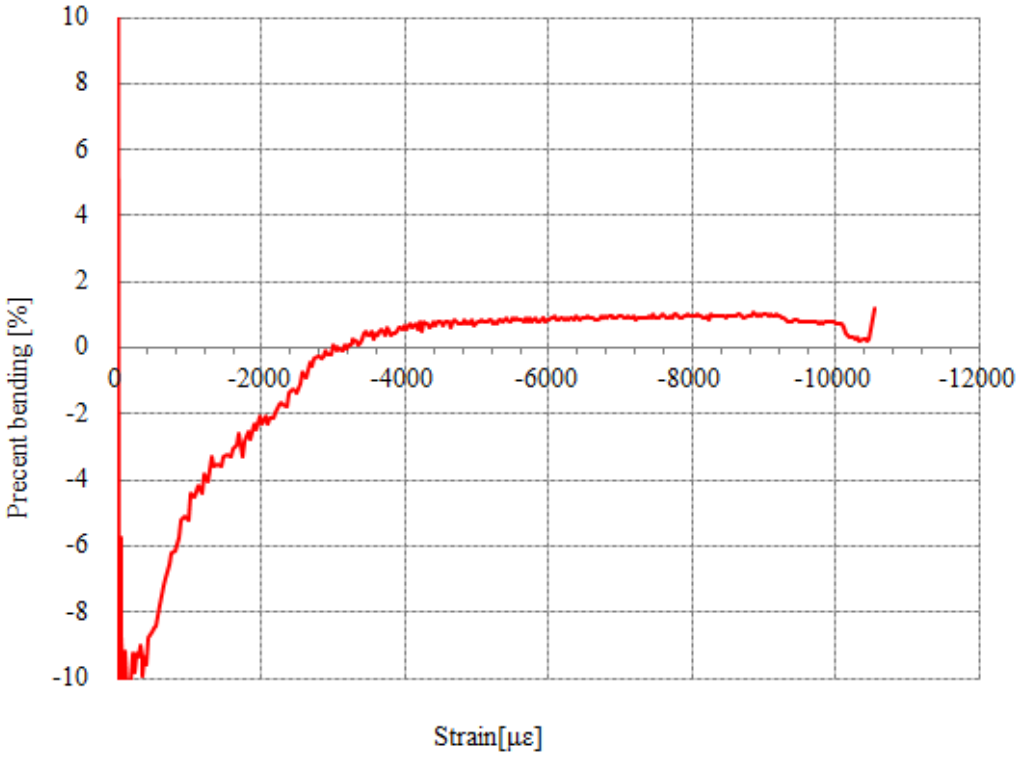

(b)

Fig. 5-22 Testing records of the specimen TP-5: (a) relationship of stress and strain and (b) percent bending

Chapter 6

Effect of out-of-plane fiber waviness on composite laminates

6.1 Introduction

The effect of out-of-plane fiber waviness on the compressive strength of composite laminates is investigated in this chapter. Two kinds of out-of-plane fiber waviness were formed in laminate SP and LP and measured using a fast Fourier transform method. The effect of out-of-plane fiber waviness on the compressive strength was identified using experimental, theoretical, and numerical methods. It was found that the compressive strength of a composite laminate fabricated using LP fabric is greater than that fabricated using SP fabrics. The relationship between the compressive strength and fiber waviness configuration was investigated in a parametrical study, and four compressive failure modes were found: the axial compressive, normal, bending, and shear failure modes.

6.2 Experimental results

The experimental compressive strength of SP and LP specimens are normalized to 60% fiber volume fraction because of the fiber volume fraction disparity among the different specimens [86], and these strength values are listed in Table 6-1. The average compressive strength of SP specimens is 464.8 MPa, and that of LP specimens is 487.9 MPa. This suggested that LP specimens, which are fabricated with LP fabric, had a greater compressive strength than that fabricated with SP fabric.

Table 6-1 Normalized compressive properties of SP and LP specimens

	Young's modulus E_{c60} [GPa]	Compressive strength F_{c60} [MPa]		Young's modulus E_{c60} [GPa]	Compressive strength F_{c60} [MPa]
SP-1	52.5	430.6	LP-1	52.2	515.3
SP-2	53.3	430.8	LP-2	51.3	459.9
SP-3	50.6	488.6	LP-3	51.3	499.6
SP-4	52.8	462.6	LP-4	55.1	497.9
SP-5	53.1	511.1	LP-5	55.5	466.5
SP-Average	52.5	464.8	LP-Average	53.1	487.9
S.D.	1.0	31.7	S.D.	1.9	21.1
C.V.	1.8%	6.8%	C.V.	3.5%	4.3%

Relationships of the compressive properties and the out-of-plane fiber waviness ratio are shown in Fig. 6-1. As the figure shows, the normalized compressive modulus,

E_{c60}, and the normalized compressive strength, F_{c60}, reduce with increasing the out-of-plane fiber waviness ratio. However, the reduction in the normalized compressive strength is more obvious than that in the normalized compressive modulus, which means indicates that the out-of-plane fiber waviness has a greater effect on the strength than on the modulus. Moreover, the experimental dispersity of the SP specimens is greater than the LP specimens because of the higher dispersity of the out-of-plane fiber waviness in SP specimens. However, the out-of-plane fiber waviness is only measured on the cross-sections of the SP specimens, and the measured out-of-plane fiber waviness may have the deviation with the internal out-of-plane fiber waviness in one specimen.

A typical post failure image was taken for each kind of specimens after the experiment; these images are shown in Fig. 6-2. Fig. 6-2(a) shows a kind of brooming failure mode for laminate SP [87]. Kelly and Hallstrom [88] demonstrated this failure mode, which was caused by laminate expansion, and an intralaminar and interlaminar fracture of the plies, which was promoted by the tensile through-thickness stress due to the expansion. In contrast, the post failure zone of laminate LP shown in Fig. 6-2(b) was slimmer than that of laminate SP. To explain the compressive strength and failure mechanism of laminates SP and LP, a theoretical analysis is discussed in the next section.

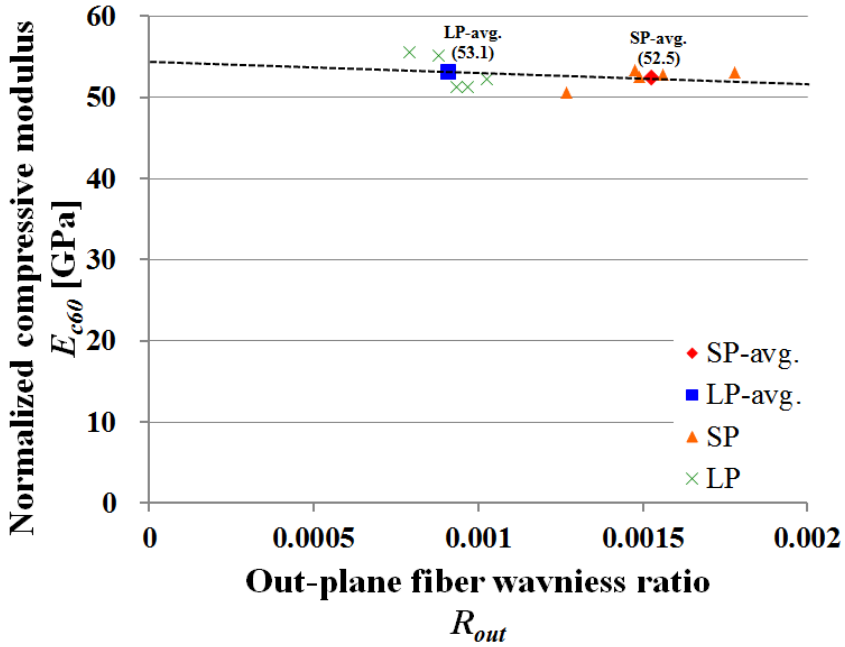

(a)

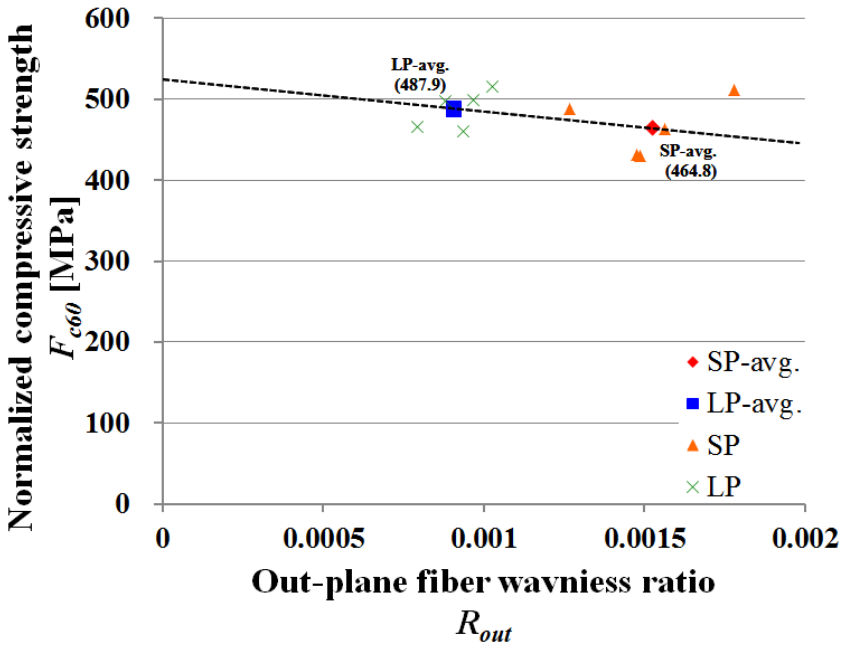

(b)

Fig. 6-1 Normalized compressive properties vs. out-of-plane fiber waviness ratio:

(a) normalized compressive modulus and (b) normalized compressive strength.

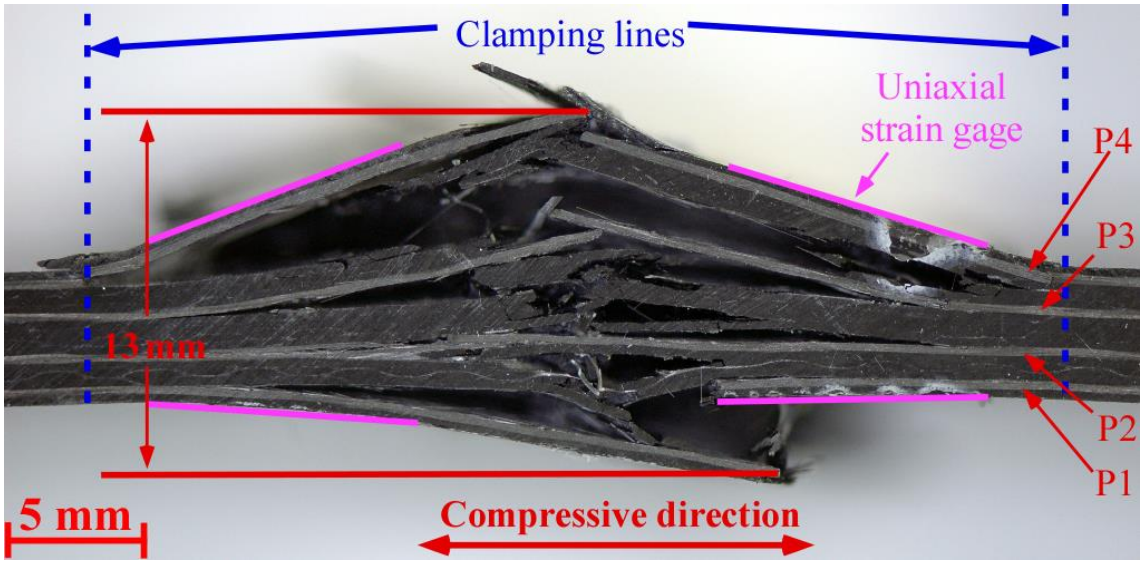

(a)

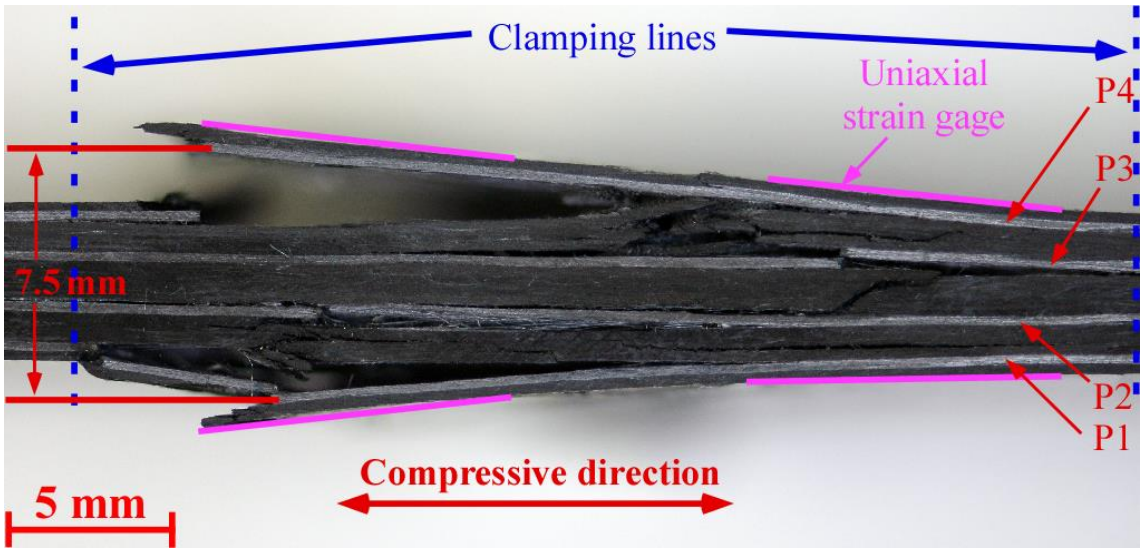

(b)

Fig. 6-2 Images of typical post failure mode: (a) laminate SP and (b) laminate LP.

6.3 Theoretical analysis

In the classical lamination theory (CLT), the out-of-plane stress components are ignored. However, considering the laminate expansion in the thickness direction, we deduced the tensile through-thickness stress according to the CLT. In one wavelength, the fiber waviness is assumed to have a small curvature in the laminate, and the deflection equation for the middle surface $W(x)$ in the x-z plane is shown as Eq. (6-1), where the x direction is the length direction of the laminate, and z is the thickness direction.

$$W(x) = A[1 - \cos(2\pi x / L)] \tag{6-1}$$

where A is the amplitude and L is equal to the wavelength.

The radius of curvature $R(x)$ is written as Eq. (6-2).

$$R(x) = \frac{[1 + (dW/dx)^2]^{3/2}}{|d^2W/dx^2|} \tag{6-2}$$

Because the minimal $R(x)$ for laminate SP is approximately 110 mm and that for laminate LP is 385 mm, the laminate with out-of-plane fiber waviness could first be considered to be straight for the calculation of the compressive stress in the case of a small curvature, $2R(x)/h>10$, where h is the thickness of the laminate [89].

When this symmetrical laminate is subjected to a force per unit width of cross section N_s, where the subscript s means the tangent line of the curved laminate in the x-z

plane, we assume that the strain of the middle surface $\varepsilon^0{}_s$ is known and calculate $\varepsilon^0{}_y$, $\varepsilon^0{}_{sy}$, and N_s using Eqs. (6-3) to (6-6).

$$\begin{bmatrix} N_s \\ 0 \\ 0 \end{bmatrix} = \begin{bmatrix} A_{11} & A_{12} & 0 \\ A_{12} & A_{22} & 0 \\ 0 & 0 & A_{66} \end{bmatrix} \begin{bmatrix} \varepsilon_s^0 \\ \varepsilon_y^0 \\ \varepsilon_{sy}^0 \end{bmatrix} \tag{6-3}$$

$$\varepsilon_y^0 = -\frac{A_{12}}{A_{22}} \varepsilon_s^0 \tag{6-4}$$

$$\varepsilon_{sy}^0 = 0 \tag{6-5}$$

$$N_s = (A_{11} - \frac{A_{12}^2}{A_{22}}) \varepsilon_s^0 \tag{6-6}$$

To compensate for the effect of the small curvature on the compressive stress, a moment per unit width M_s caused by the deflection of the middle surface under compression in the *x*-*z* plane is added, which can be written as

$$M_s(x) = -N_s W(x) \tag{6-7}$$

and the middle surface curvatures κ_s, κ_y, and κ_{sy} are calculated using Eqs. (6-8) to (6-11).

$$\begin{bmatrix} M_s \\ 0 \\ 0 \end{bmatrix} = \begin{bmatrix} D_{11} & D_{12} & D_{16} \\ D_{12} & D_{22} & D_{26} \\ D_{16} & D_{26} & D_{66} \end{bmatrix} \begin{bmatrix} \kappa_s \\ \kappa_y \\ \kappa_{sy} \end{bmatrix} \tag{6-8}$$

$$\kappa_y = \frac{(D_{12}D_{66} - D_{16}D_{26})}{(D_{26}^2 - D_{22}D_{66})} \kappa_s \tag{6-9}$$

$$\kappa_{sy} = \frac{(D_{16}D_{22} - D_{12}D_{26})}{(D_{26}^2 - D_{22}D_{66})} \kappa_s \tag{6-10}$$

$$\kappa_s = -\frac{(A_{11} - \frac{A_{12}^2}{A_{22}})}{[D_{11} + D_{12}\frac{(D_{12}D_{66} - D_{16}D_{26})}{(D_{26}^2 - D_{22}D_{66})} + D_{16}\frac{(D_{16}D_{22} - D_{12}D_{26})}{(D_{26}^2 - D_{22}D_{66})}]}\varepsilon_s^0 W(x) \quad (6\text{-}11)$$

Therefore, the in-plane stresses in the k^{th} layer can be expressed as

$$\begin{bmatrix}\sigma_s \\ \sigma_y \\ \tau_{sy}\end{bmatrix}_k = \begin{bmatrix}\overline{Q}_{11} & \overline{Q}_{12} & \overline{Q}_{16} \\ \overline{Q}_{12} & \overline{Q}_{22} & \overline{Q}_{26} \\ \overline{Q}_{16} & \overline{Q}_{26} & \overline{Q}_{66}\end{bmatrix}_k \left[\begin{bmatrix}\varepsilon_s^0 \\ \varepsilon_y^0 \\ \varepsilon_{sy}^0\end{bmatrix} + z_k\begin{bmatrix}\kappa_s \\ \kappa_y \\ \kappa_{sy}\end{bmatrix}\right] \quad (6\text{-}12)$$

The laminate is divided into infinitesimally thin slices $d\alpha$ in the length direction. A side view of the sublaminate is shown in Fig. 6-3. This sublaminate contains *m* layers counting from the bottom surface. The *s* and *n* directions are the tangent and normal line of the sublaminate in the *x*-*z* plane, respectively.

The normal force per unit width *F* and shear force per unit width *Q* on the *m*-layer-sublaminate are calculated using Eqs. (6-13) to (6-15).

$$F = \sum_{i=1}^{m}\sigma_{si}t \quad (i=1,2,3\ldots.m) \quad (6\text{-}13)$$

$$\frac{\partial\sigma_{si}}{\partial x} + \frac{\partial\tau_{si}}{\partial z} = 0 \quad (i=1,2,3\ldots.m) \quad (6\text{-}14)$$

$$Q = \int_{\frac{-h}{2}}^{z}\tau_s dz = \sum_{i=1}^{m}\tau_{si}t \approx \sum_{i=1}^{m}(\sum_{j=1}^{i} - \frac{\partial\sigma_{sj}t}{\partial x})t \quad (6\text{-}15)$$

where σ_{si} and σ_{si} are the σ_s values in the *i*th and *j*th layer, respectively; τ_{si} is the interlaminar shear stress at the upper interlayer of the *i*th layer; and *b* is the width and *t* is the thickness of each layer.

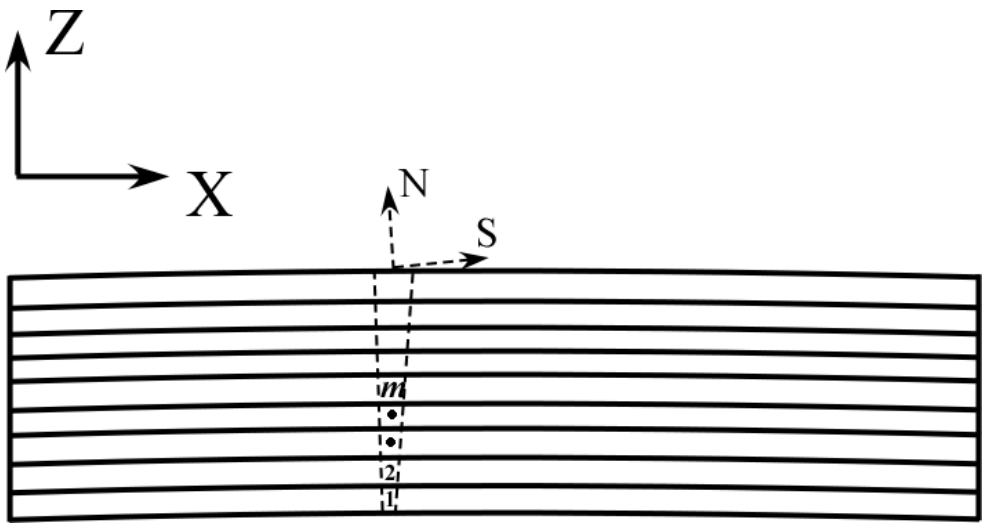

(a)

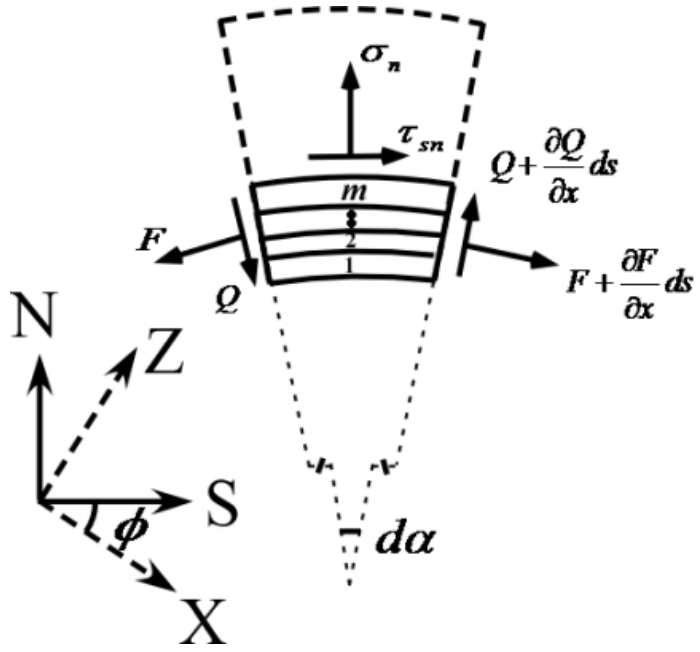

(b)

Fig. 6-3. Illustrations of sublaminate containing *m* layers:

(a) thin slice of laminate and (b) partial free-body diagram of sublaminate.

Because the sublaminate is in force equilibrium in Fig. 6-3(b), we sum the forces in the *s* direction and obtain

$$\tau_{sn} ds + (F + \frac{\partial F}{\partial x} ds) \cos \frac{d\alpha}{2} - F \cos \frac{d\alpha}{2} + (Q + \frac{\partial Q}{\partial x} ds) \sin \frac{d\alpha}{2} + Q \sin \frac{d\alpha}{2} = 0 \tag{6-16}$$

We can neglect the higher-order differentials in Eq. (6-16), and thus

$$\tau_{sn} ds + \frac{\partial F}{\partial x} ds + Q d\alpha = 0 \tag{6-17}$$

where $ds = R(x) d\alpha$, and

$$\tau_{sn} = -\frac{\partial F}{\partial x} - \frac{Q}{R(x)} \tag{6-18}$$

Similarly, in the *n* direction

$$\sigma_n ds - (F + \frac{\partial F}{\partial x} ds) \sin \frac{d\alpha}{2} - F \sin \frac{d\alpha}{2} + (Q + \frac{\partial Q}{\partial x} ds) \cos \frac{d\alpha}{2} - Q \cos \frac{d\alpha}{2} = 0 \tag{6-19}$$

$$\sigma_n ds - F d\alpha + \frac{\partial Q}{\partial x} ds = 0 \tag{6-20}$$

$$\sigma_n = \frac{F}{R(x)} - \frac{\partial Q}{\partial x} \tag{6-21}$$

Therefore, the values of σ_s, τ_{sn}, and σ_n for the *n*-th layer in the *s*-*n* coordinate system are calculated using Eqs. (6-12), (6-18), and (6-21), respectively.

Considering a rotation ϕ from the *x*-*z* coordinate system to the *s*-*n* coordinate system in Fig. 6-3(b), the transformed stresses are given by

$$\phi = \arctan(\frac{dW}{dx}) \tag{6-22}$$

$$\sigma_x = \sigma_s \sin^2\phi + \sigma_n \cos^2\phi - 2\tau_{sn} \sin\phi\cos\phi \qquad (6\text{-}23)$$

$$\sigma_z = \sigma_s \sin^2\phi + \sigma_n \cos^2\phi + 2\tau_{sn} \sin\phi\cos\phi \qquad (6\text{-}24)$$

$$\tau_{xz} = -\sigma_s \sin\phi\cos\phi + \sigma_n \sin\phi\cos\phi + \tau_{sn}(\cos^2\phi - \sin^2\phi) \qquad (6\text{-}25)$$

Afterward, the stress components are translated from the *x-y-z* coordinate system to the 1-2-3 material coordinate system in Eq. (6-26) [90].

$$\begin{bmatrix} \sigma_{11} \\ \sigma_{22} \\ \sigma_{33} \\ \sigma_{23} \\ \sigma_{13} \\ \sigma_{12} \end{bmatrix}_k = T_{\sigma k} \begin{bmatrix} \sigma_x \\ \sigma_y \\ \sigma_z \\ \sigma_{yz} \\ \sigma_{xz} \\ \sigma_{xy} \end{bmatrix}_k = \begin{bmatrix} m^2 & n^2 & 0 & 0 & 0 & 2mn \\ n^2 & m^2 & 0 & 0 & 0 & -2mn \\ 0 & 0 & 1 & 0 & 0 & 0 \\ 0 & 0 & 0 & m & -n & 0 \\ 0 & 0 & 0 & n & m & 0 \\ -mn & mn & 0 & 0 & 0 & (m^2 - n^2) \end{bmatrix}_k \begin{bmatrix} \sigma_x \\ \sigma_y \\ \sigma_z \\ \sigma_{yz} \\ \sigma_{xz} \\ \sigma_{xy} \end{bmatrix}_k \qquad (6\text{-}26)$$

where $m = \cos\theta$, $n = \sin\theta$, and T_σ is the transformation matrix of the stress.

Finally, we can use the factor F_{tw} in the Tsai–Wu failure criterion to determine the initial failure zone in the laminate, as shown in Eq. (6-27) [91], where we assume that the strengths of the composite in the *z* direction are the same as those in the *y* direction. In addition, the values of C_{12}, C_{23}, and C_{13} are simply set equal to zero, based on the results of Narayanaswami and Adelman [92].

$$C_1 = \frac{\sigma_{11}^2}{X_t X_c} + \frac{\sigma_{22}^2}{Y_t Y_c} + \frac{\sigma_{33}^2}{Z_t Z_c} + \frac{\sigma_{12}^2}{S^2} + \frac{\sigma_{13}^2}{S^2} + \frac{C_{12}\sigma_{11}\sigma_{22}}{(X_t X_c Y_t Y_c)^{1/2}} + \frac{C_{23}\sigma_{22}\sigma_{33}}{(Y_t Y_c Z_t Z_c)^{1/2}} + \frac{C_{13}\sigma_{33}\sigma_{11}}{(Z_t Z_c X_t X_c)^{1/2}}$$

$$C_2 = (\frac{1}{X_t} - \frac{1}{X_c})\sigma_{11} + (\frac{1}{Y_t} - \frac{1}{Y_c})\sigma_{22} + (\frac{1}{Z_t} - \frac{1}{Z_c})\sigma_{33}$$

$$F_{tw} = C_1 + C_2$$

(6-27)

This theoretical analysis was programmed in the Wolfram Mathematica software, and all the parameters needed for the calculation were in accordance with the values listed in Table 6-2. Two examples corresponding to laminates SP and LP are calculated. The distributions of F_{tw} in the length direction in the first two failure layers P1 and P2 shown in Fig. 6-2 are plotted in Fig. 6-4, where the maximal F_{tw} is equal to one.

Table 6-2. Properties of this unidirectional carbon/ epoxy composite

Properties	Value	Properties	Value
Longitudinal modulus, E_{11}	160 GPa	Longitudinal tensile strength, X_t	2500 MPa
Transverse modulus, E_{22}	10 GPa	Longitudinal compressive strength, X_c	1300 MPa
Tangential modulus, G_{12}	5 GPa	Transverse tensile strength, Y_t	50 MPa
Major Poisson's ratio, υ_{12}	0.32	Transverse compressive strength, Y_c	150 MPa
Ply thickness, t	0.3 mm	Shear strength, S	100 MPa

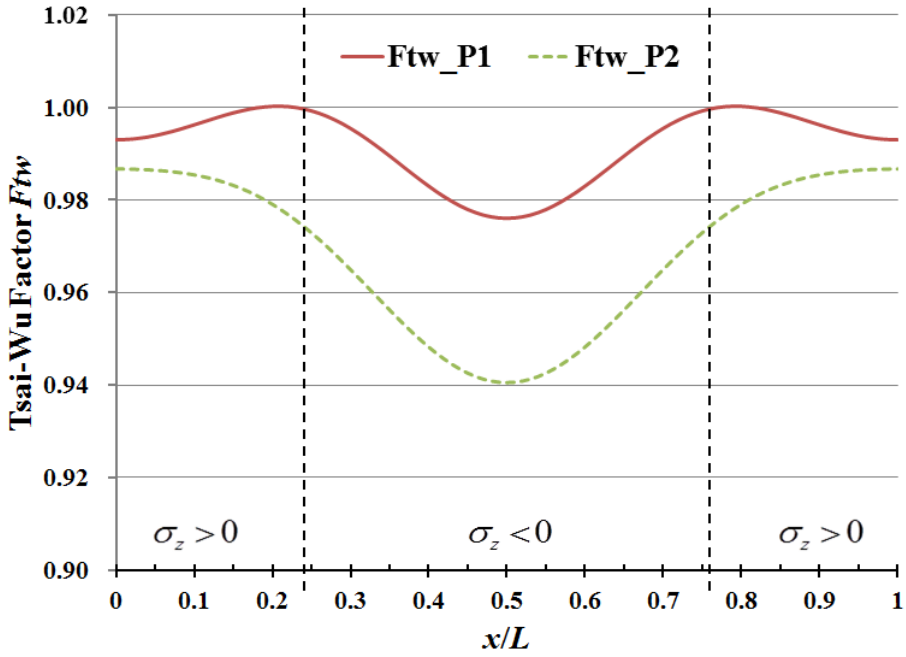

(a)

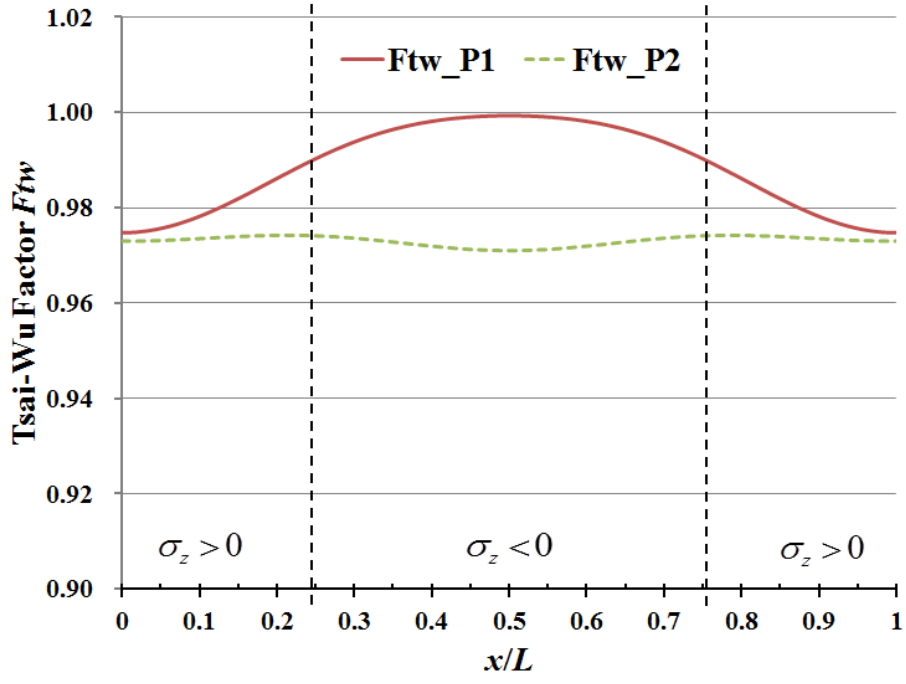

(b)

Fig. 6-4. Distribution of factor F_{tw} in length direction: (a) laminate SP and (b) laminate LP.

In Fig. 6-4(a), which corresponds to laminate SP, the dotted lines are boundaries between the tensile and compressive through-thickness stresses, which have values of 0.24 and 0.76 for x/L, respectively. The maximums of F_{tw} occur at x/L values equal to 0.21 and 0.79, which are in the zone of the tensile through-thickness stress. However, the maximal F_{tw} of laminate LP appears in the compressive through-thickness stress zone ($\sigma_z < 0$) in Fig. 6-4(b), and x/L is equal to 0.5. This difference can explain why the expansion of the failure zone in laminate LP is less than that in laminate SP in Fig. 6-2. Moreover, the theoretical analysis shows that the corresponding compressive strength to the first failure achieved in laminate LP (483 MPa) is slightly greater than that in laminate SP (480 MPa). To demonstrate the accuracy of the theoretical analysis, a FE method was adopted, and the results are discussed in the next section.

6.4 Numerical analysis

The great advances in the calculation capacity of computers have made the finite element method (FEM) a powerful tool for understanding the failure mechanism using numerical calculations. In previous studies, models such as the wavy fiber unit cell model and wavy material-orientation model were proposed by Garnich and Karami for unidirectional composites. However, there have been few studies on the effect of fiber waviness in quasi-isotropic composite laminates. The lack of through-thickness stresses made it difficult to employ a 2D shell model based on the plane stress in the *x*-*y* plane. Therefore, a 2D plane mode based on the generalized plane strain was applied in the *x*-*z* plane, and four additional preconditions were employed, as listed below:

(1) The strains ε_{xy} and ε_{yz} were equal to zero in the generalized plane strain model. We found that ε_{xy} was equal to zero in this quasi-isotropic composite laminate according to Eq. (6-3) in the theoretical analysis, but still needed to assume that ε_{yz} was small enough to be ignored.

(2) The middle surface curvatures κ_y and κ_{xy} in the generalized plane strain model were also neglected, although this was contrary to the theoretical results. The values of κ_y and the κ_{xy} were $0.20A\varepsilon_x$ mm^{-2} and $0.07A\varepsilon_x$ mm^{-2} from Eqs. (6-9) and (6-10), respectively.

Therefore, the effects of κ_y and κ_{xy} in this model could be neglected because the amplitudes of the fiber waviness A were very small.

(3) A new material was set as a counterpart of the 45° and -45° layers in the generalized plane strain model. The coefficients of mutual influence corresponding to $\overline{Q}_{16}$ and $\overline{Q}_{26}$ of the 45° and -45° layers could not be input in this 2D model, which affected the engineering constants in these two kinds of layers, such as by decreasing their modules E_x. Therefore, we averaged the elastic stiffness matrix [C] of the 45° and -45° layers using Eq. (6-28) and calculated the engineering constants using Eq. (6-29), where the value of "•" depended on the angle of the layer. Finally, the lost stress τ_{xy} in this model could be obtained from Eq. (6-30).

$$[C]_{\overline{45}} = \frac{1}{2}[C]_{45} + \frac{1}{2}[C]_{-45} \tag{6-28}$$

$$[S]_\theta = [C]_\theta^{-1} = \begin{bmatrix} \frac{1}{E_{x\theta}} & \frac{-\nu_{xy\theta}}{E_{x\theta}} & \frac{-\nu_{xz\theta}}{E_{x\theta}} & 0 & 0 & \bullet \\ \frac{-\nu_{xy\theta}}{E_{x\theta}} & \frac{1}{E_{y\theta}} & \frac{-\nu_{yz\theta}}{E_{y\theta}} & 0 & 0 & \bullet \\ \frac{-\nu_{xz\theta}}{E_{x\theta}} & \frac{-\nu_{yz\theta}}{E_{y\theta}} & \frac{1}{E_z} & 0 & 0 & \bullet \\ 0 & 0 & 0 & \frac{1}{G_{yz\theta}} & \bullet & 0 \\ 0 & 0 & 0 & \bullet & \frac{1}{G_{xz\theta}} & 0 \\ \bullet & \bullet & \bullet & 0 & 0 & \frac{1}{G_{xy\theta}} \end{bmatrix}_\theta \tag{6-29}$$

$$\tau_{xy} = \overline{Q}_{16}\varepsilon_x + \overline{Q}_{26}\varepsilon_y \tag{6-30}$$

(4) The calculated results in the *x*-*z* plane has to be translated into the material coordinate system using Eq. (6-26), and the Tsai–Wu failure factor F_{tw} shown in Eq. (6-27) was used to determine whether or not an element failed. The material properties of the failure elements decreased to 1000 MPa if F_{tw} was greater than one.

Based on the numerical method presented above, two unit models corresponding to single wavelengths of laminates SP and LP were built, respectively. The thicknesses *h* of the models SP and LP were equal to 4.8 mm, and the lengths of the models L_c were 10 mm and 17 mm, respectively. A curvature was introduced as the fiber waviness of each model in the length direction, as shown in Eq. (6-1), where the amplitudes of this waviness were 0.015 mm and 0.016 mm, respectively. To simulate the expansion in the thickness direction, a cohesive zone model (CZM) dominated by the mode I fracture was created, as shown by the blue lines in Fig. 6-5, where major delaminations occurred in the experiments, as shown in Fig. 6-2. The G_{Ic} value of the cohesive elements was 0.25 kN/m, based on double cantilever beam (DCB) tests [93]. An important assumption was suggested in these models: that the cohesive element was degraded to 1 MPa when adjacent composite elements failed.

For boundary conditions, which are also shown in Fig. 6-5, the middle node at the left end of the model was fixed, and the other nodes at the left end were fixed in the

length direction and free in the thickness direction. At the right end of the model, a displacement loading along the negative length direction was applied to all the nodes in this compressive calculation. In addition, the middle node at the right end of the model was fixed in the thickness direction, but the other nodes were free.

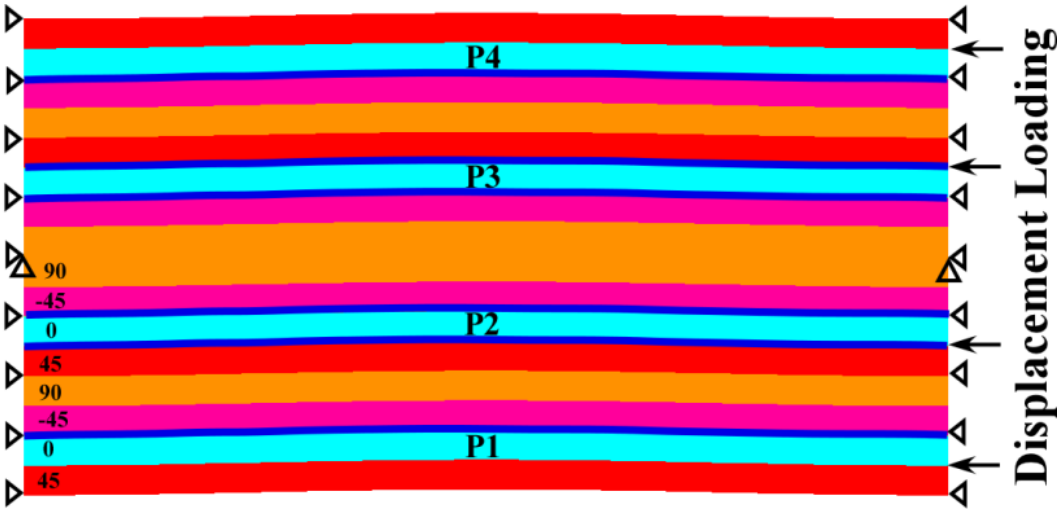

Fig. 6-5. Boundary conditions for simulation

The compressive strengths from the simulations are listed in Table 6-3, and compared with the experimental and theoretical results. We found that laminate LP consistently had a greater compressive strength than laminate SP, although this difference was not obvious. Moreover, there were different failure mechanisms for laminates SP and LP, as shown in Figs. 6-6 and 6-7.

Table 6-3. Comparison of numerical results for models SP and LP

	Wavelength	Compressive strength		
	L_c [mm]	F_c (avg. exp.) [MPa]	F_c (theor.) [MPa]	F_c (FEM) [MPa]
Laminate SP	10	464.8	480	482
Laminate LP	17	487.9	483	491

In model SP, which corresponded to laminate SP, the initial failure elements were found at the ends of layers P1 and P2 and in the middle of layers P3 and P4, as shown in Fig. 6-6(a), where the compressive stress σ_x and tensile through-thickness stress σ_z dominated this failure mode. Thus, we considered this failure mode to be the normal failure mode. The positions of the initial failure elements were a little different from the results of the theoretical analysis, as shown in Fig. 6-4(a). This may have been because of ignoring the deformation κ_y in the model and the thickness effect in the theoretical analysis. Afterward, the damage extended and delamination occurred in the zones of the tensile through-thickness stress, as shown in Fig. 6-6(b) and (c).

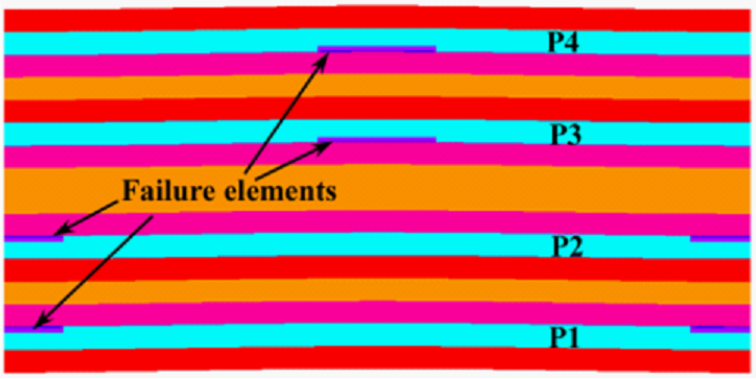

(a)

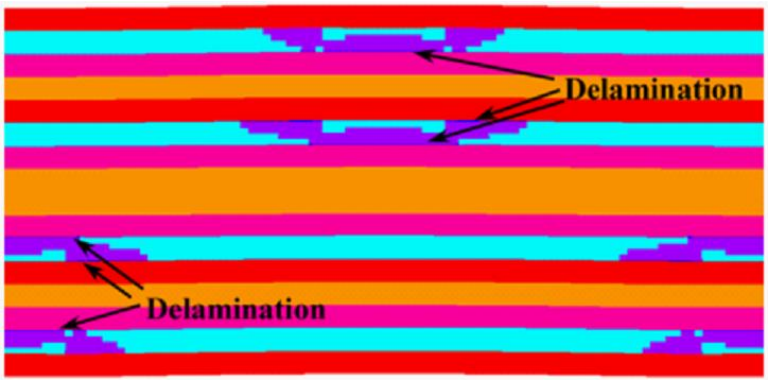

(b)

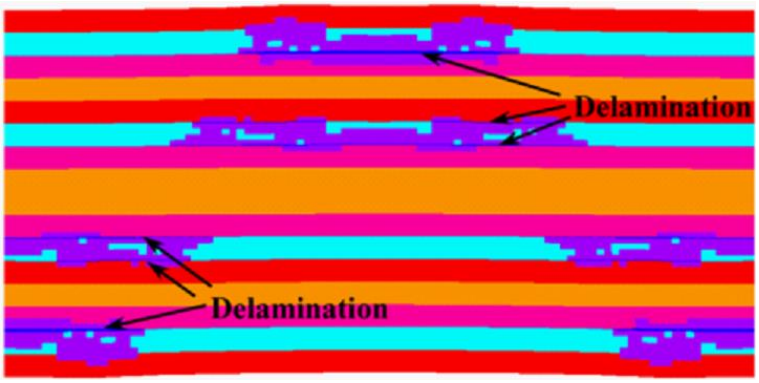

(c)

Fig. 6-6 Failure mechanism in laminate SP: (a) initial failure, (b) failure extension, and (c) ultimate failure.

Fig. 6-7 shows the damage evolution of model LP, which corresponded to laminate LP. The initial damage zone occurred at the middle of layer P1 and the ends of layer P4, as shown in Fig. 6-7(a), which is in accord with the theoretical results shown in Fig. 6-4(b). The occurrence of the initial failure elements was strongly influenced by the compressive stress in the length direction σ_x due to bending. Therefore, the dominant failure mode in laminate LP was the bending compressive failure mode. Next, layers P2 and P3 failed because of the compressive stress σ_x and through-thickness shear stress τ_{zx}, as shown in Fig. 6-7(b). The damage zone in laminate LP is shown in Fig. 6-7(c).

By comparing the initial failure of laminate SP from this section with the theoretical results from Section 6.3, we recognize that the positions of maximal F_{tw} are offset by the effect of the shear stress τ_{zx} in the theoretical analysis. This phenomenon raised the fundamental question of whether a shear failure mode dominated by compressive-shear stress occurs when the amplitude of the fiber waviness A is great enough. Therefore, a parametrical study was conducted to investigate the shear failure mode, as reported in the next section.

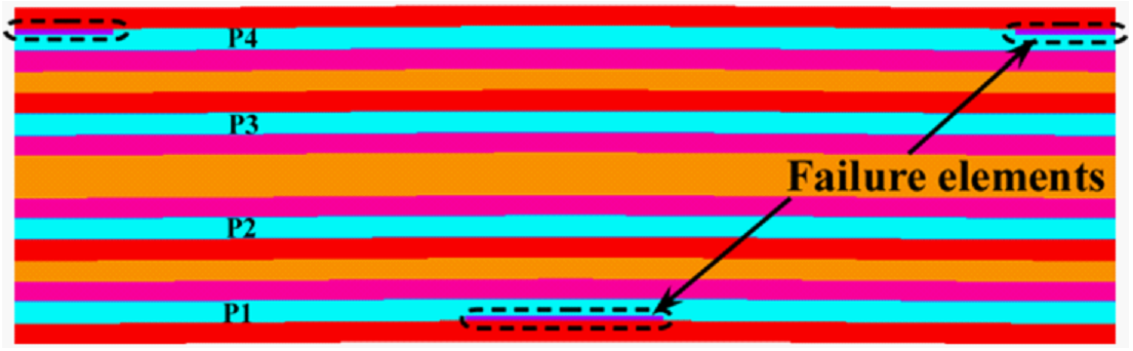

(a)

(b)

(c)

Fig. 6-7 Failure mechanism in laminate LP: (a) initial failure, (b) failure extension, and (c) ultimate failure.

6.5 Parametrical analysis

In order to investigate the shear failure mode, eight models with different wavelengths were created, and then five different amplitude-to-wavelength ratios R_{out} were introduced into each model. The wavelengths of the models ranged from 6 mm to 28 mm, and the maximum ratio was equivalent to 0.01 in each model. The compressive strengths were normalized based on the maximum compressive strength (498 MPa) from FEM calculations with R_{out} equal to zero, and are shown in Fig. 6-8. Four regions with distinct failure mechanisms were found: region C was an axial compressive failure mode; regions N and B corresponded to the normal failure mode as Fig. 6-9(a) and bending failure mode as Fig. 6-9(b), respectively; and region S was the shear failure mode in Fig. 6-9(c).

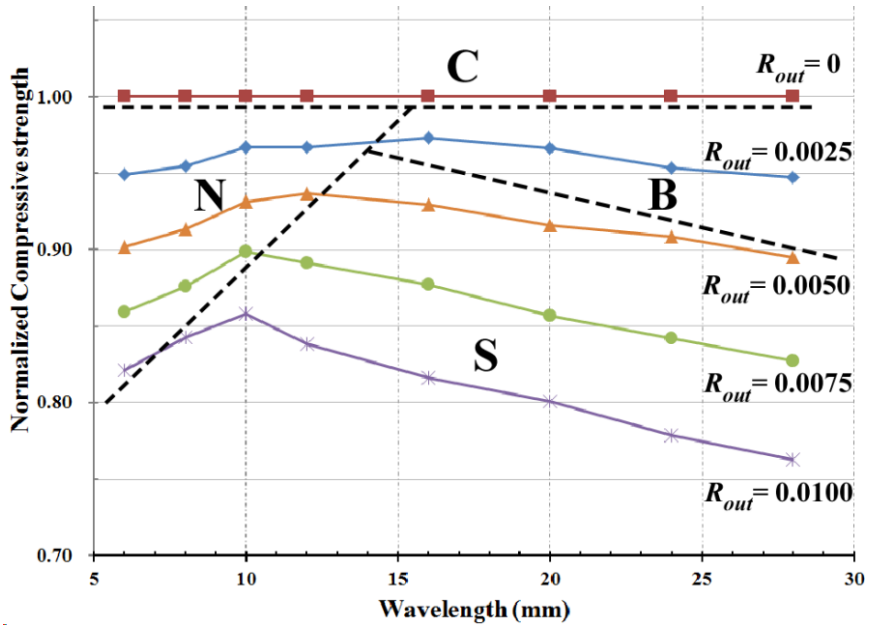

Fig. 6-8 Normalized compressive strengths from parametrical study on ratios.

The normalized compressive strengths showed a complex tendency because of the different failure mechanisms shown in Fig. 6-8. In region N, the compressive strengths increased with decreasing ratio and increasing wavelength. This was because the tensile through-thickness stress decreased quickly at the same compressive stress when the wavelength was long with a small curvature. When the wavelengths increased with a smaller ratio, 0.0025, the model failed by slight bending in region B. Therefore, the normalized compressive stress decreased with an increase in the wavelength. Meanwhile, if the ratio increased, the shear stress increased and dominated the failure mode, with compressive stress in region S. Thus, the laminate damage was from the shear failure mode. Similarly, the compressive strength decreased with increasing wavelength because of the bending deformation, with the exception of a point whose wavelength was 8 mm at the R_{out} equal to 0.01. This could be explained by the fact that the initial failure elements failed in the zone of tensile through-thickness stress at that point, thus the combined shear, normal and compressive stress caused the initial failure. Whereas the other points in region S failed in the zone of compressive through-thickness stress, and only shear and compressive stress dominate the initial failure. Moreover, the maximum strength could be observed near the boundaries between regions N and B or S for a fixed ratio, which implied that a good wavelength

design for carbon fabrics could improve the compressive strength of laminates if the amplitude-to-wavelength ratio was known.

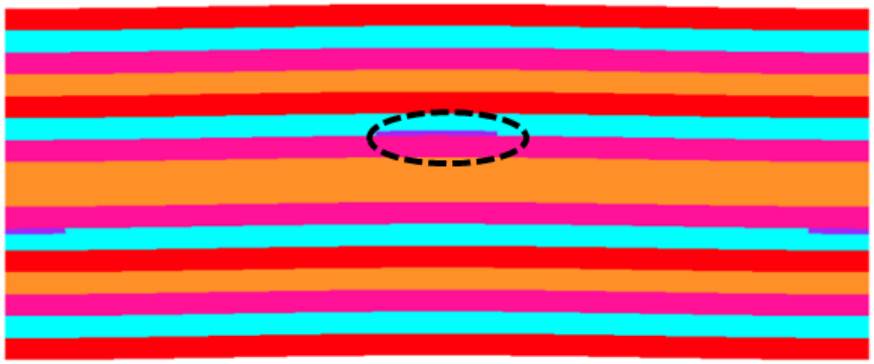

(a)

(b)

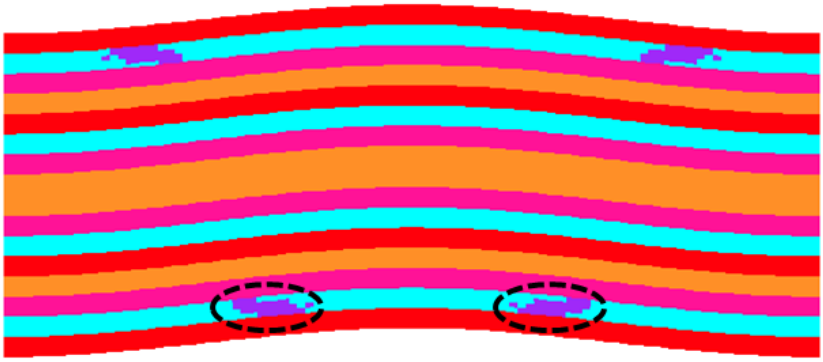

(c)

Fig. 6-9 Three types of failure modes: (a) normal failure mode, (b) bending failure mode and (c) shear failure mode

6.6 Conclusions

The effect of fiber waviness on the compressive strength of quasi-isotropic composite laminates was studied in this paper. Compressive experiments were conducted first, and it was shown that the compressive strength of composite laminates fabricated with LP fabric was higher than that fabricated with SP fabric. Then, theoretical and numerical analyses were performed and the results were compared with the strengths from the experiments to obtain the different failure mechanisms for these two kinds of laminates.

A parameter investigation was conducted to analyze the effects of the wavelength of the fiber waviness and the amplitude-to-wavelength ratio, and four failure modes were mapped. This suggested that the configuration of the fiber waviness had a strong effect on the compressive strength of the quasi-isotropic composite laminates, and an optimized design for the configuration of the fiber waviness in a carbon fabric could improve the compressive strength.

Chapter 7

Effect of in-plane fiber waviness on composite laminates

7.1 Introduction

Experimental and theoretical analysis are carried out to investigate the effect of in-plane fiber waviness on compressive strength of the composite laminate in this chapter. SP and TP fabrics are used for this study. The compressive strengths of 0° ply of the composite laminate are obtained by a back-out method. The experiments show that the compressive strengths decreases with in-plane fiber waviness increasing. Furthermore, a two-dimensional model is proposed so as to explain our experimental results. The numerical results indicate that the tensile stress along the weft direction of the composite caused by the in-plane fiber waviness and compressive stress along the warp direction diminish the compressive strengths.

7.2 Experimental results

To reckon the E_c and F_c of 0°-ply (E_{xc}^0 and F_{xc}^0), the experimental results of the quasi-isotropic laminates are evaluated via the back out method, on which the design and compressive properties of the composite laminates are based; In addition, simulation of the 0°-ply (rather than the quasi-isotropic lay-up) helps to reduce the computational complexity of the numerical models. The back out method consists of three steps, namely:

a. Chamis' mechanistic theory is used to determine theoretical compressive properties of the unidirectional composites [94],

b. Back-out factors *BF*, calculated based on the linear lamination theory, are used to determine the E_c and F_c of 0°-ply [80,82,83,95],

$$BF = \left[Q_{11}^0 \frac{A_{22}A_{66} - A_{26}^2}{d} + Q_{12}^0 \frac{A_{16}A_{26} - A_{12}A_{66}}{d} \right] \cdot h \tag{7-1}$$

where

$$d = A_{11}A_{22}A_{66} - A_{11}A_{26}^2 - A_{12}^2A_{66} + 2A_{12}A_{16}A_{26} - A_{16}^2A_{22} \tag{7-2}$$

and

$Q_{ij}^0 = ij^{th}$ entry in the plane stress stiffness matrix of the 0° laminate

$A_{ij} = ij^{th}$ entry in the extensional stiffness matrix of the laminate

h = total laminate thickness

The E_{xc}^{0} and F_{xc}^{0} are calculated from Eqs. (7-3) and (7-4), respectively.

$$E_{xc}^{0} = BF \cdot E_{c} \tag{7-3}$$

$$F_{xc}^{0} = BF \cdot F_{c} \tag{7-4}$$

c. The disparity between the fiber volume fraction of the SP and TP laminates is overcome by normalizing the modulus and strength of the 0°-ply to a volume fraction of 60% [86].

$$E_{xc} = E_{xc}^{0} \cdot \frac{60\%}{V_{fact}} \tag{7-5}$$

$$F_{xc} = F_{xc}^{0} \cdot \frac{60\%}{V_{fact}} \tag{7-6}$$

where

V_{fact} = fiber volume fraction of the actual specimen

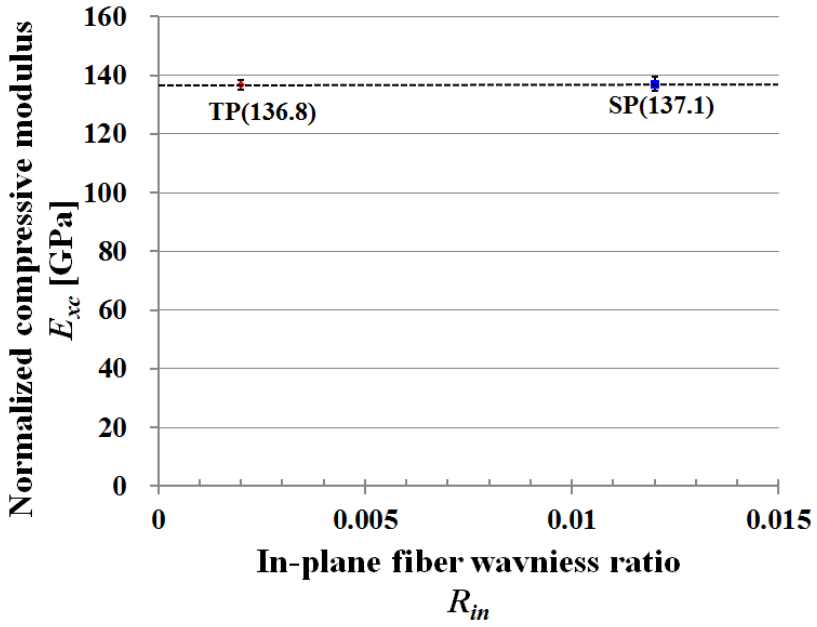

(a)

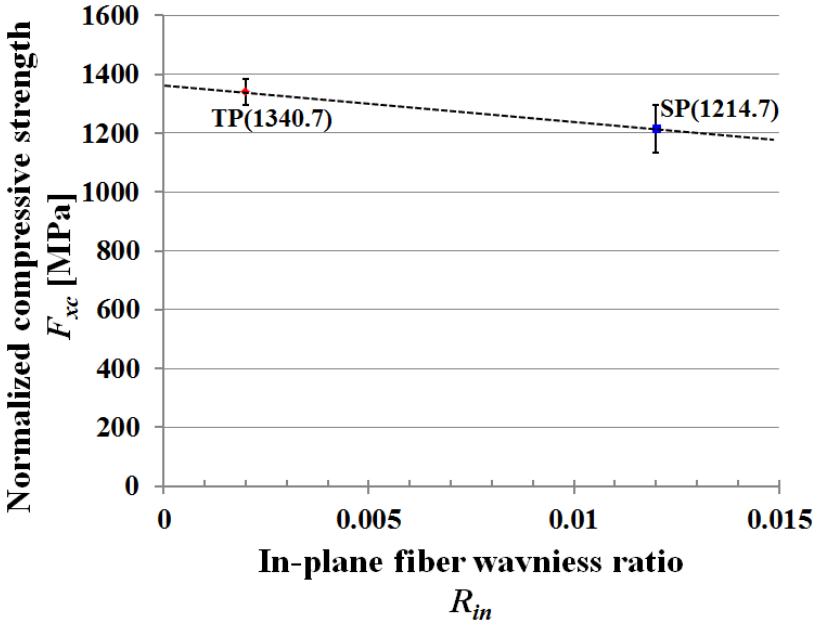

(b)

Fig. 7-1 Normalized compressive properties of the 0°-ply, as determined by using the back-out factor method: (a) normalized compressive modulus and (b) normalized compressive strength.

The back-out factors for the SP and the TP are 2.61 and 2.64, respectively; the normalized compressive properties of the 0°-ply after back-outing are shown in Fig. 7-1. As the figure shows, the SP and TP have similar normalized compressive modulus, E_{xc}, which means the effect of the micro in-plane fiber waviness on compressive modulus is little. But the normalized compressive strength, F_{xc}, of the latter is 10.4% higher than that of the former, and reduces with increasing the in-plane fiber waviness ratio obviously; this indicates that the in-plane fiber waviness has a greater effect on the strength than on the modulus.

7.3 Numerical analysis and discussion

Our experimental findings were clarified by performing a numerical study on the 0°-ply via ANSYS. This study included the modeling of a cell (Fig. 7-2(a)) of the quasi-UD woven fabrics.

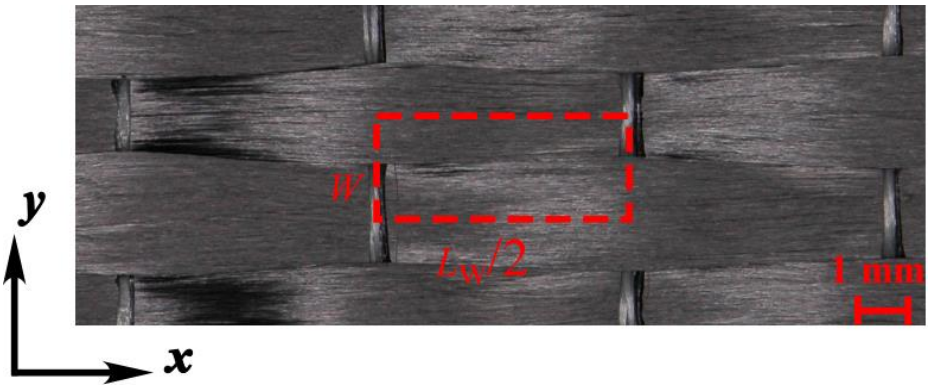

(a)

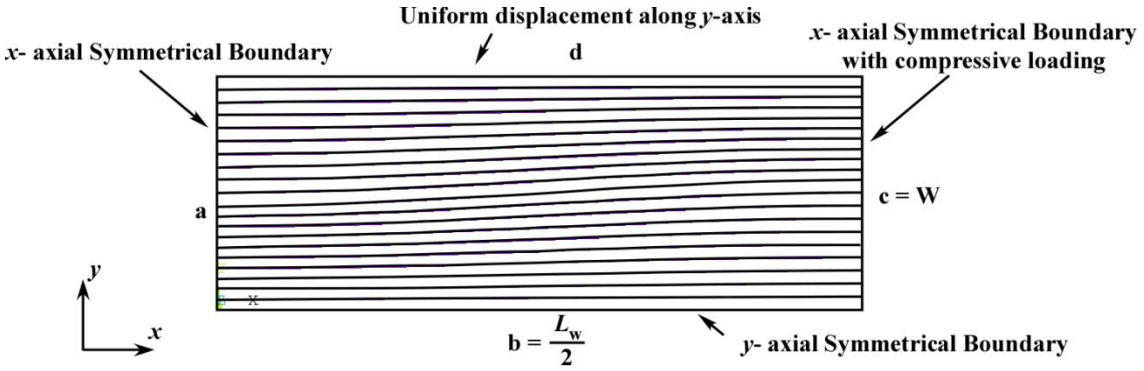

(b)

Fig. 7-2 (a) A cell in the fabric and (b) numerical model of the cell.

Fiber reinforcements with sine curves are represented by elastic beam elements (Fig. 7-2(b)), and a graded fiber distribution is implemented in order to simulate the in-plane fiber waviness. The length of the model along the *x*-axis is equal to half the wavelength, $L_w/2$, and the width along the *y*-axis is the tow width (W). In addition, fiber reinforcements that have the maximum amplitude of the in-plane fiber waviness (A_{in}) are at the center of the model; the amplitude of the reinforcements decreases from the maximum amplitude at the center to zero at the edges b and d. The beam elements are, however, incapable of maintaining the transverse properties of the quasi-UD woven fabric composite and artificial resin, which is represented by shell elements, is used to suspend the reinforcements; appropriate transverse and shear moduli of the composite are defined for the artificial resin [96]. The following parameters are used in the calculations (parameters associated with the artificial resin and the fiber reinforcement are denoted by subscripts *AR* and *FR*, respectively) as follows:

Shear modulus

$$G_{AR} = \frac{G_m}{1-\sqrt{V_f(1-G_m/G_f)}} \tag{7-7}$$

Poisson's ratio

$$\nu_{AR} = V_f \nu_f + (1-V_f)\nu_m \tag{7-8}$$

Young's modulus

$$E_{AR} = 2G_{AR}(1+\nu_{AR}) \tag{7-9}$$

Young's modulus

$$E_{FR} = \frac{E_{xc} - (1-V_f)E_{AR}}{V_f} \tag{7-10}$$

Shell thickness

$$T_{AR} = \frac{(1-V_f)w_f}{V_f \rho_f} \tag{7-11}$$

Radius

$$R_{FR} = \sqrt{\frac{w_f W}{m\pi\rho_f}} \tag{7-12}$$

where *m* is number of lines in the elements that represent the reinforcement.

At a fiber volume fraction of 60%, a Young's modulus of 14 GPa is determined for the artificial resin. Moreover, the value of maximum von Mises stress that prescribes a strain of 1% is used to determine when initial failure occurs [96,97]; the magnitude of the material properties of the failed resin elements will decrease to 1% if the von Mises stress exceeds 140 MPa due to the carbon fiber composite is brittle material.

Symmetrical boundaries were applied to edges a, b, and c (Fig. 7-2(b)), and *x* and *y* are designated as the warp and weft directions, respectively, of the specimen. The edge d undergoes uniform displacement along the *y* direction. In addition, a compressive displacement loading along the negative warp direction is applied to edge c. In contrast,

some researchers used the boundary conditions of free edges on the edges b and d to simulate lager deformation of the kinking bands [98,99], however, the symmetrical boundaries match the periodic pattern in the quasi-UD woven fabrics better than the free edges.

The axial stress-end shortening response of the SP and the TP model is shown in Fig. 7-3, and both models exhibit a linear response before initial failure. The maximum von Mises stress occurs at the top left and bottom right corners of the both models due to the effect of the in-plane fiber waviness (Fig.7-4), however, the greater in-plane fiber waviness of the SP model makes a greater difference between the maximum and minimum von Mises stress than that in the TP model (20.0 MPa vs 4.5 MPa). Hereafter in the case of the SP model, initial failure in the shell elements occurs in the region of the maximum von Mises stress (Fig. 7-5(a)) at a strain of 8700 $\mu\varepsilon$. This failure is attributed to the tensile stress (49.2 MPa), which results from the in-plane fiber waviness, and compressive stress (108.5 MPa) along the weft and warp directions, respectively. In contrast, shear stress in the center of the model is only 4.9 MPa, which is not the major stress leading to the initial failure. The fiber reinforcements are subsequently deflected, as indicated by failure of shell elements along the weft direction, and this failure propagates at a stress of 1217 MPa (Fig. 7-5(b)). Moreover, the loading capacity of the SP model is

lost near an applied stress of 1228 MPa and a strain of 8950 $\mu\varepsilon$ (Fig. 7-5(c)). In the TP model, the tensile stress (11.4 MPa) along the weft direction is significantly lower than that in the SP model. However, initial failure (Fig. 7-6(a)) in the TP model occurs at a higher compressive stress (134.0 MPa vs. 108.5 MPa) and strain (9700 $\mu\varepsilon$ vs. 8700 $\mu\varepsilon$) than in the SP model. The failure then propagates and the reinforcements are deflected at stresses lower than 1408 MPa, as indicated by the failure shell elements; this deflection continues until a compressive strength of 1415 MPa is reached (Figs. 7-6(b) and (c)).

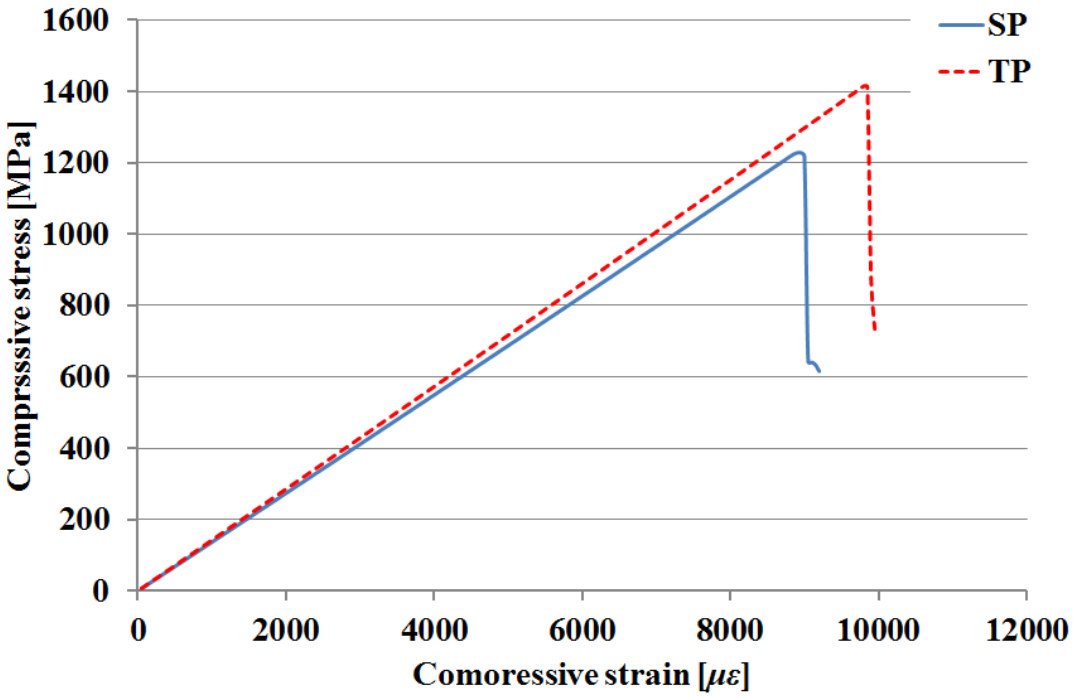

Fig. 7-3 Axial stress-end shortening responses of the SP and TP models.

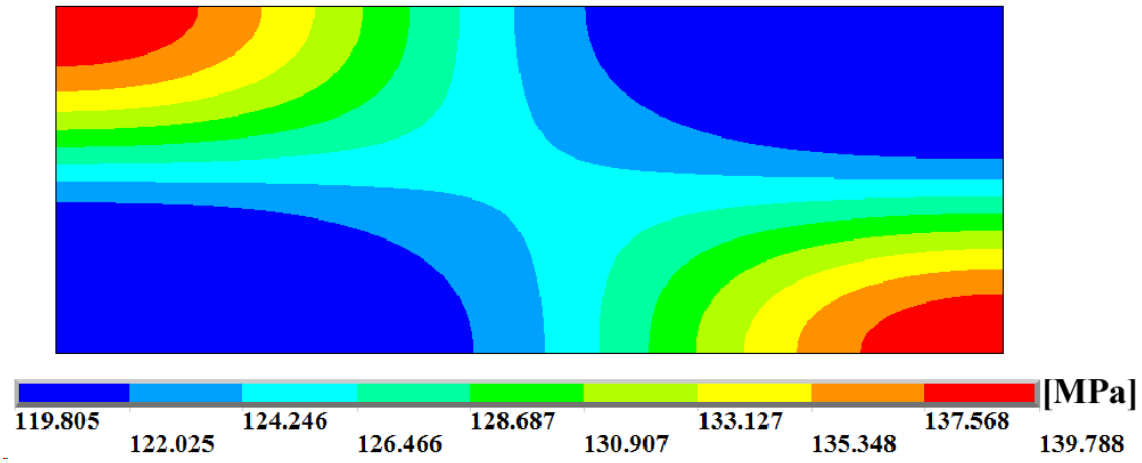

(a)

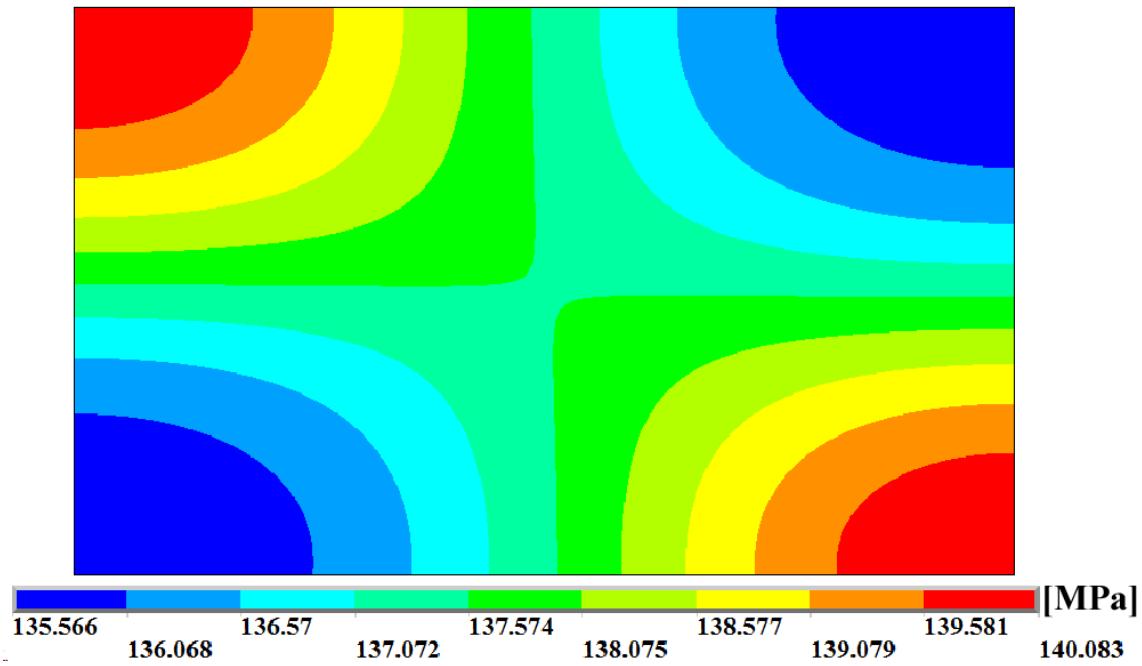

(b)

Fig. 7-4 Von Mmises stress distributions: (a) the SP model and (b) the TP model.

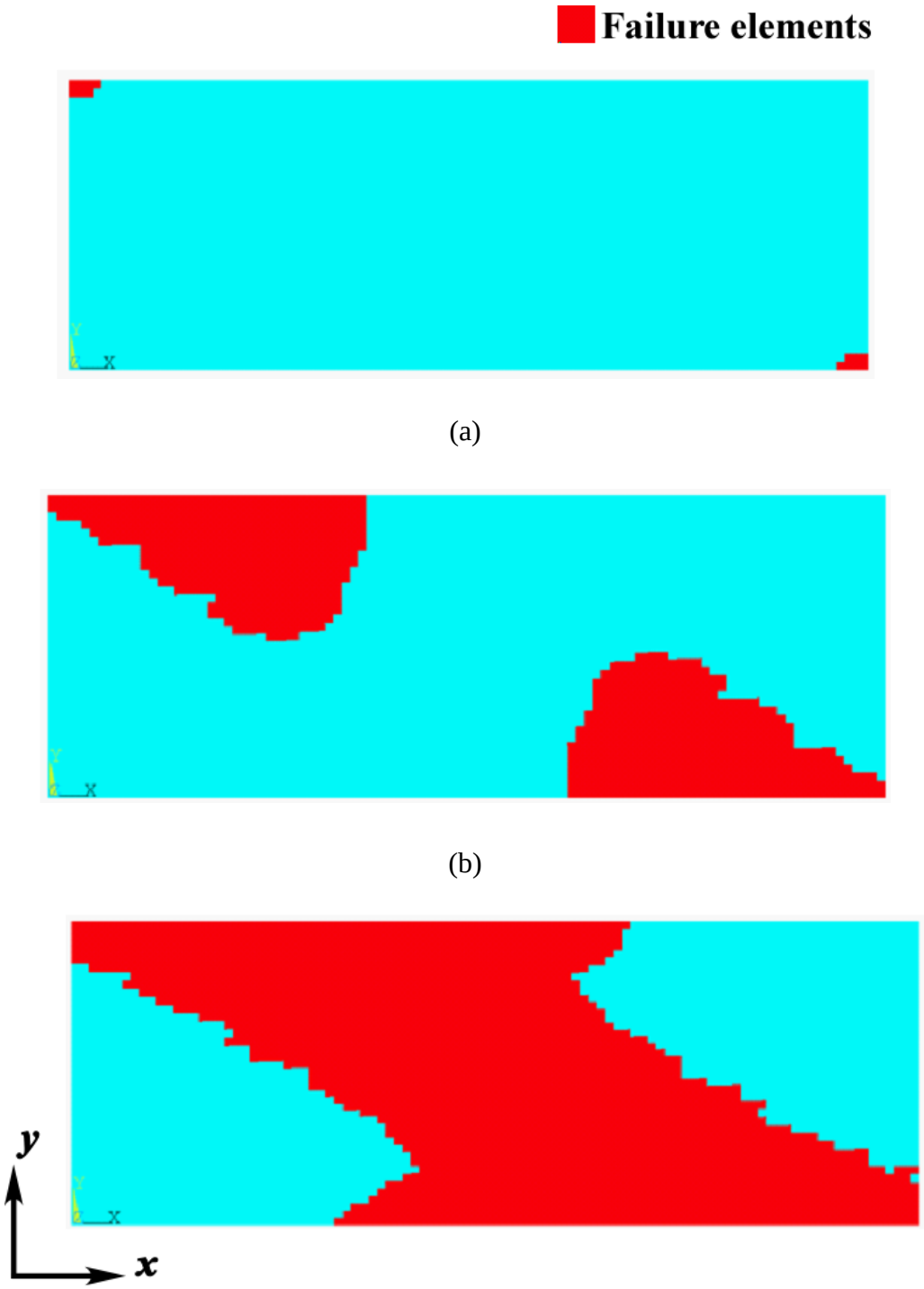

Fig. 7-5 Failure processes in shell elements of the SP model: (a) 8700 $\mu\varepsilon$, 1203 MPa, (b) 8750 $\mu\varepsilon$, 1217 MPa, and (c) 8950 $\mu\varepsilon$, 1228 MPa.

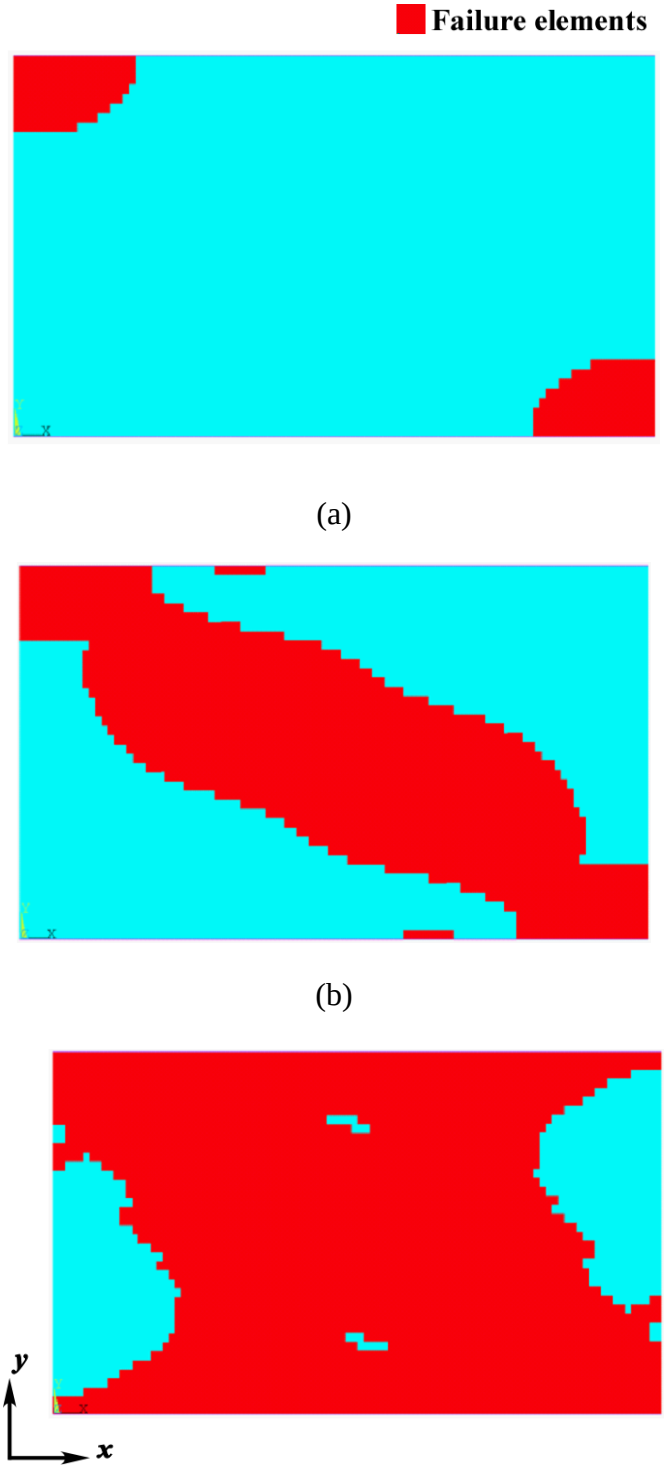

(a)

(b)

(c)

Fig. 7-6 Failure processes in shell elements of the TP model: (a) 9700 $\mu\varepsilon$, 1400 MPa, (b) 9750 $\mu\varepsilon$, 1408 MPa, and (c) 9800 $\mu\varepsilon$, 1415 MPa.

The results reveal that the in-plane fiber waviness reduces the compressive modulus and strength in the numerical models. For example, the respective modulus and strength obtained in the TP model (142.3 GPa and 1415 MPa) are 4.2% and 15.2% higher than those in the SP (136.5 GPa and 1228 MPa), and this result also shows the effect of the in-plane fiber waviness on the strength is greater than on the modulus, which are consistent with the experimental findings. Furthermore, the results from both models concur with those from the experiments, as evidenced by compressive strengths that are only 1.1% (SP) and 5.5% (TP) greater than the experimental values. The calculations also indicate that the micro in-plane fiber waviness results in the tensile stress along the weft direction; this stress, in turn, leads to initial failure prior to pure compressive failure along the warp direction. The reasons why the shear stress doesn't dominate the initial failure are shown as follows: (a) the constraints of the symmetrical and uniform displacement boundaries on the edges b and d, respectively, are stronger than those of free edges; (b) the micro in-plane fiber waviness in the quasi-UD woven fabric composite is relatively lower than that in the Z-pinned composite.

7.4 Conclusions

The effect of in-plane fiber waviness on the compressive properties of a quasi-UD woven fabric composite is investigated. A back-out factor method is used to determine the compressive modulus and strength of 0°-ply from the experimentally determined compressive properties. The reduction in the compressive strength, owing to the in-plane fiber waviness, becomes evident at a fiber volume fraction of 60% in the compression tests. And the effect of the in-plane fiber waviness on the compressive strength is greater than on the compressive modulus.

The in-plane fiber waviness was accounted for in the numerical analysis used to explain the experimental findings. In fact, the calculations have a good agreement on the tendency of effect of the in-plane fiber waviness on the compressive properties with the experiments, moreover, these show that this waviness results in a tensile stress along the weft direction of the composites; this stress combined with the compressive stress along the warp direction leads to initial failure. These results indicate that the in-plane fiber waviness can be reduced by using architectures that consist of low areal weights and low pitch density in the weft direction.

Chapter 8

Summary

The effect of out-of-plane and in-plane fiber waviness on compressive properties of quasi-UD woven fabric composites is investigated in this research. Three types of quasi-UD woven fabrics with different pitch intervals or pitch densities were used, namely, standard pitch fabric, long pitch fabric and thin pitch fabric. The in-plane parameters associated with this waviness were measured in three quasi-UD woven fabrics; three composite laminates (one from each fabric) were fabricated via the vacuum-assisted resin transfer molding (VaRTM) process. Moreover, the wavelengths and amplitudes of out-of-plane fiber waviness were measured using the fast Fourier transform (FFT) method.

Compression tests were performed in order to determine the effect of the waviness on the compressive properties, and the normalized experimental results show that both out-of-plane and in-plane fiber waviness have a greater effect on compressive strength than that on the compressive modulus. In addition, the failure mechanisms of the composite were identified by using finite element method in this study. The models for out-of-plane fiber waviness revealed that initial failure depends on the wavelength and the amplitude-to-wavelength ratio of the out-of-plane fiber waviness and four

compressive failure modes were found: the axial compressive, normal, bending, and shear failure modes were found in a parametrical study. The models for in-plane fiber waviness shows initial failure due to the micro in-plane fiber waviness is more sensitive to a combination of the tensile and compressive stresses along the weft and warp directions, respectively, than the shear stress of the composite.

Although both out-of-plane and in-plane fiber waviness have an adverse effect on the compressive properties of the composites, this research shows the negative effect of in-plane fiber waviness is greater than out-of-plane fiber waviness due to the in-plane fiber waviness ratio is a magnitude greater than the out-of-plane fiber waviness ratio. Moreover, an optimized design on the pitch intervals and pitch densities is able to decrease the out-of-plane or in-plane fiber waviness in the quasi-UD woven fabrics and improve the compressive properties of the composites consequently.

Reference

[1] Mallick PK. Fiber-reinforced composites: materials, manufacturing, and design: CRC press; 1993.

[2] http://www.1001crash.com/index-page-composite-lg-2.html

[3] Potluri P, Young RJ, Rashed K, Manan A, Shyng YT. Meso-scale strain mapping in UD woven composites. Compos Part a-Appl S. 2009;40(12):1838-1845.

[4] Vandreumel WHM, Kamp JLM. Non-hookean behavior in fiber direction of carbon-fiber composites and influence of fiber waviness on tensile properties. J Compos Mater. 1977;11(Oct):461-469.

[5] Berthelot JM. Effect of fiber misalignment on the elastic properties of oriented discontinuous fiber composites. Fibre Sci Technol. 1982;17(1):25-39.

[6] Potluri P, Thammandra VS. Influence of uniaxial and biaxial tension on meso-scale geometry and strain fields in a woven composite. Compos Struct. 2007;77(3):405-418.

[7] Potter K, Khan B, Wisnom M, Bell T, Stevens J. Variability, fibre waviness and misalignment in the determination of the properties of composite materials and structures. Compos Part a-Appl S. 2008;39(9):1343-1354.

[8] El-Hajjar RF, Petersen DR. Gaussian function characterization of unnotched tension behavior in a carbon/epoxy composite containing localized fiber waviness. Compos Struct. 2011;93(9):2400-2408.

[9] Croft K, Lessard L, Pasini D, Hojjati M, Chen JH, Yousefpour A. Experimental study of the effect of automated fiber placement induced defects on performance of composite laminates. Compos Part a-Appl S. 2011;42(5):484-491.

[10] Tsai CH, Zhang C, Jack DA, Liang RC, Wang B. The effect of inclusion waviness and waviness distribution on elastic properties of fiber-reinforced composites. Compos Part B-Eng. 2011;42(1):62-70.

[11] Hillig WB. Effect of fiber misalignment on the fracture-behavior of fiber-reinforced composites .1. Experimental. J Mater Sci. 1994;29(2):419-423.

[12] Hillig WB. Effect of fiber misalignment on fracture-behavior of fiber-reinforced composites .2. Theoretical Modeling. J Mater Sci. 1994;29(4):899-920.

[13] Schmidt F, Rheinfurth M, Horst P, Busse G. Effects of local fibre waviness on damage mechanisms and fatigue behaviour of biaxially loaded tube specimens. Compos Sci Technol. 2012;72(10):1075-1082.

[14] Wang J, Potter KD, Etches J. Experimental investigation and characterisation techniques of compressive fatigue failure of composites with fibre waviness at ply drops. Compos Struct. 2013;100:398-403.

[15] Chaudhuri RA. Effects of fiber misalignment and transverse shear modulus on localization and shear crippling instability in thick imperfect cross-ply rings under external pressure. Compos Struct. 2008;82(4):587-599.

[16] Marklund E, Asp LE, Olsson R. Transverse strength of unidirectional non-crimp fabric composites: Multiscale modelling. Compos Part B-Eng. 2014;65:47-56.

[17] Rosen BW. Mechanics of composite strengthening. Fiber Composite Materials. Metals Park, OH.: American Society of Metals Seminar; 1965.

[18] Dow NF, Rosen BW. Evaluations of Filament-Reinforced Composites for Aerospace Structural Applications. 1965.

[19] Argon AS. Fracture of composites. In: Herbert H, editor. Treatise on Materials Science and Technology, vol. Volume 1: Elsevier; 1972. p. 79-114.

[20] Budiansky B. Micromechanics. Comput Struct. 1983;16(1-4):3-12.

[21] Budiansky B, Fleck NA. Compressive failure of fiber composites. J Mech Phys Solids. 1993;41(1):183-211.

[22] Budiansky B, Fleck NA. Compressive kinking of fibre composites: a topical review. Appl Mech Rev. 1994;47(6):246-S270.

[23] Fleck NA, Deng L, Budiansky B. Prediction of kink width in compressed fiber composites. J Appl Mech. 1995;62(2):329-337.

[24] Slaughter WS, Fleck NA. Microbuckling of fiber composites with random initial fiber waviness. J Mech Phys Solids. 1994;42(11):1743-1766.

[25] Fleck NA, Liu DQ. Microbuckle initiation from a patch of large amplitude fibre waviness in a composite under compression and bending. Eur J Mech a-Solid. 2001;20(1):23-37.

[26] Evans AG, Adler WF. Kinking as a mode of structural degradation in carbon fiber composites. Acta Metallurgica. 1978;26(5):725-738.

[27] Wisnom MR. The effect of fiber misalignment on the compressive strength of unidirectional carbon-fiber epoxy. Composites. 1990;21(5):403-407.

[28] Jelf P, Fleck N. Compression failure mechanisms in unidirectional composites. J Compos Mater. 1992;26(18):2706-2726.

[29] Shuart MJ. Failure of compression-loaded multidirectional composite laminates. AIAA J. 1989;27(9):1274-1279.

[30] Fleck NA, Shu JY. Microbuckle Initiation in Fiber Composites - a Finite-Element Study. J Mech Phys Solids. 1995;43(12):1887-1918.

[31] Sun CT, Jun AW. Compressive strength of unidirectional fiber composites with matrix nonlinearity. Compos Sci Technol. 1994;52(4):577-587.

[32] Wisnom MR. Nonlinear-analysis of misaligned unidirectional carbon fiber-epoxy compression specimens. Compos Eng. 1993;3(6):547-556.

[33] Wisnom MR. Analysis of shear instability in compression due to fiber waviness. J Reinf Plast Comp. 1993;12(11):1171-1189.

[34] Kyriakides S, Arseculeratne R, Perry EJ, Liechti KM. On the compressive failure of fiber-reinforced composites. Int J Solids Struct. 1995;32(6-7):689-738.

[35] Hsiao HM, Wooh SC, Daniel IU. Fabrication methods for unidirectional and crossply composites with fiber waviness. J Adv Mater. 1995;26(2):19-26.

[36] Daniel IM, Hsiao HM, Wooh SC. Failure mechanisms in thick composites under compressive loading. Compos Part B-Eng. 1996;27(6):543-552.

[37] Hsiao HM, Daniel IM. Elastic properties of composites with fiber waviness. Compos Part a-Appl S. 1996;27(10):931-941.

[38] Hsiao HM, Daniel IM. Nonlinear elastic behavior of unidirectionai composites with fiber waviness under compressive loading. J Eng Mater-T Asme. 1996;118(4):561-570.

[39] Hsiao HM, Daniel IM. Nonlinear and dynamic compressive behavior of composites with fiber waviness. Am Soc Test Mater. 2000;1357:223-237.

[40] Chun HJ, Shin JY, Daniel IM. Nonlinear behavior of thick composites with uniform fiber waviness. AIAA J. 2000;38(10):1949-1955.

[41] Adams DO, Hyer MW. Effects of layer waviness on the compression strength of thermoplastic composite laminates. J Reinf Plast Comp. 1993;12(4):414-429.

[42] Adams DO, Hyer MW. Effects of layer waviness on the compression fatigue performance of thermoplastic composite laminates. Int J Fatigue. 1994;16(6):385-391.

[43] Garnich MR, Karami G. Finite element micromechanics for stiffness and strength of wavy fiber composites. J Compos Mater. 2004;38(4):273-292.

[44] Garnich MR, Karami G. Localized fiber waviness and implications for failure in unidirectional composites. J Compos Mater. 2005;39(14):1225-1245.

[45] Karami G, Garnich A. Micromechanical study of thermoelastic behavior of composites with periodic fiber waviness. Compos Part B-Eng. 2005;36(3):241-248.

[46] Karami G, Garnich M. Effective moduli and failure considerations for composites with periodic fiber waviness. Compos Struct. 2005;67(4):461-475.

[47] Bogdanovich AE, Mohamed MH. Three-Dimensional Reinforcements for Composites. Sampe J. 2009;45(6):8-28.

[48] Mouritz AP, Chang P, Isa MD. Z-Pin composites: aerospace structural design considerations. J Aerospace Eng. 2011;24(4):425-432.

[49] Knopp A, Scharr G. Effect of z-pin surface treatment on delamination and debonding properties of z-pinned composite laminates. J Mater Sci. 2014;49(4):1674-1683.

[50] Wei YQ, Zhang JQ. Characterization of microstructure in stitched unidirectional composite laminates. Compos Part a-Appl S. 2008;39(5):815-824.

[51] Mouritz AP. Compression properties of z-pinned composite laminates. Compos Sci Technol. 2007;67(15-16):3110-3120.

[52] Mouritz AP. Review of z-pinned composite laminates. Compos Part a-Appl S. 2007;38(12):2383-2397.

[53] O'Brien TK, Krueger R. Influence of compression and shear on the strength of composite laminates with z-pinned reinforcement. Appl Compos Mater. 2006;13(3):173-189.

[54] Steeves CA, Fleck NA. In-plane properties of composite laminates with through-thickness pin reinforcement. Int J Solids Struct. 2006;43(10):3197-3212.

[55] Xie SL, Zhang JQ, Guo ZS, Hu HJ. Prediction of compressive strength of z-pinned unidirectional composite laminates. J Compos Mater. 2012;46(4):383-390.

[56] Yurgartis SW. Measurement of small angle fiber misalignments in continuous fiber composites. Compos Sci Technol. 1987;30(4):279-293.

[57] Zak G, Park C, Benhabib B. Estimation of three-dimensional fibre-orientation distribution in short-fibre composites by a two-section method. J Compos Mater. 2001;35(4):316-339.

[58] Clarke AR, Archenhold G, Davidson NC. A novel technique for determining the 3D spatial distribution of glass fibres in polymer composites. Compos Sci Technol. 1995;55(1):75-91.

[59] Clarke A, Archenhold G, Davidson N, Slaughter W, Fleck N. Determining the power spectral density of the waviness of unidirectional glass fibres in polymer composites. Appl Compos Mater. 1995;2(4):233-243.

[60] Creighton CJ, Sutcliffe MPF, Clyne TW. A multiple field image analysis procedure for characterisation of fibre alignment in composites. Compos Part a-Appl S. 2001;32(2):221-229.

[61] Sutcliffe M, Lemanski S, Scott A. Measurement of fibre waviness in industrial composite components. Compos Sci Technol. 2012;72(16):2016-2023.

[62] Kratmann KK, Sutcliffe MPF, Lilleheden LT, Pyrz R, Thomsen OT. A novel image analysis procedure for measuring fibre misalignment in unidirectional fibre composites. Compos Sci Technol. 2009;69(2):228-238.

[63] Matsunoshita A. Molding initial imperfections and compression-after-impact properties of VaRTM composites. Master's thesis, Kyushu University, Department of Aeronautics and Astronautics, 2010.

[64] Maekawa K. Compression-After-Impact properties of VaRTM composites fabricated by ud woven fabrics. Bachelor's thesis, Kyushu University, Department of Aeronautics and Astronautics, 2010.

[65] Mitsubishi Rayon. Product data sheet PYROFIL # 1053 Series.

[66] http://www.nittobo.co.jp/business/glassfiber/industrial/manufacture/tape

[67] NagaseChemtex. DENATOOL XNR/H6809 Technical Sheet. 2009.

[68] https://www.nde-ed.org/EducationResources/HighSchool/Sound/immersion.htm

[69] https://en.wikipedia.org/wiki/Radar_display

[70] http://www.compositesworld.com/articles/airbus-a350-update-braf-fpp

[71] Standard test method for compressive properties of polymer matrix composite materials with unsupported gage section by shear loading.

[72] http://www.wyomingtestfixtures.com/Products/b6.html

[73] Adams D, Odom E. Influence of test fixture configuration on the measured compressive strength of a composite material. J Compos Tech Res. 1991;13(1):36-40.

[74] Chaterjee S, Adams DF, Oplinger D. Test methods for composites: a status report. Volume 2. Compression Test Methods. DTIC Document; 1993.

[75] http://www.wyomingtestfixtures.com/Products/b3.html

[76] Standard test method for compressive properties of rigid plastics.

[77] http://www.wyomingtestfixtures.com/Products/b2.html

[78] Adams D, Lewis E. Influence of specimen gage length and loading method on the axial compressive strength of a unidirectional composite material. Exp Mech. 1991;31(1):14-20.

[79] Westberg R, Abdallah M. An experimental and analytical evaluation of three compressive test methods for unidirectional graphite epoxy composites. 6th International Congress on Experimental Mechanics, vol. 11988. p. 350-361.

[80] Standard Test method for compressive properties of polymer matrix composite materials using a combined loading compression (CLC) test fixture

[81] http://www.wyomingtestfixtures.com/Products/b1.html

[82] Adams DF, Welsh JS. The Wyoming combined loading compression (CLC) test method. J Compos Tech Res. 1997;19(3):123-133.

[83] Wegner PM, Adams DF. Verification of the combined load compression (CLC) test method. Report No. DOT/FAA/AR-00/26. Federal Aviation Administration Technical Center, New Jersey, 2000.

[84] Shimokawa T, Hamaguchi Y, Kakuta Y, Katoh H, Sanda T, Mizuno H, Toi Y. Effect of isothermal aging on ultimate strength of high-temperature composite materials for SST structures. J Compos Mater. 1999;33(12): 1104-18.

[85] Uda N, Ono K, Kunoo K. Compression fatigue failure of CFRP laminates with impact damage. Compos Sci Technol. 2009;69(14):2308-14.

[86] U.S. Dept. of Defense. Guidelines for property testing of composite. In: U.S. Dept. of Defense, editor. Composite Materials Handbook Volume 1: Polymer Matrix Composites - Guidelines for Characterization of Structural Materials. Pennsylvania: SAE International, 2012.p. 1-119.

[87] Odom E, Adams D. Failure modes of unidirectional carbon/epoxy composite compression specimens. Composites. 1990;21(4):289-296.

[88] Kelly G, Hallstrom S. Bearing strength of carbon fibre/epoxy laminates: effects of bolt-hole clearance. Compos Part B-Eng. 2004;35(4):331-343.

[89] Liu H. Material mechanics. Beijing: Higher Education Press, 2004.

[90] Whitney JM. Structural analysis of laminated anisotropic plates: CRC Press; 1987.

[91] Tsai SW. Introduction to composite materials. Stephen W. Tsai, H. Thomas Hahn. Westport, Conn: Technomic Pub; 1980.

[92] Narayanaswami R, Adelman HM. Evaluation of tensor polynomial and Hoffman strength theories for composite-materials. J Compos Mater. 1977;11(Oct):366-377.

[93] Hashimoto Y. Interlaminar fracture properties of carbon fiber composites with through-thickness shape-memory-alloy wire reinforcement. Master's thesis, Kyushu University, Department of Aeronautics and Astronautics, 2014.

[94] Chamis CC, Handler LM, Manderscheid J. Composite nanomechanics: a mechanistic properties prediction. NASA/TM 2007-214673. 2007.

[95] CMH-17-1F. Polymer Matrix Composites, Volume 1–Guidelines for Characterization of Structural Materials. ASTM International, West Conshohocken, PA19428, Section 2.4.2.

[96] Lemanski SL, Sutcliffe MPF. Compressive failure of finite size unidirectional composite laminates with a region of fibre waviness. Compos Part a-Appl S. 2012;43(3):435-44.

[97] Joffe R, Mattsson D, Modniks J, Varna J. Compressive failure analysis of non-crimp fabric composites with large out-of-plane misalignment of fiber bundles. Compos Part a-Appl S. 2005;36(8):1030-46.

[98] Prabhakar P, Waas AM. Interaction between kinking and splitting in the compressive failure of unidirectional fiber reinforced laminated composites. Compos Struct. 2013;98:85-92.

[99] Huang HJ, Waas AM. Modeling and predicting the compression strength limiting mechanisms in Z-pinned textile composites. Compos Part B-Eng. 2009;40(6):530-9.

Publication records

[1] Wang B, Maekawa K, Uda N, Ono K, and Nagai H. Compressive failure analysis of quasi-isotropic composite laminates fabricated with quasi-unidirectional woven fabric. J Compos Mater. 2016;50(2):231-241.

[2] Wang B, Maekawa K, Uda N, Ono K, and Nagai H. Effect of in-plane fiber waviness on compressive properties of quasi-unidirectional woven fabric composites. 9th Asian-Australasian Conference on Composite Materials, 2014.

[3] Wang B, Maekawa K, Uda N, Ono K, and Nagai H. Compressive failure analysis of composite laminates with fiber waviness. 9th Japan-Korea Joint Symposium on Composite Materials, 2013.

[4] Wang B, Xu F and Liu YG. Buckling analysis of composite stiffened panels with pre-damage under uniaxial compression. Chinese J Appl Mech. 2013;30(1):115-119.

[5] Wang B, Xu F and Qian Y. Numerical analysis of composite stiffened panels' mode jumping under compression. Int J Aerosp LTWT Struct. 2012;2(1):121-136.

[6] Sun Z, Xu F, Xie W, Wang B. Compression after impact performance of composite stiffened panels. Adv Mat Res. 2012,415(417):2231-2235.

Acknowledgements

First, I would like to thank the China Scholarship Council (CSC) for sponsoring me as a doctoral candidate at Kyushu University. The generous financial support from the CSC let me have an opportunity to study in Japan and feel this country by myself.

I would like to express my gratitude and appreciation to my advisor Dr. Nobuhide Uda for his guidance throughout my Ph.D. studies, and Dr. Kousei Ono and Dr. Hiroto Nagai for their time and expertise.

I would also like to thank Mr. Kento Maekawa for his help in VARTM experiments training, and Mitsubishi Rayon Co., Ltd. and Nagase ChemteX Corp. for providing the materials used in the experiments.

Most importantly, my deepest thanks go to my mother, Chunlan Zhang. It is not an easy life for my mother because my father passed away when I was nine years old, but her continuous love and support enable me to reach the milestone in my life. Now, it is time to me repay my mother for her love and care given me from childhood.

Appendix A

Compressive failure analysis of unidirectional laminate fabricated by standard pitch fabric

A.1 Abstract

An in-plane fiber waviness compressive failure analysis of a quasi-unidirectional (UD) woven fabric composite is studied via experimental and theoretical analyses. A quasi-UD woven fabric with standard pitch is used for this study. The two cross-sectional inspections were conducted in the warp and weft direction of the composite respectively, and the fiber misalignments, the resin-rich zones, and voids are found. The compressive strengths of the quasi-UD woven fabric composite were obtained from the tests, and the in-plane X-shaped kink bands in the failed specimens have been shown in the postmortem analysis. Motivated by the experimental findings, a two-dimensional model based on an analysis of in-plane fiber waviness was built. The calculated results indicate the initial compressive failure is the tensile yielding of the matrix and the following shear yield failure of the matrix causes the in-plane X-shaped kink bands.

A.2 Unidirectional quasi-UD woven fabric composite

Twelve layers of the quasi-UD woven fabrics were stacked as a unidirectional lay-up, and cured with epoxy resin to make the quasi-UD woven fabric composite via a vacuum-assisted resin transfer molding (VaRTM) process. The epoxy resin used for consolidation is DENATOOL XNR/H 6809 from Nagase ChemteX Corp. Two cross-sectional inspections on the quasi-UD woven fabric composite were conducted in warp and weft directions, respectively.

A cross-section in the warp direction is shown in Fig. A1, in which *x* and *z* correspond to the warp and thickness direction of the composite, respectively. Several resin-rich zones with eyelet shapes caused by the weft yarns are randomly distributed in this cross-section. In the each resin-rich zone, the weft yarns, as black parts, are surrounded by brown resin. Moreover, the thickness of the weft yarns is approximately 0.06 mm, which is smaller than the diameter of the weft yarns before consolidation. Although reduction in compressive properties associated with the resin-rich zones is reported in Z-pin composites, the resin-rich zones in the quasi-UD woven fabric composite are much smaller than that in the Z-pin composites. Bending of the carbon fibers leads to out-of-plane fiber waviness near the resin-rich zones, and amplitude of the out-of-plane fiber waviness is assumed as half the thickness of the weft yarns, 0.03 mm.

Although negative influences of the out-of-plane fiber waviness are studied, comparing with the maximal amplitude of the in-plane fiber waviness, 0.2 mm, it is implied that the effect of the in-plane fiber waviness is greater than that of the out-of-plane fiber waviness in the quasi-UD woven fabric composite.

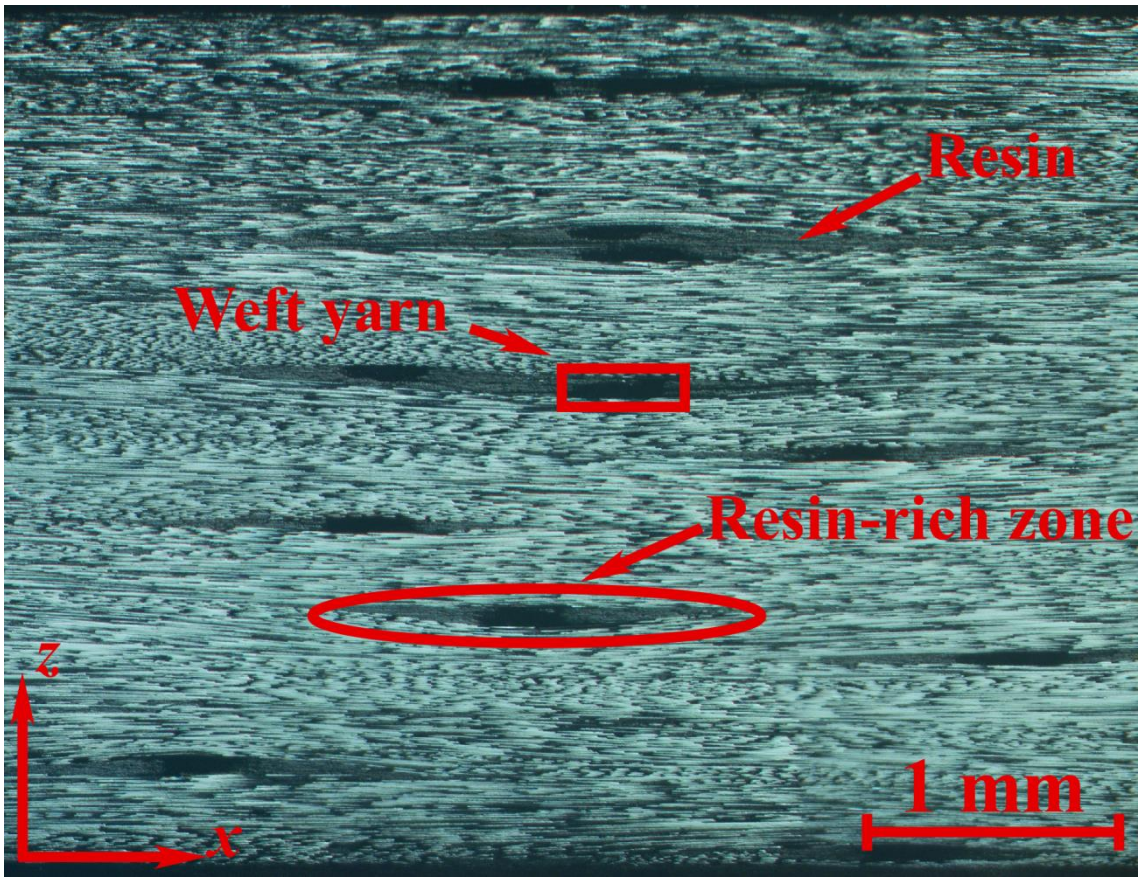

Fig. A-1 Cross-section in the warp direction

Fig. A-2 shows a cross-section in the weft direction, and *y* is the weft direction and the *z* is the thickness direction of the composite. The weft yarns are clearly displayed in

this cross-section, and are shown as thick black lines. The maximum width among the weft yarns is the same as the thickness of the weft yarns in the Fig. A-1. Thin brown lines are the resin in the resin-rich zone. These lines divide the carbon fibers into single tow or double tows, and the maximum and minimum widths in the fabrics are also reflected in this cross-section. Some voids in the interfaces among the glass fibers, the resin, and the carbon fibers are defects in the quasi-UD woven fabric composite to decrease the compressive strength as Fig. A-3.

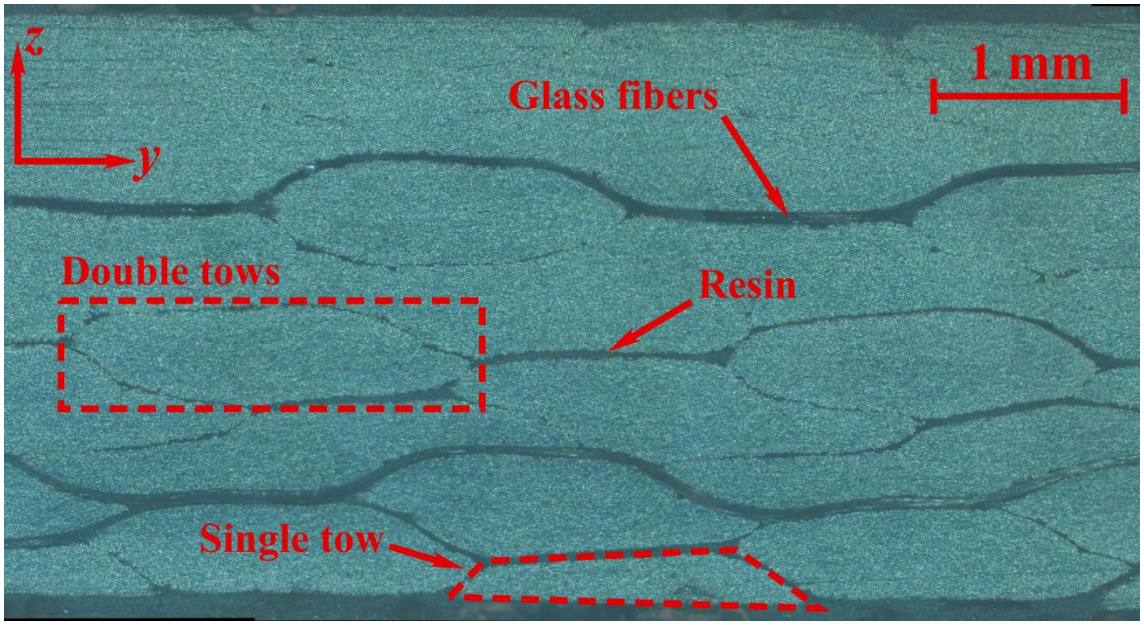

Fig. A-2 Cross-section in the weft direction

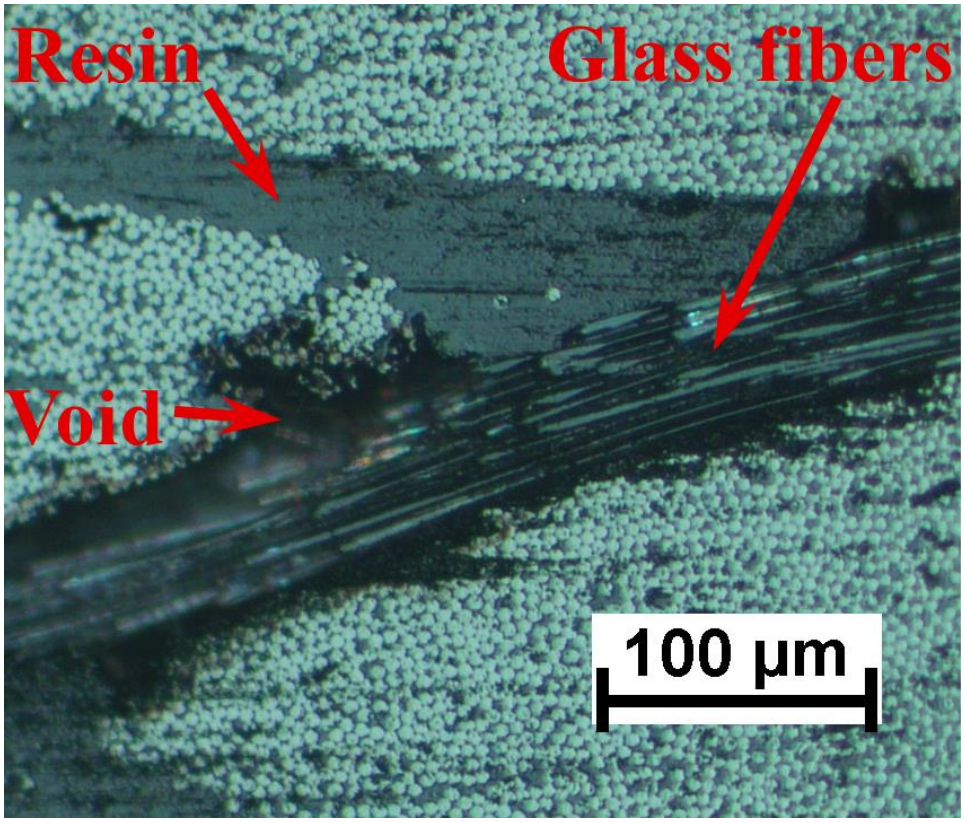

Fig. A-3 Interfaces among the glass fibers, the resin, and the carbon fibers

A.3 Compressive tests

Four specimens were cut from the quasi-UD woven fabric composite for compressive tests. According to ASTM D3410, each specimen is 140 mm long, 6.2 mm wide, and approximately 3.4 mm thick like Fig. A-4(a). The longitude direction of the specimens corresponds to warp direction of the quasi-UD woven fabric composite, and the width direction is the weft direction. Tabs fabricated with glass fiber composites were bonded to the two ends of each specimen by 63.6 mm long.

Each specimen was mounted in a support fixture, and each end of the specimen was fixed in place using 63.6 mm long binding grips, with a central gage area that is 12.8 mm long. Then, the specimen/support fixture combination was installed in the testing machine (INSTRON 8501, ±100 kN) for the compressive tests and the compressive loading was applied at the ends of the specimen as Fig. A-4(b).

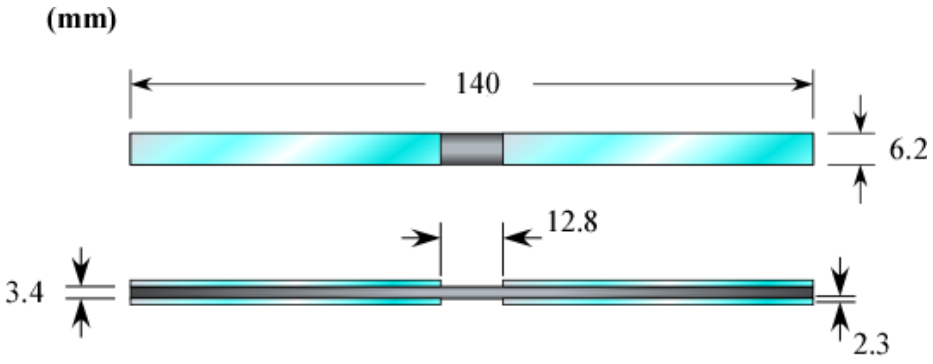

(a)

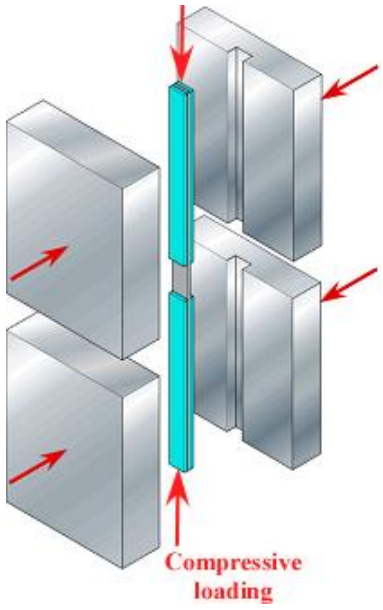

(b)

Fig. A-4 Dimension of specimens (a) and loading conditions (b)

A.4 Experimental results

The compressive tests were conducted with the aforementioned testing method, and the results are listed in Table A1. Considering a fiber volume fraction (V_f) disparity between the different specimens, we normalized the fiber volume fraction to 60%, and normalized average Young's modulus (E_L) and compressive strength (F_L) are equal to 155 GPa and 1184 MPa, respectively. Based on the rule of mixture, the theoretical Young's modulus is 178 GPa with 60% fiber volume fraction, which is greater than experimental results. The reduction in the modulus is due to a combined effect of the in-plane and out-of-plane fiber waviness, resin-rich zones, and voids in the quasi-UD woven fabric composite.

Table. A1 Experimental results of compression tests

	Stacking sequence	E_L [GPa]	F_L [MPa]	V_f [%]	ε_{max} [%]
LC-1	$[0]_{12}$	158	1154	61.3	0.801
LC-2	$[0]_{12}$	155	1271	61.4	0.898
LC-3	$[0]_{12}$	162	1421	61.4	0.935
LC-4	$[0]_{12}$	156	922	60.7	0.582

The stress and strain relationships of the compression tests are shown in Fig. A-5. As the figure shows, there are some stress-strain circles in the specimens LC-1 to 3, which indicate kink bands generate and propagate at this stage. The average Young's modulus and compressive strength of LC-1 to 3 are equal to 158 GPa and 1290 MPa, respectively. For comparison, the test of LC-4 was stopped at initial failure occurring. The in-plane failure patterns at point a and b, corresponding to the initial failure in LC-4 and ultimate failure in LC-3, are shown in Fig. A-6 and A-7, respectively.

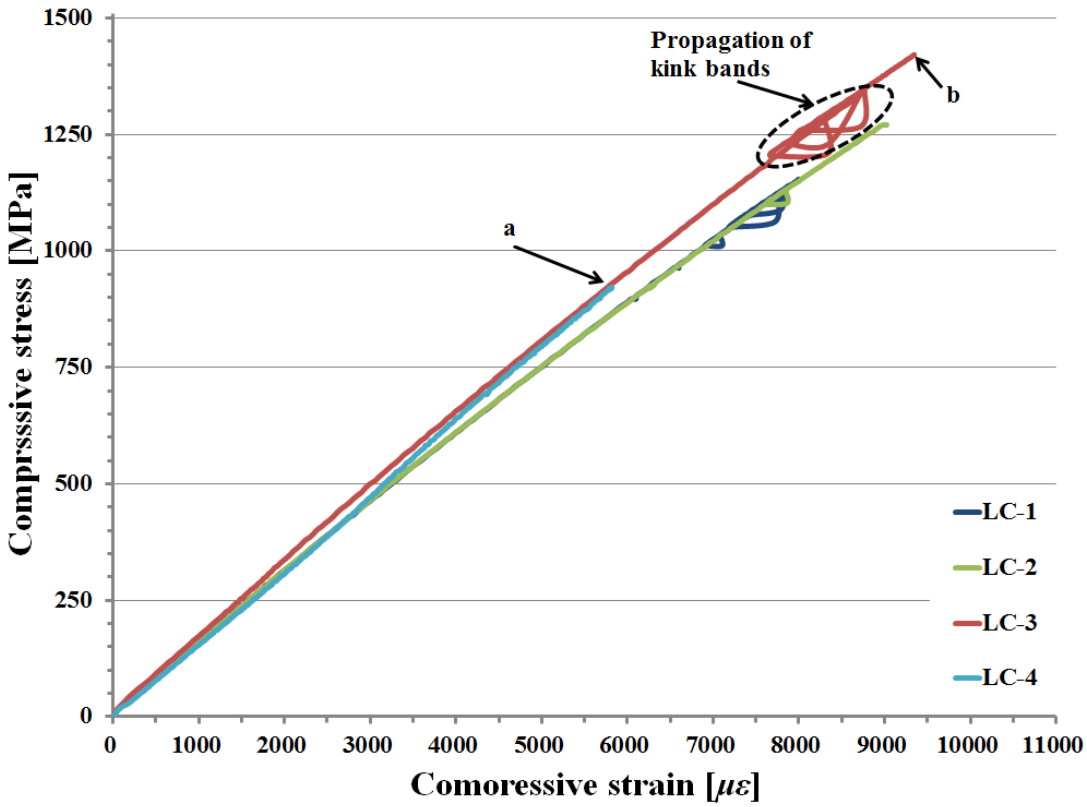

Fig. A-5 stress and strain relationships of the compression tests

A view of the in-plane kink bands in the specimen LC-4 is shown in Fig. A-6(a), where the *x* is the warp direction and *y* is the weft direction of the composite. Four major kink bands traverse the specimen in width direction, and intersect at a hole, which makes the failure pattern like the X-shape. The kink bands are found to be oriented at a range from 23° to 33° to the weft direction. Fig. A-6(b) shows a higher magnification view of the hole. The hole is formed with bands of broken carbon fibers, and several kink bands symmetrically surround the hole, whose widths are from 35 to 70 μm. We suspect that this is the location where failure initiated. The ultimate failure in LC-3 is shown in Fig. A-7. Compare with the initial failure in LC-4, the kink band and the center hole are crushed by the compressive stress, and the carbon fibers are thoroughly fractured and expand out, which make a larger deformation in the width direction than LC-4.

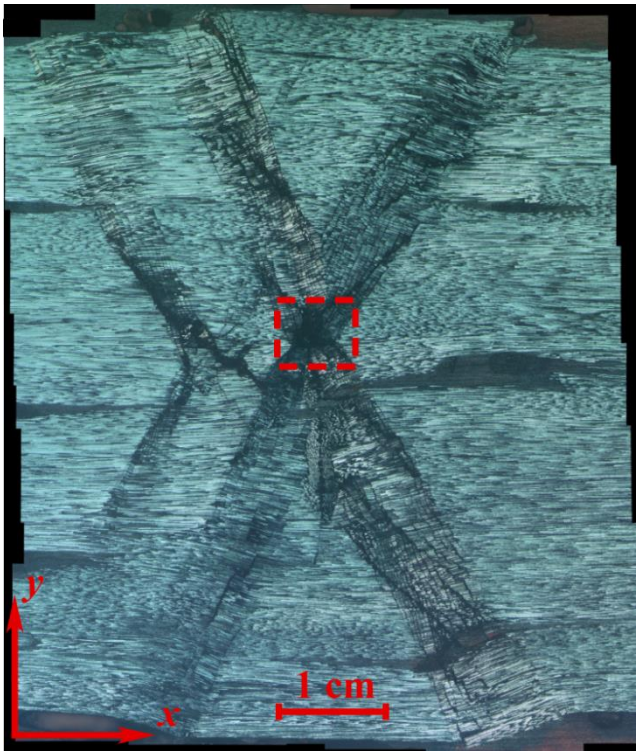

(a)

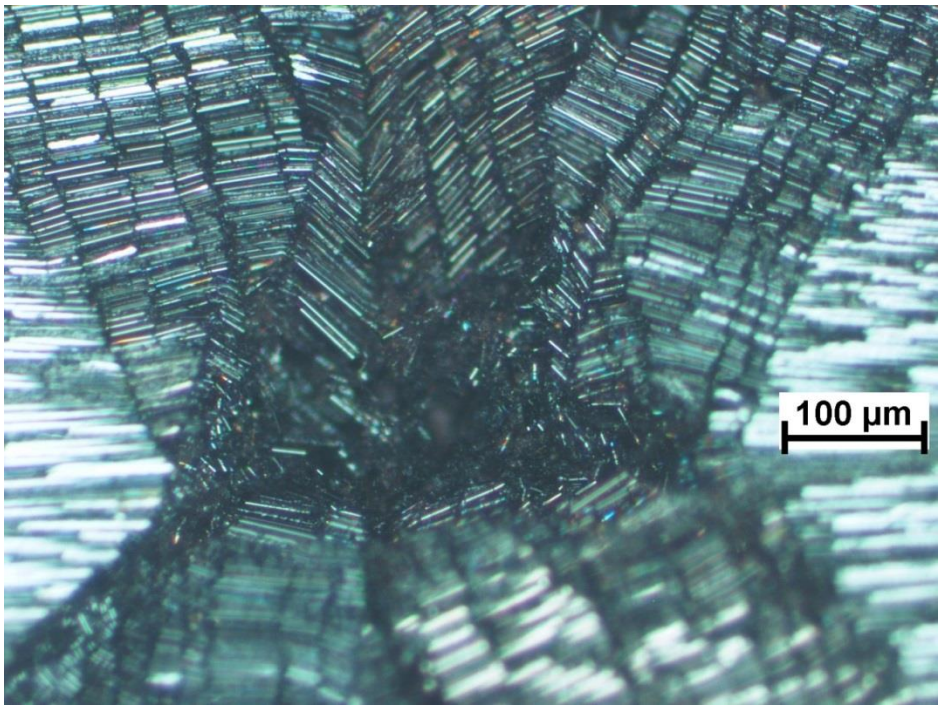

(b)

Fig. A-6 X-shaped kinking failure in LC-4 (a) and a higher magnification view (b)

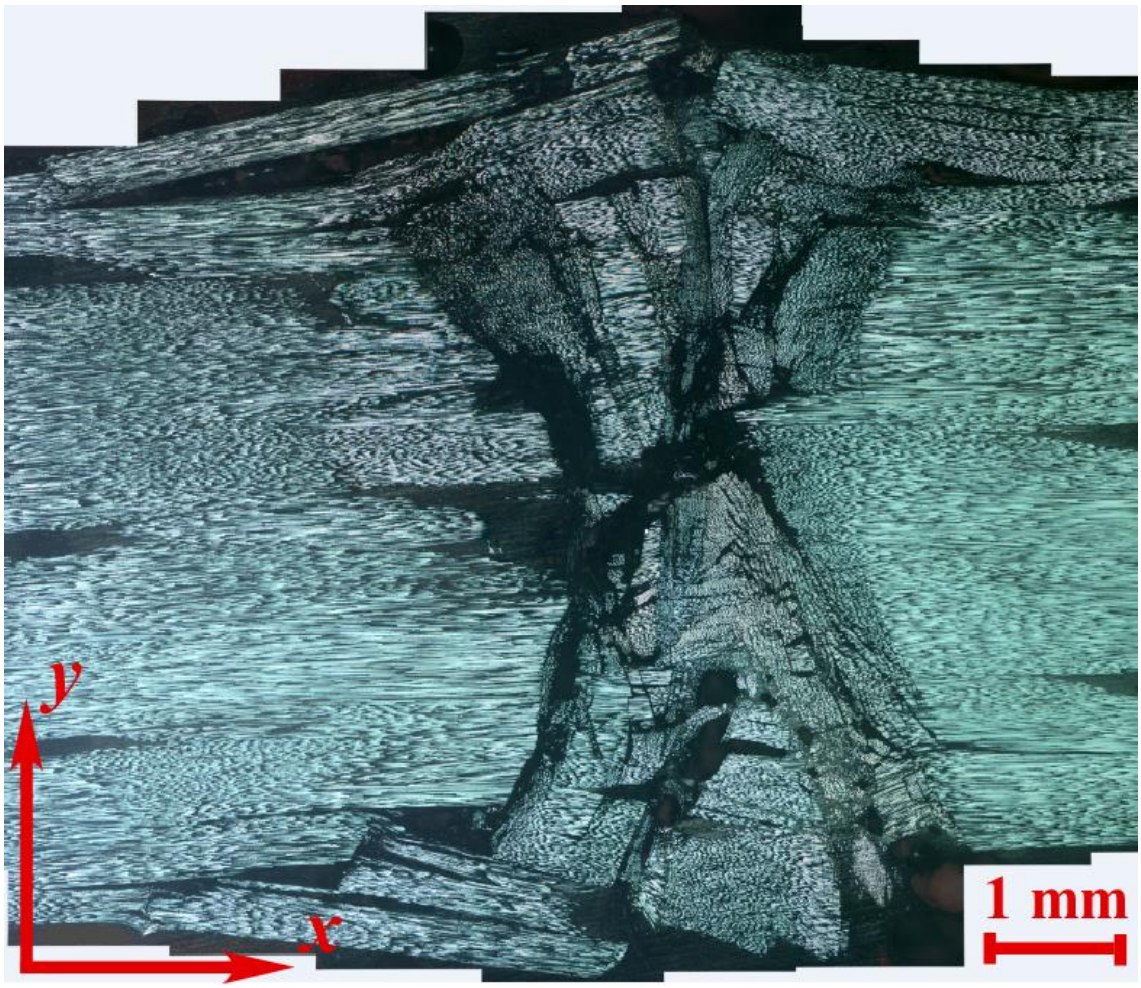

Fig. A-7 Ultimate failure in LC-3

A.5 Numerical simulations and discussions

Motivated by the experimental findings, the two-dimensional in-plane fiber waviness model in chapter 7 is modified to explain the in-plane X-shaped kinking failure mode. The modification is that a free edge boundary condition is set in edge d to simulate the kinking failure because the large deformation of the X-shaped kink bands in the weft direction and there are two or three intact tows in the weft direction of each of the specimen. Moreover, elastic properties are calculated from Chamis' theory. And an elastic-perfectly plastic property with Hill yield criterion is attributed to the artificial resin. Compressive yield strength, tensile yield strength, and shear yield strength are equal to 137 MPa (1% uniaxial yield strain), 86 MPa (epoxy's tensile strength), and 45 MPa (epoxy's shear strength), respectively.

The axial stress-end shortening response of the model is shown in Fig. A-8, and five deformed configurations of plastic strain (Fig. A-9) are numbered so as to correspond to the points identified in Fig. A-8. The model exhibits a linear response before initial failure. It becomes nonlinear a strain of 5000με (point i) when the initial yielding occurs at the bottom right corners of the model due to the effect of the in-plane fiber waviness. A distribution of a tensile stress along the weft direction indicates the tensile stress is a major factor in the initial yielding (Fig. A-9(a)). Then a shear yielding is caused by the

initial yielding at about 1100 MPa (Fig. A-9(b)) and propagates quickly toward the free edge d at an angle of about 25° with an obvious nonlinear response of strain and stress (Fig. A-9(c)), which corresponds to the initial failure of the composite, and the X-shaped kink bands are formed at this stage. Fig. A-10 shows a good agreement between the calculated kink band and a quarter of the X-shaped kink bands in LC-4. Hereafter the maximum shear yielding propagates to the free edge d and a maximal applied stress, 1342 MPa, is reached at a strain of 8200με (Fig. A-9(d)). As the experiments show, the average compressive strength of LC-1 to 3 is 1290 MPa, which agrees with the maximal applied stress well. After the point iv, the stiffness of the model is sharply reduced, and the expanding along weft direction increases obviously (Fig. A-9(e)) like the ultimate failure pattern in LC-3. In general, the kinking failure occurs because of the shear yield strength's reaching. However, the calculation indicates the initial failure is caused by the tensile yielding along weft direction and the resultant shear yield strain dominates the X-shaped kinking failure.

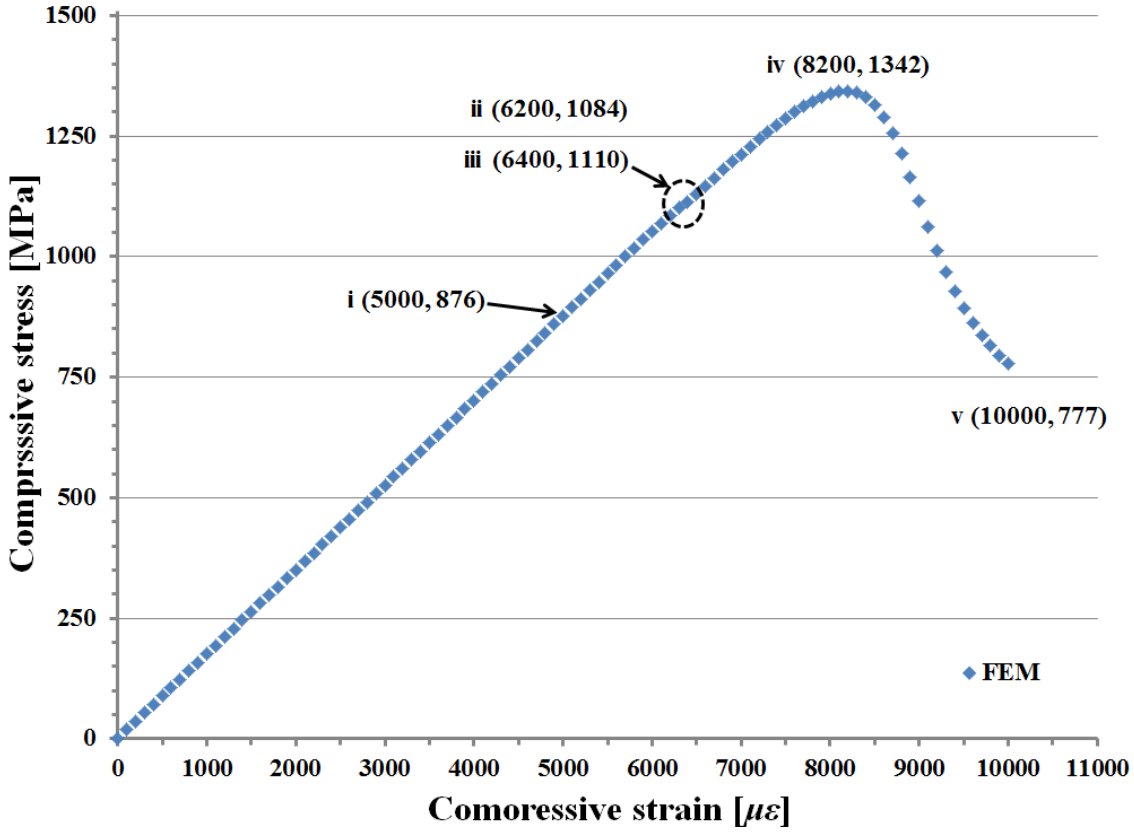

Fig. A-8 Axial stress-end shortening response of the model

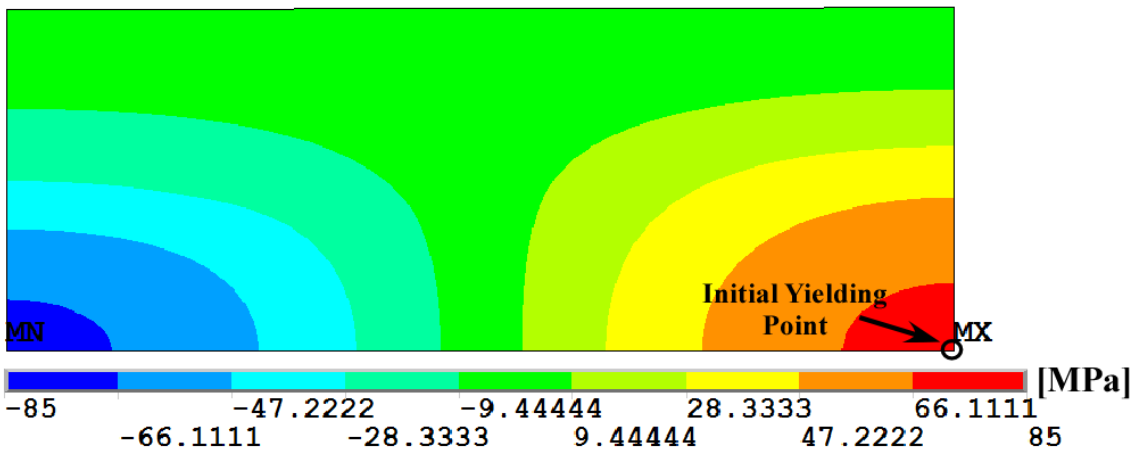

(a)

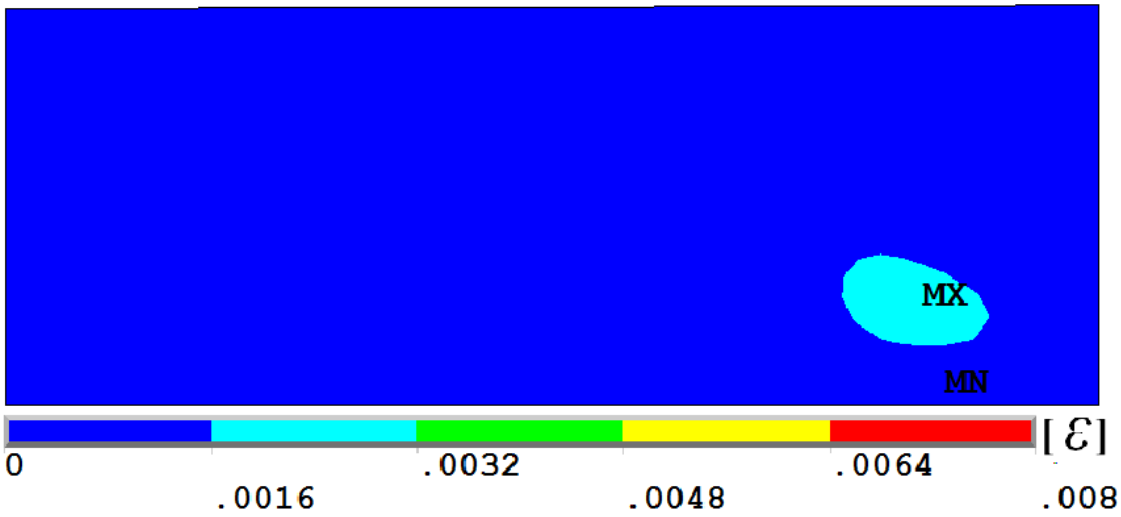
MX
MN
[ε]
0
.0016
.0032
.0048
.0064
.008

(b)

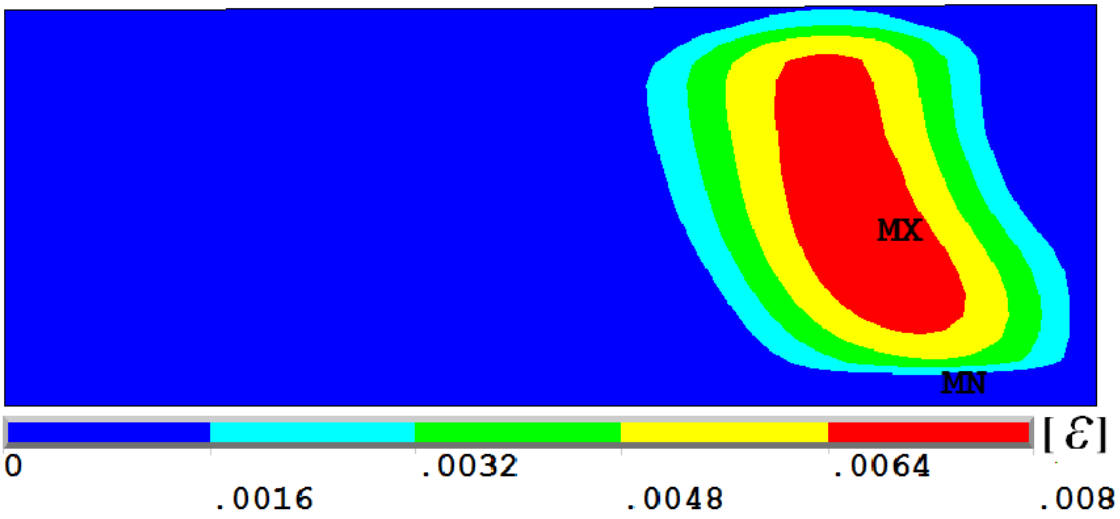
MX
MN
[ε]
0
.0016
.0032
.0048
.0064
.008

(c)

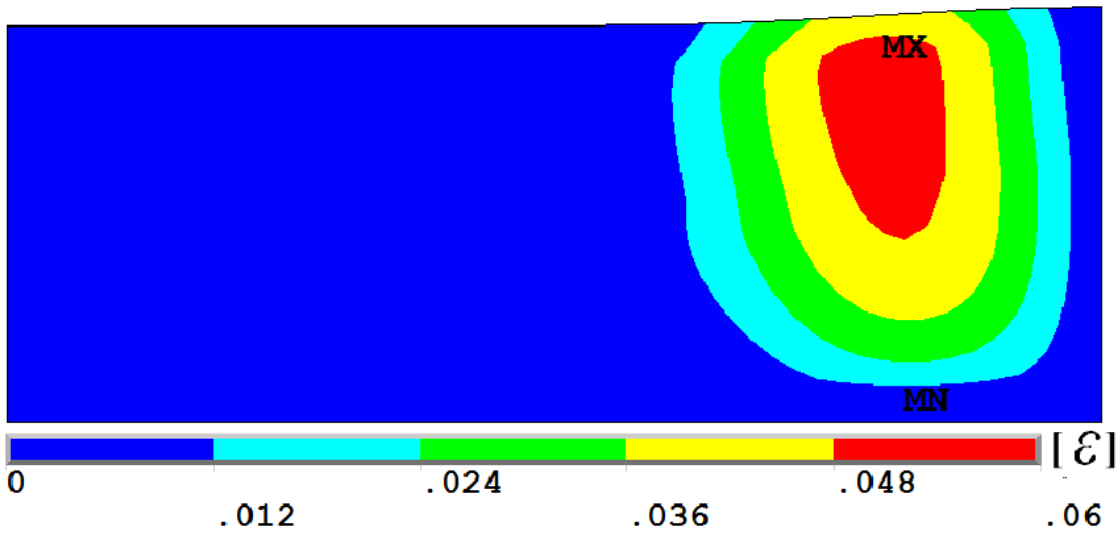

(d)

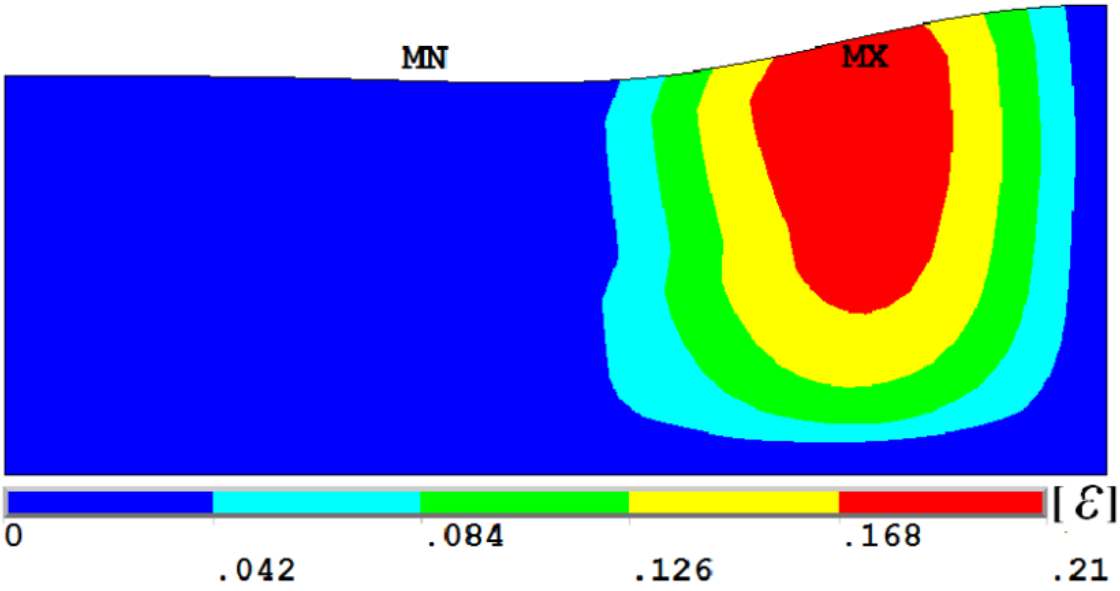

(e)

Fig. A-9 Five contours corresponding to the points in Fig. A-8: (a) distribution of a tensile stress at point i, (b-e) distributions of shear yield strain at point ii, iii, iv, and v.

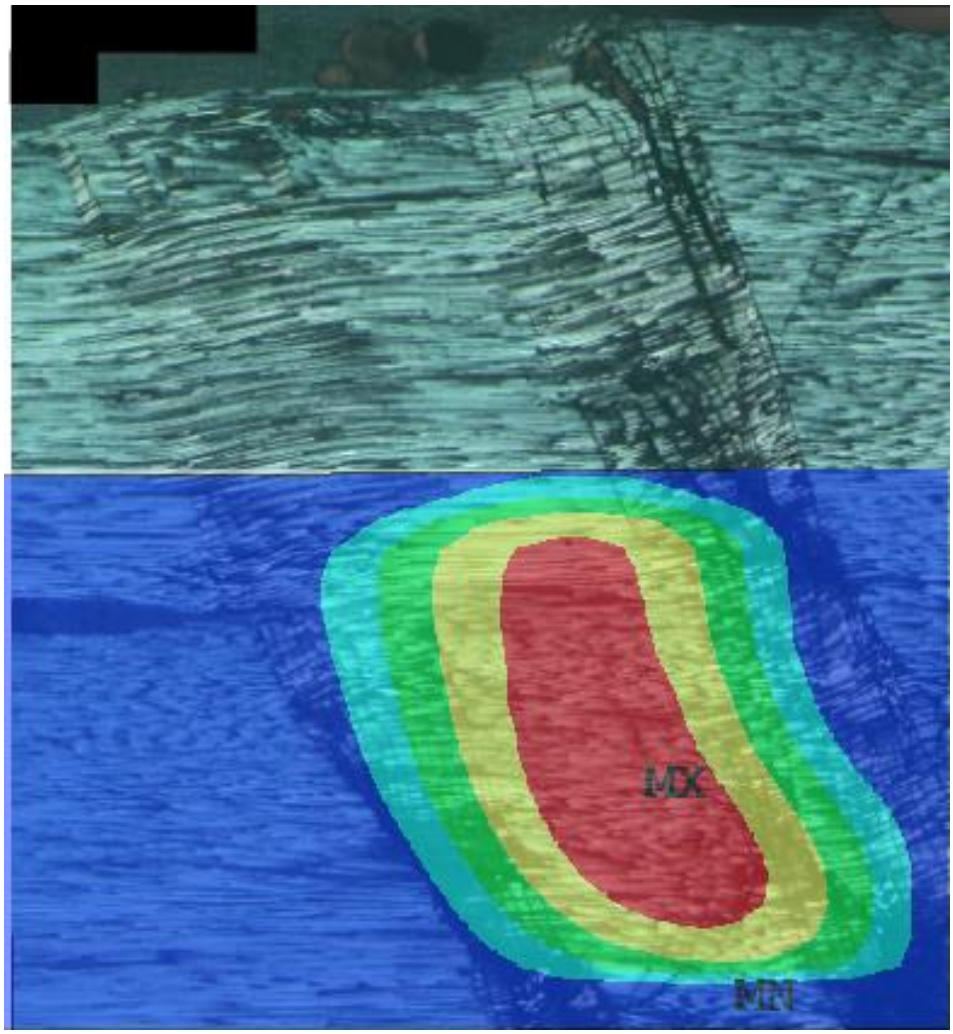

Fig. A-10. A comparison between simulation and experiment

A.6 Conclusions

This study has presented the failure mechanisms of the quasi-UD woven fabric composite under compression. The unidirectional quasi-UD woven fabric composite was fabricated from the standard quasi-UD woven fabrics and epoxy, and was inspected in the two transverse sections after consolidation. These inspections reveal the occurrence of the resin-rich zones, the out-of-plane waviness, and the voids in the quasi-UD woven fabric composite.

The compressive experiments were performed on the composite, which shows the X-shaped kinking failures in the failed specimens. The calculation using the two-dimensional model based on the analysis of in-plane waviness has been implemented to explain the experimental findings. The results show that the initial failure is derived from the tensile yielding along the weft direction of the composite and the subsequent shear yielding causes the X-shaped kink bands, which also indicates the compressive strength is sensitive to the tensile yielding strength of the matrix.